Aachener Verfahrenstechnik Series
AVT.CVT – Chemical Process Engineering
Volume 32 (2022)

Felix Stockmeier

Flow Fields in the Overlimiting Current Regime in Electrically-Driven Membrane Processes

DOI: 10.18154/RWTH-2022-11194

Flow Fields in the Overlimiting Current Regime in Electrically-Driven Membrane Processes

Felix Stockmeier

Flow Fields in the Overlimiting Current Regime in Electrically-Driven Membrane Processes

Strömingsfelder im überlimitierenden Strombereich von elektrisch getriebenen Membranprozessen

Von der Fakultät für Maschinenwesen
der Rheinisch-Westfälischen Technischen Hochschule Aachen
zur Erlangung des akademischen Grades eines Doktors
der Ingenieurwissenschaften genehmigte Dissertation

vorgelegt von

Felix Stockmeier

Berichter:
Univ.-Prof. Dr.-Ing. Matthias Wessling
Assoc. Prof. Ali Mani, Ph.D.

Tag der mündlichen Prüfung: 27.06.2022

Diese Dissertation ist auf den Internetseiten der Universitätsbibliothek online verfügbar.

Parts of this dissertation have been published. Reproduced with permission from:

Felix Stockmeier, Michael Schatz, Malte Habermann, John Linkhorst, Ali Mani, and Matthias Wessling
"Direct 3D observation and unraveling of electroconvection phenomena during concentration polarization at ion-exchange membranes", *Journal of Membrane Science*, 2021, DOI: 10.1016/j .memsci.2021.119846

Florian Roghmans, Elizaveta Evdochenko, Felix Stockmeier, Sven Schneider, Amel Smailji, Rahul Tiwari, Annabel Mikosch, Elif Karatay, Alexander Kühne, Andreas Walther, Ali Mani, and Matthias Wessling
"2D Patterned Ion-Exchange Membranes Induce Electroconvection", *Advanced Material Interfaces*, 2019, DOI: 10.1002/admi.201801309

Felix Stockmeier, Michael Schatz, Malte Habermann, John Linkhorst, Ali Mani, and Matthias Wessling
"Measurement of Electrokinetically Induced Hydrodynamics at Ion-selective Interfaces using 3D Micro Particle Tracking Velocimetry", *MethodsX*, DOI: 10.1016/j .mex.2022.101814

Parts of this chapter are submitted as:
Felix Stockmeier, Daniel Felder, Steffen Eser, Malte Habermann, Petar Perić, Stephan Musholt, Katharina Albert, John Linkhorst, and Matthias Wessling
"Localized Electroconvection at Ion-Exchange Membranes with Heterogeneous Surface Charge", *Under Review in Nature Materials*, 2021, Preprint available at Research Square as DOI: 10.21203/rs.3.rs-1093972/v1

Parts of this dissertation are in preparation for publication:

Felix Stockmeier, Lucas Stüwe, Elizaveta Evdochenko, Niklas Köller, Sebastian Brosch, Christian Kneppeck, Stephan Musholt, Katharina Albert, John Linkhorst, and Matthias Wessling
"Interaction Between Spacer-Altered Bulk Hydrodynamics and Electroconvection", *Journal to be decided*

Titel: Flow Fields in the Overlimiting Current Regime in Electrically-Driven Membrane Processes
Strömungsfelder im überlimitierenden Strombereich von elektrisch getriebenen Membranprozessen

Autor: Felix Stockmeier

Reihe: Aachener Verfahrenstechnik Series
AVT.CVT - Chemical Process Engineering
Volume: 32 (2022)

Herausgeber: Aachener Verfahrenstechnik
Forckenbeckstraße 51
52074 Aachen
Tel.: +49 (0)241 8095470
Fax.: +49 (0)241 8092252
E-Mail: secretary.cvt@avt.rwth-aachen.de
http://www.avt.rwth-aachen.de/AVT

Volltext verfügbar: 10.18154/RWTH-2022-11194

Acknowledgement

I was fortunate to work with many great people on scientific questions, publications, proposals, teaching, voluntary work, and this thesis. Such an achievement is always backed by multiple layers of support. It would be impossible to thank everybody that was involved in the process. However, some people substantially guided me on my way:

First of all, thank you, Prof. Dr.-Ing. Matthias Wessling for supervising this thesis. You enabled this exciting journey and provided me with the flexibility and multitude of learning opportunities that I longed for and which kept me going all these years. Additionally, you managed to put together a most inspiring and socially functioning group of individuals that is without equal. Toward the end of my thesis, you also made it possible for me to go abroad, which turned out to be one of the peaks of my scientific hike.

Thank you, Prof. Ali Mani, for agreeing to be my second examiner. I had the most intense and unforgettable time working with your group at Stanford. Thank you for your scientific and personal guidance during our inspiring collaboration and my research stay.

John Linkhorst, thank you for all the most interesting scientific discussions and personal guidance.

The people of DWI - Leibniz-Institut für interaktive Materialien e.V., Aachener Verfahrenstechnik (AVT), and, explicitly, Lehrstuhl für Chemische Verfahrenstechnik (AVT.CVT) were not only amazing colleagues but also became great friends along the way. Thank you to everybody for your support and friendship.

I had my first contact with CVT as a student assistant with Marco Scholz, who not only employed me despite my lack of membrane knowledge but also included me in the social structure of CVT. That was the groundwork for my way toward this manuscript. Additionally, all this only happened because Martin Dorn put me in contact with Marco. Thank you both for introducing me to CVT.

Afterward, I was very fortunate to work with Martin Wiese as a student and later office mate. Thank you, Martin, we were a great team (including Chris, Norman, and Denis), and I learned a lot during our work. You always kept your calm and brought me back down to earth when I was overthinking. I always saw you as a great inspiration along the way.

During my time at CVT, multiple colleagues had a significant impact on my work and well-being: Anna Kalde, Kristina Baitalow, and Denis Wypysek aka the 'Kaffee Babos'; Morten Logemann, Christian Linnartz, Lucas Stüwe, Niklas Köller, the rest of my Mutual Coaching groups, Patrick Bongartz, Maria Padligur, Florian Roghmans, and Georg Linz who gave me the

inspiration for the first functioning version of my microfluidic electrochemical module. Thank you all, I highly value our close friendships and deep scientific exchanges.

A big thank you to all the people without whom the work at CVT would end up in total chaos: Sekretariat, Mechanische Werkstatt, Elektrische Werkstatt, IT, ZAL, and Karin Faensen.

Thank you to all the students who supported my work and without whom none of this would have been possible. I was fortunate to supervise multiple Bachelor's theses and Master's theses: your work built the foundation of my research, for which I am incredibly grateful. I am most proud that many students even voluntarily extended their time under my guidance as working students: I hope that I could provide you with an interesting and encouraging environment and, may be, one or two helpful pieces of advice.

During my time at Stanford, I was quickly welcomed and integrated into Ali's group, especially thanks to Yassaman Shirian, Jessie Liu and Arunraj Balaji. Additionally, I felt right at home because of my great host Silvestre, my housemates, and my awesome beach volleyball friends.

I also received great help from Denis Wypysek, Anna Kalde, Kristina Baitalow, Lucas Stüwe, and Max Stockmeier, who proofread this manuscript multiple times.

Natürlich hat auch meine Familie entscheidend zu dieser Dissertation beigetragen. Ein erster Dank gilt meiner Schwiegerfamilie dafür, dass ihr mich herzlich aufgenommen und Tsatsa und mich durch das Studium und die Promotion hindurch unterstützt habt. Danke auch an meine Großeltern, die mich von klein auf mit zu dem Menschen erzogen haben der ich heute bin und vor Allem meine Neugierde und Kreativität gefördert haben.

Genau so möchte ich meinen Geschwistern und Eltern danken, die mich auf diesen Weg gebracht, begleitet und gehalten haben. Im Besonderen danke ich meiner Mama für die unzähligen Kilos Eingefrorenes. Das Essen war nicht nur immer eine großartige Unterstützung, sondern auch eine wahre geschmackliche Bereicherung. Ihr alle habt dazu beigetragen, dass ich meine Studien- und Promotionszeit mit so viel Durchhaltevermögen bewältigen konnte.

Zu guter Letzt geht der größte Dank an meine Frau Tsatsral Oyunbaatar. Wir haben uns vom Anfang des Studiums bis heute stets gegenseitig unterstützt und dadurch alle Widrigkeiten gemeistert. Ich weiß, dass wir zusammen jede Herausforderung stemmen können und dafür bin ich dir unendlich dankbar!

Für meine Familie

Contents

Abstract

Electroconvection, a hydrodynamic instability which convectively mixes the ion-depleted diffusion boundary layer in electrically-driven membrane processes, enables the operation of such processes beyond a diffusion-limited current density. When operating at overlimiting current densities, industrial processes could be designed with smaller membrane modules and, thus, reduced investment costs. Still, the energy needed to overcome the diffusion-limitation as well as concerns regarding water splitting still stand in the way of their application. Both hindrances can be reduced by effectively triggering and tailoring the 3D electroconvective vortex field. However, the 3D features of electroconvection and their interaction with membrane surface modifications or spacer hydrodynamics are lacking experimental quantification. Until now, experimental studies were limited to 2D measurement techniques and 3D simulations which are restricted to small scales due to computational costs.

This thesis surpasses this limitation and presents an experimental method for quantification of the 3D velocity field of electroconvection with high temporal and spatial resolution. Using this method, we quantify the velocity field and its statistics close to a cation-exchange membrane in a steady or pumped electrolyte. We further measure its interaction with modified membrane surfaces and spacer structures.

We conducted these measurements in a newly designed electrochemical cell using micro particle tracking velocimetry for 3D velocity reconstruction. The recorded velocity fields were then used to visualize coherent vortex structures and reveal changes in the velocity field and its statistics. During the transition from vortex rolls to vortex rings with increasing current densities, changes in the rotational direction, mean square velocity, and temporal energy spectrum with only little influence on the spatial spectrum were revealed.

Additionally, we investigated the impact of membrane surface modifications with two types of microgels varying in zeta potential on the vortex field's build-up. We discovered that a large difference in zeta potential between microgel and membrane material offers full control over the velocity field in terms of structure and rotational direction.

Lastly, we quantified the interaction of the electroconvective velocity field with spacer-induced hydrodynamics in a pumped electrolyte. The velocity fields and their statistics revealed that significant interaction only appears at Reynolds numbers below one. However, pilot-scale experiments reported the appearance of overlimiting currents in such systems. Which is why measurements on a smaller scale at higher current densities are expected to provide further insights.

This thesis emphasizes the potential of specifically engineered membrane surfaces and spacer structures for overcoming the limitations of electrically driven membrane processes. Tailored interaction of controlled electroconvection and spacer hydrodynamics could reduce the energy to overcome limiting currents in industrial applications to a minimum.

Zusammenfassung

Elektrokonvektion ist eine hydrodynamische Instabilität, welche die ionenverarmte Diffusionsgrenzschicht in elektrisch getriebenen Membranprozessen konvektiv durchmischt und dadurch deren Betrieb jenseits der limitierenden Stromdichte ermöglicht. Aktuell stehen dem Einsatz solch hoher Stromdichten ein erhöhter Energieaufwand zur Überwindung der Diffusionslimitation sowie Bedenken bezüglich Wasserspaltung bei hohen Spannungen entgegen. Beide Herausforderungen könnten durch eine effektive Erzeugung und Beeinflussung des 3D-elektrokonvektiven Wirbelfeldes überwunden werden. Das 3D-Wirbelfeld und dessen Wechselwirkung mit Membranoberflächenmodifikationen oder der durch Spacer hervorgerufen Hydrodynamik wurden jedoch bisher nicht experimentell quantifiziert. Aktuelle Forschung ist auf 2D-Messverfahren oder 3D-Simulationen beschränkt, die aufgrund ihrer langen Rechenzeiten nur kleine Skalen auflösen.

Diese Arbeit stellt eine experimentelle Methode zur Quantifizierung des 3D-Geschwindigkeitsfeldes der Elektrokonvektion mit hoher zeitlicher und räumlicher Auflösung vor. Mit dieser Methode quantifizieren wir das Geschwindigkeitsfeld und dessen Statistik an einer Kationenaustauscher-Membran in einem stationären oder gepumpten Elektrolyten. Des Weiteren messen wir die Wechselwirkung des Geschwindigkeitsfeldes mit modifizierten Membranoberflächen und Spacer-Strukturen.

Für diese Messungen haben wir eine elektrochemische Zelle entworfen, welche die Aufnahme des 3D-Geschwindigkeitsfeldes mittels mikro Particle-Tracking-Velocimetry (µPTV) erlaubt. Mit diesen Geschwindigkeitsfeldern konnten dann kohärente Wirbelstrukturen visualisiert und Veränderungen des Feldes erfasst und dessen Statistik gezeigt werden. Während des Übergangs von Wirbelrollen zu Wirbelringen bei steigender Stromdichte wurden Änderungen der Rotationsrichtung, der mittleren quadratischen Geschwindigkeit und des zeitlichen Energiespektrums, mit nur geringem Einfluss auf das räumliche Spektrum festgestellt. Zusätzlich konnten wir zeigen, dass die Membranmodifikation mit Mikrogelsuspensionen die volle Kontrolle über das Geschwindigkeitsfeld in Bezug auf Struktur und Rotationsrichtung ermöglicht. Abschließend quantifizierten wir die Wechselwirkung des elektrokonvektiven Geschwindigkeitsfeldes mit der Spacer-induzierten Hydrodynamik in einem gepumpten Elektrolyten. Hier trat eine signifikante Wechselwirkung allerdings nur bei Reynoldszahlen unter eins auf. Experimente im Pilotmaßstab zeigten jedoch von überlimitierenden Stromdichten in solchen Systemen, weshalb Messungen auf kleinerer Skala bei höheren Stromdichten weitere Erkenntnisse versprechen.

Diese Dissertation unterstreichen das Potenzial modifizierter Membranoberflächen und Spacer-Strukturen zur Überwindung der bisherigen Limitationen elektrisch angetriebener Membranprozesse. Ein maßgeschneidertes Zusammenspiel von kontrollierter Elektrokonvektion und Spacer-Hydrodynamik könnte die Energie zur Überwindung des limitierenden Stromes in industriellen Anwendungen auf ein Minimum reduzieren.

1 Introduction

Parts of this chapter have been published as:
Felix Stockmeier, Michael Schatz, Malte Habermann, John Linkhorst, Ali Mani, and Matthias Wessling, "Direct 3D observation and unraveling of electroconvection phenomena during concentration polarization at ion-exchange membranes", *Journal of Membrane Science*, 2021
DOI: 10.1016/j.memsci.2021.119846

Felix Stockmeier, Michael Schatz, Malte Habermann, John Linkhorst, Ali Mani, and Matthias Wessling, "Measurement of Electrokinetically Induced Hydrodynamics at Ion-selective Interfaces using 3D Micro Particle Tracking Velocimetry", *MethodsX*, 2022
DOI: 10.1016/j.mex.2022.101814

Parts of this chapter are submitted as:
Felix Stockmeier, Daniel Felder, Steffen Eser, Malte Habermann, Petar Perić, Stephan Musholt, Katharina Albert, John Linkhorst, and Matthias Wessling, "Localized Electroconvection at Ion-Exchange Membranes with Heterogeneous Surface Charge", *Under Review in Nature Materials*, 2021
Preprint available at Research Square as DOI: 10.21203/rs.3.rs-1093972/v1

Parts of this chapter are in preparation for publication:
Felix Stockmeier, Lucas Stüwe, Elizaveta Evdochenko, Niklas Köller, Sebastian Brosch, Christian Kneppeck, Stephan Musholt, Katharina Albert, John Linkhorst, and Matthias Wessling, "Interaction Between Spacer-Altered Bulk Hydrodynamics and Electroconvection", *Journal to be decided*

Water is the most valuable resource for humanity and life in general. Not only do we drink water, but it is also needed for many industrial processes like food production or as a reactant in the chemical industry. Actually, about 90 % of the globally used water goes into the food industry [Djeh2019].

One could think that we luckily live on the 'blue planet' covered mainly in this most valuable resource. However, only 0.5 % - 1 % of earth's water resources are sustainable accessible [Pete2016; Gude2017]. Additionally, water use increased by a factor of six over the past 100 years, and our resources are dwindling faster as they can naturally be replenished [Gude2017; UNES2020]. Another critical challenge for many regions is the geographic and temporal mismatch between supply and demand of freshwater over the year [Meko2016].

Today, already half of the world's river basins are stressed beyond sustainable consumption [Hoek2014]. Two-thirds of the world's population, or approximately 4 billion people, suffer from severe water scarcity at least once a month and half a billion face water scarcity over the whole year [Meko2016] while about 3.4 million die by drinking contaminated water each year [Tzan2020].

In the future, the situation is expected to get even worse. Not only will climate change lead to a more significant disparity in the supply and demand of water [Pete2016; Dina2019; UNES2020] but also will the increase of the world's population to an expected 10 billion by 2050 and increasing living standards with changing consumption patterns lead to a rising water demand [Gude2017; Meko2016; Djeh2019; UNES2020]. Connected to the risk of water scarcity are also risks to secure food production, sustainable development, and global trade [Meko2016; Qu2018; Dina2019].

Considering the severe impact of increasing water scarcity, it comes with no surprise that global organizations like the WHO, UNESCO, and UNICEF all classify water scarcity as one of today's prime global challenges [Worl2017; Unit2019; UNES2020]. Water scarcity is a problem not only of countries associated with less developed infrastructure and industry; it also concerns developed countries like the US and southern

Europe and other regions once rich with water [Lavr2017; Gude2017; Mars2020]. Thus, the supply of potable water is a worldwide challenge setting a responsible task to scientists of all nations.

A crucial solution to water scarcity is the use of sea-, brackish-, river-, or even wastewater as alternative water resources by desalination [Ali2018; Jone2019; Tzan2020]. With many technologies already working at their thermodynamic limit, membrane processes offer low-energy processes with small ecological footprints and, thus, gain increased interest [Gude2017; Ali2018; Nass2020]. Especially the combination of membrane processes and renewable energy sources seems attractive [Ali2018; Nass2020]. Additionally, recent developments in electrically-driven membrane processes demonstrate potential for increased overall process efficiency [Door2021]. However, their energy consumption and general costs are still too high for wide spread application [Nass2020; Door2021]. Only when convectional processes are substituted by innovative, energy-efficient, and cost-effective technologies, alternative water sources can be utilized by desalination processes [Gude2017].

In electrically-driven membrane desalination processes, a potential is applied to move ions through ion-exchange membranes which are composed of polymers with either positive or negative fixed charges. The charge of the polymer determines the type of ion that can pass through which classifies them as cation-exchange and anion-exchange membranes (CEMs and AEMs), respectively.

Currently, industrial electrically-driven membrane processes are technically limited to a maximum current density. After the initial linear dependency between ion current per membrane area and applied potential, a concentration profile develops between the bulk solution and the membrane. The ion concentration close to the membrane approaches zero leading to increased fluid-side resistance. Therefore, the ion flux reaches a limiting current density (i_{lim}) visible as a plateau in a current versus voltage curve. At this point, a larger driving force results only in a negligible flux

increase.

This plateau's appearance can be delayed by hydrodynamic means like increased flow velocity or the insertion of spacers that promote mixing. However, the effectiveness of these measures also has its limitations. Here, the immense opportunity of electrically operated membrane processes emerges [Bazi2020]: Unlike in pressure-driven processes, the flux-over-potential plot shows a third region with further increasing ion flux beyond the limiting current density.

This overlimiting current region's primary driver is a fluid instability called electroconvection (EC) [Rubi2000; Mani2020]. During EC, a 3D vortex field emerges that mixes the boundary layer close to the membrane. Thereby, the high-concentrated bulk solution is transported to the membrane surface counteracting the increased resistance. The analysis of this fluid instability's 3D velocity field and of means to exercise control over its features build the core of this thesis.

The following sections give a more detailed introduction of important theoretical concepts and assumptions used in this thesis. After that, state of the art concerning the topics covered in this thesis is briefly reviewed. The chapter ends with the scope of this thesis.

1.1 Ion-exchange membranes

Ion-exchange membranes (IEMs) are build up of a polymeric backbone with either positive or negative fixed charges. Figure 1.1 illustrates the transport of cations through a cation-exchange membrane (CEM).

Under usual circumstances, electroneutrality is assumed in all media. Therefore, the sum of charges of all species add to zero [Meli2007]:

$$\sum_i z_i \cdot c_i = 0 \tag{1.1}$$

Here, z_i is the valence number that can assume integer values and c_i

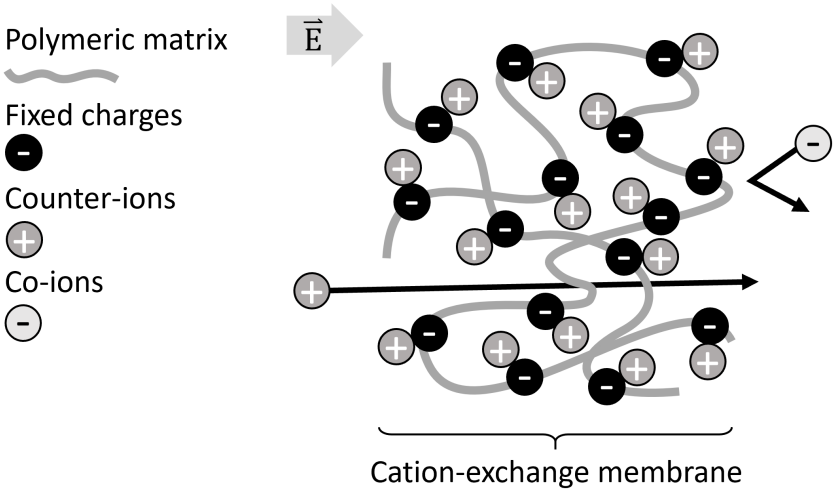

Figure 1.1: Illustration of ion passage and rejection by a cation-exchange membrane. The membrane is illustrated as a polymeric matrix with fixed charges. The applied field leads to the transport of counter-ions through the membrane while co-ions are rejected due to electrostatic repulsion of the fixed charges. Adapted from Melin and Rautenbach [Meli2007].

is the concentration. In the case of a symmetric binary electrolyte, which will be used throughout this thesis, there are only two ionic species present with equal concentrations $c_+ = c_-$ and opposite valence numbers $z_+ = -z_-$.

The electroneutrality assumption also applies to an IEM. Here, the fixed membrane charges are often included as a single parameter ξ [Meli2007]:

$$\sum_i z_i \cdot c_i + \xi = 0 \tag{1.2}$$

Supposing the membrane charge concentration has a negative value ($\xi < 0$), the charge is compensated by cations while anions are rejected. The result is in a cation-exchange membrane as pictured in Figure 1.1. The opposite case ($\xi > 0$) results in an anion-exchange membrane.

The charge selectivity of IEMs is used in a variety of processes and applications. This includes processes for desalination and deionization like electrodialysis (ED) [Stra2010; Werb2016], capacitive deionization (CDI) [Pora2013], and flow-capacitive deionization (FCDI) [Gend2014; Romm2015; Tang2020]. Furthermore, such membranes are essential in processes for energy harvesting, storage, or conversion, like reverse

electrodialysis (RED) [Post2007] and RedOx-flow batteries [Alot2014; Park2017; Perc2020]. Additionally, there are novel applications in microfluidics [Slou2014].

1.2 Electrodialysis

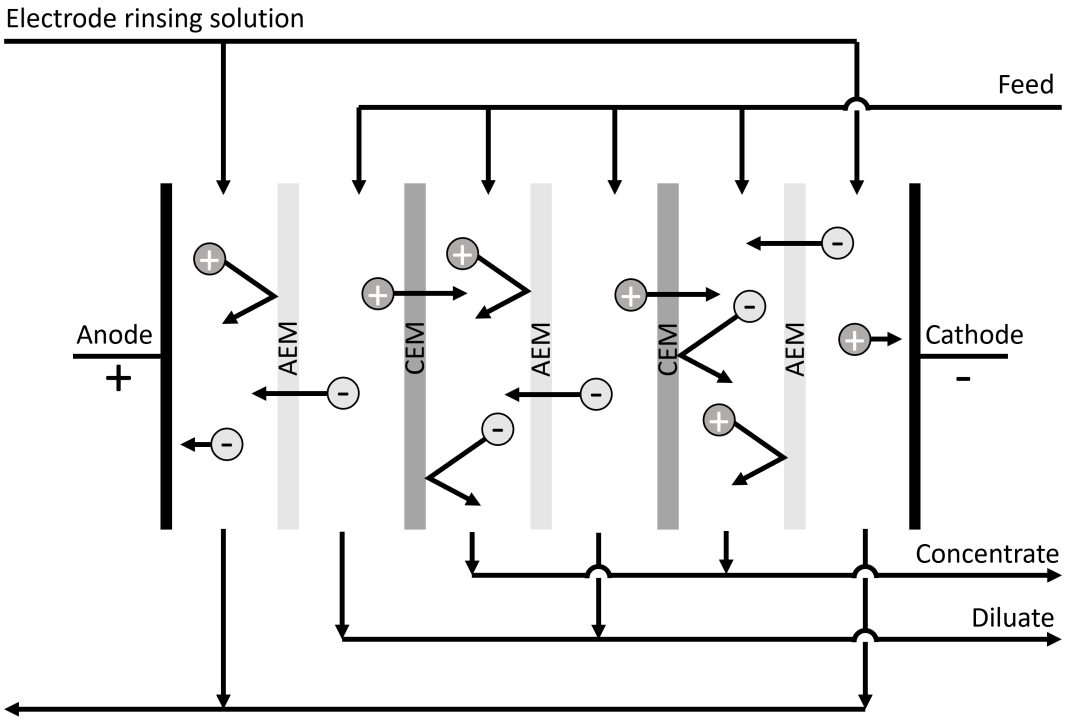

Figure 1.2: Schematic of a typical electrodialysis set-up. The set-up comprises alternating anion- and cation-exchange membranes, and the outer electrodes. The applied electric field leads to the depicted ion movement resulting in concentrated and diluted streams. The electrode rinsing solution transports the products of Faradaic reactions out of the system. Adapted from Melin and Rautenbach [Meli2007].

Out of before mentioned processes, ED is the most common electrically-driven membrane process. Its simplicity also results in the use as a model process in many studies dealing with electrokinetic phenomena [Prob1994]. It utilizes alternately stacked IEMs forming multiple compartments as depicted in Figure 1.2. Two electrodes enclose the outer compartments. A salt-containing feed solution, the electrolyte, is pumped through each compartment. During operation, an electrical field is applied

via the electrodes. Inside this field, anions and cations move towards their specific counter electrode. They pass through the adjacent membrane or are rejected. This process leads to concentrated and depleted fluid streams. The ionic equilibrium in the electrode compartments is maintained by faradaic reactions taking place at the electrodes. The reaction products are removed by a rinsing solution.

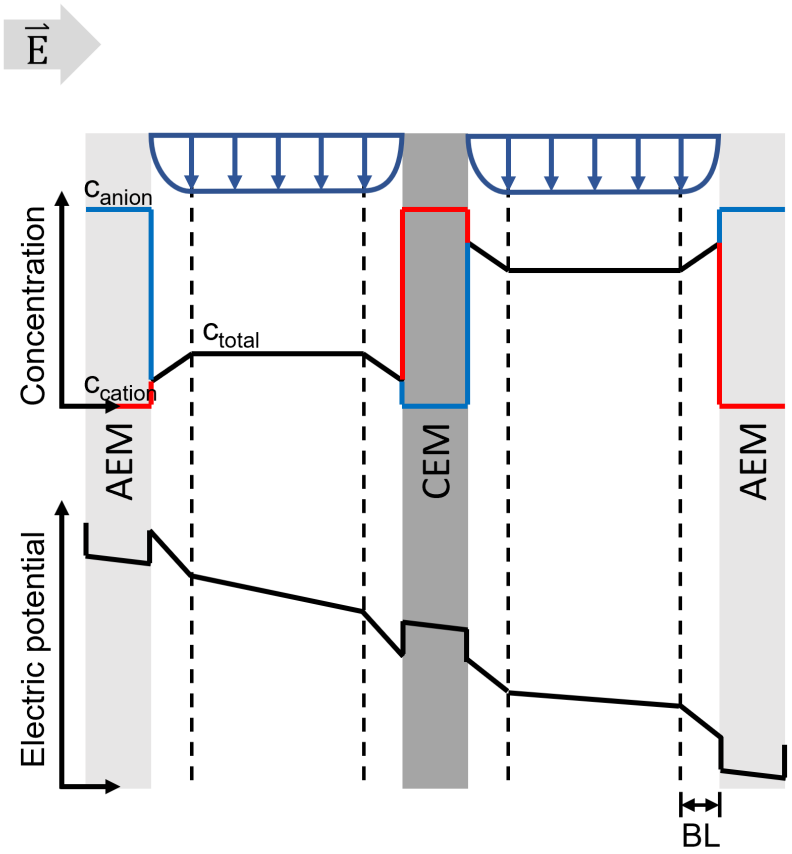

Figure 1.3: Concentration and electric field gradients in electrodialysis compartments. The top graph illustrates the course of the anion and cation concentration over a concentrate and diluate compartment pair under the effect of an electric field and plug flow. The bottom graph illustrates the resulting course of the electric potential. The dotted line exaggerates the stagnant boundary layer (BL). Adapted from Probstein [Prob1994].

Figure 1.3 outlines the concentration and electrical potential profiles in a diluate and concentrate compartment adjacent to a CEM. In the graphic, plug flow and ideal membrane behavior are assumed, resulting in an ideally mixed bulk with constant concentrations, and complete rejection of co-ions

inside the membranes. Close to the membranes, a stagnant boundary layer (BL) appears.

The ion mobility inside the membranes is higher than in the electrolyte. Therefore, high fluxes through the membranes cause decreasing concentration at the membrane-fluid interface in the desalinating compartment. Concentration gradients, the so-called concentration polarization (CP), develop between the bulk solution and the membranes due to the slow diffusive transport of ions in the BL. The same phenomenon is observed in the concentrating compartment but with an inverse direction: the ion concentration increases in the BL at the membrane. The concentration profiles directly correlate with the electric potential. Gradients in the total concentration lead to an increase in slope of the potential. The potential drop over the whole cell divided by the ion flux is proportional to the cell resistance. Therefore, evolving CP leads to increasing cell resistance and eventually to a current saturation, the so-called limiting current density. This resistance can be overcome by mixing the BL. In a typical industrial ED setup, spacers are inserted in the electrolyte compartments that increase mixing, introducing more complex hydrodynamics [Prob1994]. The effects of spacers are discussed in a later Section 1.4.

In Figure 1.3, the concentration profiles are depicted as a linear correlation, but in reality, more complex relations occur with increasing applied potential, which will be discussed in the following sections.

1.3 Ion transport in aqueous solutions at ion-exchange membranes

In the following, the different mechanisms of ion transport in the BL with increasing potential are described. First, the situation close to a CEM at a moderate potential is described on a molecular level. Then, the implications of this theory are extended to larger potentials.

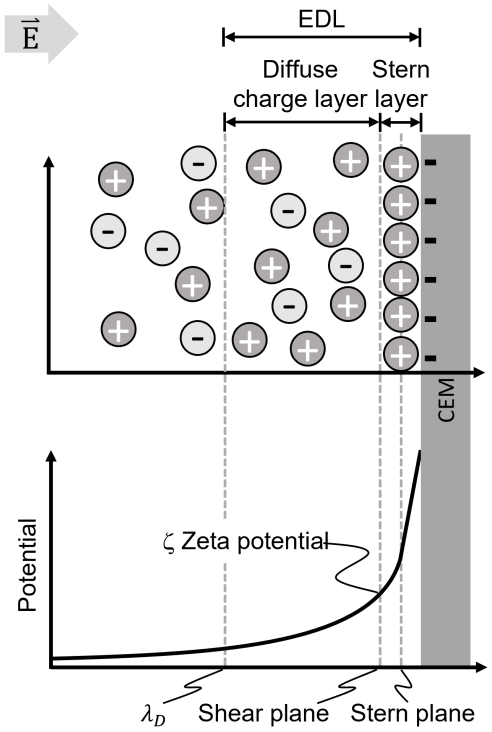

Figure 1.4: Ion distribution at the cation-exchange membrane surface. The top graph illustrates the influence of the cation-exchange membrane's surface charge on the ion distribution in the electrolyte close to that surface under the effect of an electric field. The bottom graph illustrates the resulting course of the electric potential. Adapted from Probstein [Prob1994] and Bazant et al. [Baza2009].

Fig 1.4 illustrates the situation in the electric double layer (EDL) close to a CEM at a moderate potential. The membrane's surface potential is largely compensated by adsorbed counter-ions. The ions and their hydration shells are held in the vicinity of the surface, called the Stern layer, by the electric field. Due to the finite size and interaction between the counter-ions, the surface charge's effect cannot be fully compensated and reaches further into the electrolyte. Therefore, a diffuse charge layer emerges where the excess potential is compensated by accumulating counter-ions. The size of this layer is described by the Debye length λ_D. The ion distribution is reflected in the course of the electric potential. The potential has its maximum at the membrane surface and decreases linearly towards the Stern plane which is located at an ion's radius distance from the surface. From there on, the potential decreases exponentially. The transition from the immobile Stern layer to the mobile diffuse charge layer is called the shear plane. The potential at this plane can be measured as the zeta potential ζ by applying shear stress to remove the diffuse charge layer. [Prob1994]

Figure 1.5 **a)** shows the development of the concentration profile in the BL, which was simplified as a linear correlation in Fig 1.3. During the operation of ED with increasing potentials, a characteristic current versus voltage relation can be observed with three different regimes, see Figure 1.5 **b)**. These regimes result from changing BL concentration profiles.

At potentials that lead to a current density smaller than the limiting current density, the BL consists of the EDL and the diffusion layer. The latter assumes the bulk electrolytes concentration at its border. Both anion and cation concentrations in the diffusion layer decrease linearly towards the EDL while keeping electroneutrality. During operation at limiting current densities, concentration polarization (CP) develops as the primary mass transport resistance. This resistance shows as a plateau region in the iV-graph interrupting the correlation of increasing potential with increasing current density. Both ion concentrations decrease to a minimum at the EDL. However, an even further increase in potential leads

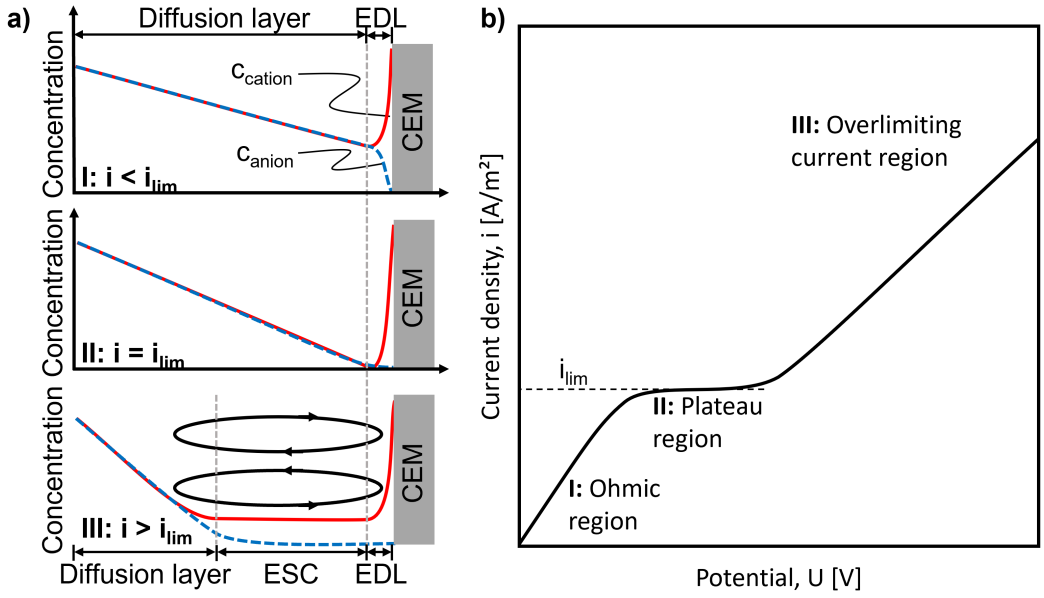

Figure 1.5: Development of concentration profiles between bulk and cation-exchange membrane surface with increasing potential. a) Illustrations of the courses of the anion and cation concentrations in the three different regions: **I:** Ohmic region ($i < i_{lim}$), **II:** plateau region ($i = i_{lim}$), and **III:** overlimiting current region ($i > i_{lim}$). Adapted from Mani and Wang [Mani2020]. **b)**Illustration of a typical current density versus voltage curve for an electrically-driven membrane process.

to the emergence of a new layer inside the BL that expands the diffuse charge layer [Baza2009]. This layer of extended space charge (ESC) extends the EDL's non-electroneutrality, reaching far into the diffusion layer. In this layer, electroconvective vortices, or simply electroconvection (EC), emerge that mix the whole domain and counteract the concentration polarization. Therefore, overlimiting current (OLC) densities become possible.

The emergence of EC results from a complex interaction of forces in the ESC region explained by the coupling of the Nernst-Planck, Poisson, and Navier-Stokes equations. This coupling leads to the mobile diffuse layer's electrokinetic interaction with an external electric field in the viscous shear layer near a charged surface. This interaction takes place in both directions. On the one hand, an electric field applied tangentially to a charged surface exerts a force on the diffuse layer's charged species. This force leads to the migration of the mobile ions. In an electroneutral

solution, the migration of counter-charged species balances out. However, the charge imbalance in the EDL, see Figure 1.4, allows a net migration of the accumulated species [Prob1994]. The viscous drag of ions on their surrounding solvent included in the Navier-Stokes equation then causes the liquid to flow. On the other hand, a forced movement of the electrolyte in the diffuse layer relative to the charged surface also induces an electric field.

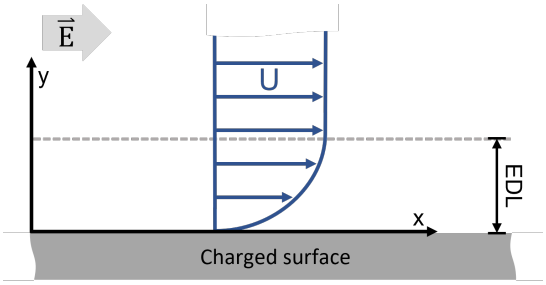

Figure 1.6: Electroosmosis close to a charged surface. Illustration of the velocity profile emerging in an electrolyte close to a charged surface under the influence of an electric field.

The case investigated in this thesis is that of an immobile, charged surface, the ion-exchange membrane, under the effect of an externally applied electric field. The electrolyte flow emerging from the charged surface's interaction with the electric field is named electroosmosis [Prob1994]. The electroosmotic velocity can be estimated from the integrated Navier-Stokes equation by neglecting all but the electrical forces, assuming an infinite plane surface and a no-slip boundary, and inserting Poisson's equation:

$$U = -\frac{e \cdot \zeta \cdot E_x}{\mu} \tag{1.3}$$

where U is the velocity parallel to the surface, e the electric charge, E_x the electric field component parallel to the surface, and μ the fluids viscosity [Prob1994]. A graphical representation of this phenomenon is illustrated in Figure 1.6.

Eq. 1.3 requests an electric field component parallel to the charged surface for velocity generation, a situation that would not exist in an ideal ED setting. However, electrically induced electrolyte motion can still be observed [Rubi2008; Kim2007; Yoss2008]. One explanation is the existence of membrane heterogeneities in geometry, surface charge, or conductivity that result in an uneven charge and, therefore, electric field distribution [Rubi1988; Rubi1991]. Following, local electric field deviations parallel to the surface lead to a net motion of the fluid [Rubi2000].

Dukhin [Dukh1991] also describes a particular case of electroosmosis that becomes possible at the strongly polarized ESC layer. The charge imbalance of this layer, similar to a charged surface, was also found to power electroosmotic fluid motion if subject to a parallel electric field. Additionally, the allowed slip between fluid layers, contrary to the no-slip assumption at solid interfaces, reduces friction and leads to stronger electroosmotic forces. Literature defines the emergence of electroosmosis at the membrane surface as electroosmosis of the first kind, and that at the ESC region as second kind or Dukhin mechanism [Niko2014].

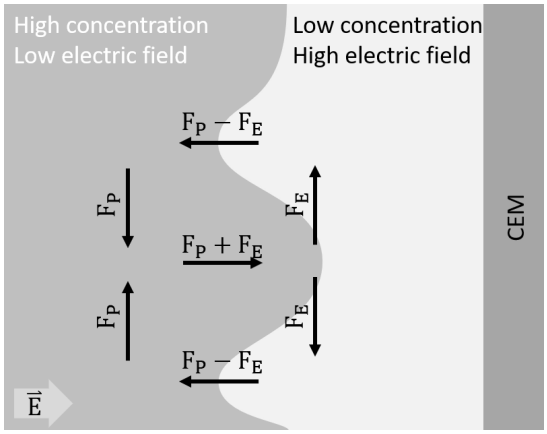

Figure 1.7: Forces acting during electroosmosis of the second kind. The illustration depicts the force balance between the forces resulting from the electric field (F_E), namely migration and electroosmosis, and the pressure forces (F_P). Adapted from Druzgalski and Mani [Druz2016].

Compared to a solid surface, the mobility of the ESC region further results in two mechanisms that aid the formation and sustain of EC. First, Rubinstein and Zaltzman [Rubi2000] showed that electroosmosis of the second kind emerges even at perfectly homogeneous surfaces when a mobile

ESC layer is present. They found that minor perturbations in the electric charge or electric field inside the ESC layer already cause lateral fluid motion. Second, once inhomogeneities occur, the induced fluid motion results in local pressure gradients as given from the Navier-Stokes equation which is depicted in Figure 1.7. These pressures lead to fluid motion towards the bulk, opposing the force of the electric field. Continuity demands that the initial electroosmotic fluid motion is compensated by a convective transport of high-concentrated bulk electrolyte towards the membrane. Above a certain threshold, this transport acts as a positive feedback mechanism that sustains and enhances the perturbation of the ESC layer [Zalt2007].

Apart from the two types of electroosmosis also the instability of the quasi-neutral bulk was hypothesized as a driving force for electroconvection. A general conclusion seems to be that EC of the ESC region plays the dominant role at highly selective surfaces while bulk electroconvection dominates at weakly selective surfaces [Rubi2015; Abu-2016; Mani2020].

Other mechanisms, besides EC, also take part in the current increase of the OLC [Zabo1998]. The first hypothesized explanation for the OLC was an increased ion availability due to water dissociation into H^+ and OH^- ions at the depleted membrane surface. The dissociation is especially evident at anion-exchange membranes due to catalysis by their functional groups [Zabo1988; Tana2010]. However, while water dissociation plays a role in the OLC region and counterbalances the current density increase of EC [Niko2017; Mani2020], its share of the OLC is small compared to EC [Niko2014]. The central role of EC was also proven in the famous experiment of Maletzki, Rösler, and Staude [Male1992] who immobilized the boundary layer close to a cation-exchange membrane using an agarose gel.

The conclusion that EC is the dominant mechanism in the OLC region and its interaction with water dissociation leads to the need to simultaneously control both phenomena to expand the operation range of electrically-driven membrane processes to the OLC region in industrial settings. The

following section summarizes the current state of the art regarding the steps necessary for this proposition.

1.4 Electroconvection

Initial theoretical investigation of EC dates back only to the end of the 20th-century. Rubinstein and Zaltzman first described EC as a hydrodynamic instability in their pioneering publications [Rubi1979; Rubi1988; Rubi2000; Zalt2007].

Due to its potential for significant improvements in the efficiency of electrically-driven membrane processes, EC is the subject of experimental and numerical studies that aim to visualize and quantify its chaotic hydrodynamics. Rubinstein et al. reported the first experimental 2D visualization of EC proving its existence [Rubi2008]. Other studies also analyzed EC by optically recording tracer substances in 2D [Yoss2008; Yoss2009; Kwak2013a; Kwak2013b; Kim2016]. Kang and Kwak [Kang2020] visualized the structural change of EC in the overlimiting current region with and without flow parallel to a membrane surface with 3D confocal microscopy. However, all these studies lack quantification of the concentration or velocity field dynamics of EC, which is important for developing physical correlations.

1.4.1 Quantification of electroconvection

Quantification of EC is possible only in intensive direct numerical simulations (DNSs) or experiments using special equipment. DNSs simultaneously solve the Navier-Stokes, Nernst-Planck, and Poisson-Boltzmann equations with highly nonlinear behavior resulting in high computational cost even for small geometries and short simulation times [Mani2020].

Druzgalski et al. analyzed and compared the statistics of chaotic EC from 2D to 3D results in an attempt to derive energy spectra needed for the development of a statistically averaged reduced-order model [Druz2013;

Druz2016]. Such a statistically averaged model enables low-cost simulations in the overlimiting regime for process optimization [Mani2020]. Today, process development for electrically-driven membrane processes is limited to the Ohmic region or the fitting of the overlimiting transport using a reduced-order parameter similar to a Schmidt number [Stod2014; Zour2015]. Druzgalski et al. also found qualitative and quantitative differences in their 2D and 3D simulations, suggesting the need for a 3D view on EC. However, the required fine resolution in space and time limited their simulations to small geometries and short time spans only. Therefore, the ability to extrapolate their conclusions to the length and time scales of industry-relevant devices remains unclear until experimental results of the 3D velocity field are available.

Valenca et al. reported an experimental methodology for quantifying the velocity field of EC in the cross-section of the CP layer by particle image velocimetry (PIV) in 2D [Vale2015]. They correlated the vortex size and rotational speed with the current density. The first analysis of the 3D vortex field on EC was reported by Demekhin et al. for 3D direct numerical simulations (DNSs) [Deme2014]. They reported a structural change of EC from vortex rolls to vortex rings which can only be observed in 3D. Consequently, a methodology for experimentally observing and quantifying the 3D velocity field of EC is inherently needed to expand the physical knowledge of its hydrodynamics.

1.4.2 Electroconvection at heterogeneous interfaces

While the above literature proves that EC indeed fuels the overlimiting current regime of electrically-driven membrane processes, another continuing challenge is the control of EC for application of the OLC in industry-relevant settings. In general, the limiting current density and the plateau region's length depend on the ion concentration, distance between bulk electrolyte and membrane, and the membrane characteristics [Mani2020]. EC is further known to be influenced by temperature gradients [Benn2018d], gravity [Kara2016], electrolyte viscos-

ity [Li2019], a pulsed electric field [Mikh2016; Buty2020], the electrolyte composition [Gil2018; Rogh2020], and the membrane surface properties [Abdu2014].

In general, a heterogeneous membrane surface can lead to a shorter and later plateau and a decreased resistance in the overlimiting current region [Rubi1988; Zabo1993; Choi2001; Niko2019]. Heterogeneity in surface geometry [Bals2007a; Bals2010; Pham2012; Benn2018a; Mare2018], conductivity [Mish1998; Volo2005; Davi2016; Zabo2017; Neba2018], hydrophobicity [Korz2016], and zeta potential [Bidd2004; Wess2014; Guan2021] have been shown to have a great influence. Additionally, Mareev et al. [Mare2018] connected the inhomogeneity of different commercially available membranes to inhomogeneity of the electric field at those membranes.

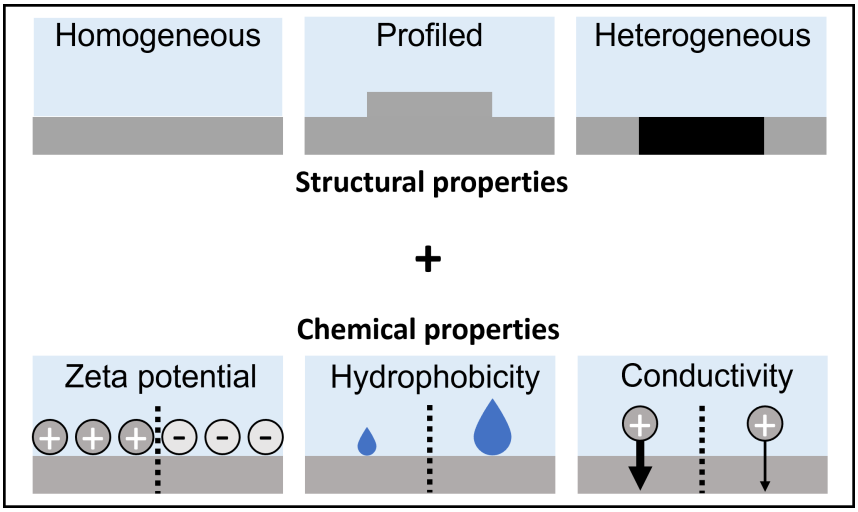

Figure 1.8: Collection of the influence factors on electroconvection. The influence factors on electroconvection are divided into structural properties and chemical properties of the membrane. The blue and orange zones indicate the change in chemical properties.

The knowledge gained from the above observations, summarized in Figure 1.8, led to research on tailored membrane modifications in attempts to control the plateau region and overlimiting current [Camp2018; Pawl2019; Went2020].

The pioneering works of Zabolotskii, Loza, and Sharafan [Zabo2005] and

Balster et al. [Bals2007a] confirmed the theoretical predictions that membrane undulations of the size of the boundary layer lead to a shortened plateau length [Rubi1991].

Valenca et al. [Vale2018a] recorded the velocity and orientation of EC vortices at geometric patterns on a cation-exchange membrane, again using 2D PIV. The experiments showed that the rotation of vortices was directed towards the patterns' valleys. Overall, the pattern structure led to a decrease of the system's resistance of about 50%.

A similar observation was made by Davidson, Wessling, and Mani [Davi2016] in 2D DNSs at a membrane patterned with non-conductive patches. Vortices located at and rotated towards the pattern structure. The optimal pattern length and their spacing, for a stable vortex structure with the largest current density, correlated with the diffusion boundary layer's height resulting in a surface coverage of 50%. They also reported that the vortex height is limited by its width. In an experimental study, Benneker et al. [Benn2016] used ion conductive nanoslots between unconductive material to experimentally investigate the build-up of EC in 2D. They concluded that distortions in the electric field could have a significant impact on the desalination performance. Nebavskaya et al. [Neba2018] reported the impact of nonconducting strips on the limiting current density of homogeneous AEMs. They found an optimal surface coverage of about 10% which deviates of the numerical results of Davidson, Wessling, and Mani [Davi2016].

While changes in surface charge and conductivity can be investigated separately in simulations, most membrane modifications in experiments achieve a superposition of multiple heterogeneities [Neba2017; Pism2019; Rogh2019].

Pismenskaya et al. [Pism2019] showed that the sizes of electric and geometric heterogeneities of the membrane surface influence the current density confirming the best results with sizes approaching the diffusion boundary layer thickness.

Kim, Kim, and Kwak [Kim2021] ranked the performance of differently shaped structures put on top of the membrane surface, similar to spacer structures, under forced flow. They found that a segmentation of the bound-

ary layer, which creates stagnant regions, is beneficial for the build-up of EC. Square patterns resulted in the highest vortex intensity in the overlimiting regime.

We presented a method to engineer the surface geometry and chemical topology of membrane surfaces in a controlled manner [Rogh2019]. An ink-jet printing technique was used to apply patterns such as circular patches of polymer microgels with varying zeta potential. Such membranes patterned with circular patches out of poly(2-vinylpyridine) (P2VP) doubled the limiting current density with a 40% reduced plateau length and only slightly increased membrane resistance. The hypothesis behind this great success was a combination of an early start of EC even at limiting current densities, the ion conductivity of the pattern, and an altered rotational direction due to the direction of the surface charge gradient. Additionally, a 3D structure most probably also leads to a 3D vortex pattern compared to the 2D structures of Valenca et al. and Davidson et al. [Vale2018a; Davi2016]. However, this study was limited to investigations of the macroscopic effect of the membrane modification of the system's electric properties. Therefore, the physics behind this modification's success is still unclear but could be revealed by experimental analysis of the 3D vortex field.

1.4.3 Electroconvection in spacer-filled channels

The advance in controlling EC's effectiveness with membrane modifications is a large step towards introducing the OLC region as a feasible process regime in industry. However, industry-scale processes include and combine further influencing factors like forced flow through spacer-filled, high-aspect-ratio compartments. Additionally, electrolyte impurities, membrane scaling due to insoluble salt species' formation, and gas evolution by water splitting are challenging, especially at overlimiting current densities. Currently, industrial processes are efficiently run only at underlimiting current densities. However, operation at high current densities in smaller

membrane modules would significantly decrease investment costs. Therefore, the complex interaction of EC, spacer-altered hydrodynamics, and water splitting in the OLC regime is of particular interest.

In a pumped electrolyte, Kwak et al. [Kwak2013a] visually analyzed EC vortices' behavior using a microchip. They observed that electroconvective vortices move along the shear flow. Additionally, Kwak et al. [Kwak2013b] found that the vortex movement speed is independent of applied voltage. Their research confirmed that electroconvection occurs in application-oriented systems in which the boundary layer is primarily affected. Pham et al. [Pham2016] reported the 3D structure of EC vortices under flow in DNSs. Their simulation showed that the vortices move as helices along with the flow over the membrane surface. However, both studies neglected the presence of spacers. Guan, Riley, and Novosselov [Guan2020] confirmed the organizing effect of shear flow on the 3D vortex structure of EC suppressing structures in the perpendicular flow direction. This effect might be of importance when considering the interaction of EC with the flow conditions in spacer-filled channels.

Various studies analyzed the effect of different flow conditions on ion transport in ED stacks. It becomes evident that shear flow reduces the boundary layer thickness leading to shorter diffusion lengths. However, electroconvection is also suppressed [Tana1991; Khai2011; Urte2013]. Tanaka [Tana2012] concluded that the ion transport in the boundary layer of a static electrolyte is governed by gravitational or electro convection while migration and diffusion dominate in a thin boundary layer of a pumped electrolyte.

Similar to most membrane processes, spacers are used in industrial ED set-ups to expand the process operational range. Spacers are open woven structures placed in the flow channels which increase mixing to counteract CP and separate the membranes in a membrane stack. The increased mixing of the bulk phase in channels with spacers reduces the boundary layer thickness even further. As a result, the diffusion length is shortened, ions

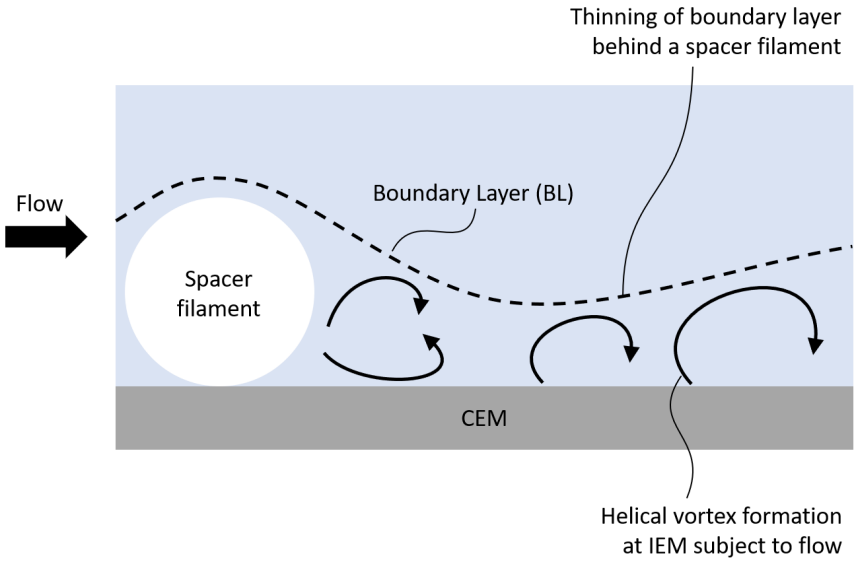

Figure 1.9: Interplay of spacer hydrodynamics and electroconvection. Theoretical illustration of the change in the course of the boundary layer and the resulting vorticity behind a single circular spacer filament.

can reach the membranes faster, and the current is increased [Kim2011; Fimb2010].

In industry-relevant 2D and 3D simulations, Fimbres-Weihs and Wiley [Fimb2007] identified differences in mass transfer enhancement of non-woven net spacers in a membrane channel of a pressure-driven process. They stressed the importance of 3D effects such as stream-wise vortices, open span-wise vortices, and higher wall shear rates vertically to the bulk flow direction. Another correlation in 3D simulations was revealed between locations of highest mass transfer and the presence of both stream-wise and span-wise vortices. Since these simulations considered a pressure-driven process, the additional effect of EC was omitted.

The decrease of the boundary layer thickness raises the question if electroconvective vortices even emerge at high currents in such small diffusion layers. If vortices are present, there might be competitive effects on the current. On the one hand, spacers increase the current by reducing the boundary layer thickness [Kim2011]. On the other hand, EC increases the current by mixing the boundary layer. The strength of EC is also dependent on the boundary layer thickness [Prob1994]. Therefore, an effective spacer

presumably suppresses EC to a minimum by minimizing the boundary layer thickness. However, spacers also introduce more complex flow conditions like vortex shedding or dead zones. One could imagine strong EC appearing in such regions of low flow velocity as illustrated in Figure 1.9. Early research in this field was dedicated to analyzing the effect of spacer-altered hydrodynamic conditions in flow-through cells [Cowa1959; Belf1972]. Conductive spacers were shown to be especially effective for increasing the limiting current density [Bals2010].

Tadimeti et al. [Tadi2016] modeled a spacer-filled electrodialysis channel in 2D. Their results show a high dependency of the ion removal on the flow profile in the channel. Additionally, they found that the boundary layer thickness is reduced to a minimum in corrugated membrane channels. Experimental studies of the hydrodynamics in a spacer-filled ED channel are also limited to 2D visualization [Kim2017; Kim2021]. Kim et al. [Kim2017] showed the impact of hydrodynamic change for varying spacer placement on the ion transfer. They reported that a central positioning of spacer filaments results in an about 40% limiting current increase. However, the study was limited to 2D parallel rods instead of a 3D woven spacer structure with only low flow velocities. These rods also had small diameters compared to the channel height, which leaves extrapolation to industry-relevant conditions an open question. They also only reported the influence in the limiting current regime without extension of their experiments to the OLC regime.

For effective use of the OLC in industrial electrically-driven membrane processes, knowledge of the combined interaction between EC and spacers' hydrodynamic impact in relevant length and time scales is still needed. Their possible synergy at large overlimiting currents and high flow rates would enable maximizing the hydrodynamic ion transport. As stated in Sec. 1.3, a promoted hydrodynamic current increase would shift the balance with unwanted water splitting in a favorable direction.

1.5 Scope of the thesis

This thesis aims to experimentally reveal the 3D features of the electroconvective (EC) vortex field that emerges at an cation-exchange membrane at overlimiting current densities. When the underlying physics of EC in industry-relevant settings are fully understood, the operational range of potential-driven membrane processes can be extended to the overlimiting current regime. Membrane modules also need to be optimized for operation in the overlimiting current region. Current models that include EC only resolve small geometries and short times far from scales found in realistic devices. Therefore, EC's statistics need to be fully understood to derive statistically averaged models comparable to turbulence modeling. Such models would reduce the computation costs to a fraction of the current demand and increase the possible domain size to realistic geometries.

Another challenge poses the elimination of the energy efficiency loss due to the plateau region. An earlier occurrence of EC will lead to a shortened plateau or even the direct transition from the ohmic to the overlimiting current region. This jump in efficiency would drastically reduce the needed membrane area and, therefore, the investment costs of most electrically-driven membrane processes.

The last step will be extending the before-mentioned knowledge to industry-like systems with typically small channel heights and spacer-filled channels. The hydrodynamic interaction of turbulence-promoting spacers and boundary layer-mixing EC is still only slightly touched in literature and application.

To tackle these challenges, we developed an experimental set-up utilizing micro particle tracking velocimetry (µPTV) to record and quantify the time-resolved 3D vortex field developing during electroconvection. With this set-up, we measured EC's hydrodynamics in a static electrolyte over a range of overlimiting currents and revealed their statistics.

In combination with a direct numerical simulation approach, this technique further allowed for the determination of the underlying hydrodynamic

mechanisms of a membrane surface modification that previously demonstrated to significantly shorten the plateau region [Rogh2019]. The modification method utilizes precise surface patterning of membranes with microgel suspensions that introduce a regular surface charge inhomogeneity. However, the influence of the modification on the formation of electroconvection is still unknown.

Lastly, we extended the measurements to flowing electrolytes in a spacer-filled channel to investigate the interaction between electroconvection and the flow field influenced by the spacers. Velocity measurements of only flow through spacer-filled channels were already performed using a µPTV, proving the feasibility of the technique [Will2010].

Chapter 2: Methodical details introduces the comprehensive experimental method for the time-resolved recording of the 3D electroconvective velocity field near a cation-exchange membrane.

With this setup, we measured the steady-state velocity field at multiples of the overlimiting current density in **Chapter 3: Three-dimensional quantification of electroconvection** . In contrast to simulations, the experiments cover length and time scales typical for industrial applications. We visualized coherent vortex structures and revealed the velocity field changes and their statistics with increasing current density. Additionally, this method enables the evaluation of the rotation direction of vortex structures. The transition is characterized by changes in the rotation direction, mean square velocity, and temporal energy spectrum with only minor influence on the spatial spectrum. These findings indicate a more significant impact of EC's structural change on the mean square velocities and temporal spectra than on the spatial spectra. This knowledge is a prerequisite for developing resource-efficient simulation codes and engineering ion-selective surfaces that will extend the operation range of electrically-driven processes beyond the diffusion-limited Nernst regime.

The same set-up is used in **Chapter 4: Electroconvection at charged patches** to record the vortex field, its structure, and rotational direction at membranes modified with microgel patches. These patches introduce

a regular heterogeneity of the membrane surface charge, which causes charge-specific positioning of vortices in 2D simulations. This chapter reports the vortex field structure, its rotational direction, and the steady-state structural stability for membranes modified with two types of microgels varying in zeta potential. The results demonstrate that the microgels with the largest difference in zeta potential compared to the membrane material structure the vortex field and dictate its rotational direction. Even though no long-term structure is maintained, the vortex field still differs from the case of a bare membrane. Additionally, this modification offers complete control of the electroconvective vortex field during its build-up. These results emphasize the potential of specifically engineered membrane surfaces for overcoming the limitations of electrically-driven membrane processes.

Chapter 5: Interaction between spacer hydrodynamics and electroconvection reports a newly designed electrochemical module that allows to record the 3D electroconvective velocity field with forced flow and inserted spacer structures. The module is validated against the convectional module design used in **Chapter 3** and **Chapter 4**. We could show the superposition of the electroconvective and forced flow profiles at a low Reynolds number with and without inserted spacer. Overall, the superposition leads to decreased velocities. The forced flow profile seems to disrupt the cortex structure of electroconvection. With increasing Reynolds number, the flow profile of electroconvection gets further suppressed.

Chapter 6: Summary and outlook gives a summary of the results obtained in this thesis. The chapter analyzes new findings and existing challenges and concludes with an outlook on the way to commercial application of EC in industrial processes.

1.6 Publication information

This thesis's content and results originate from research conducted under the affiliations and positions of the author as a research fellow (Wissenschaftlicher Mitarbeiter) at DWI - Leibniz Institute for Interactive Materials e.V., and as a PhD candidate (Promotionsstudent) at RWTH Aachen

University. Both positions are associated with the Chair for Chemical Process Engineering (Prof. Dr.-Ing. Matthias Wessling), AVT.CVT RWTH Aachen University. The author and his co-authors have previously published parts of the content presented in this thesis. Parts of this thesis are taken from published material under copyright regulations also listed underthe author's ORCID ID: 0000-0002-4725-6607. Relevant publications are mentioned at the beginning of the respective chapters. In particular, the following publications shall be considered:

- [Rogh2019] F. Roghmans, E. Evdochenko, F. Stockmeier, S. Schneider, A. Smailji, R. Tiwari, A. Mikosch, E. Karatay, A. Kühne, A. Walther, A. Mani, M. Wessling, "2D Patterned Ion-Exchange Membranes Induce Electroconvection", *Advanced Material Interfaces*, 2019.

- [Stoc2021b] F. Stockmeier, M. Schatz, M. Habermann, J. Linkhorst, A. Mani, M. Wessling, "Direct 3D observation and unraveling of electroconvection phenomena during concentration polarization at ion-exchange membranes", *Journal of Membrane Science*, 2021.

- [Stoc2022] F. Stockmeier, M. Schatz, M. Habermann, J. Linkhorst, A. Mani, M. Wessling, "Measurement of Electrokinetically induced hydrodynamics at Ion-selective interfaces using 3D Micro particle tracking velocimetry (µPTV)", *MethodsX*, 2022.

- [Stoc2021a] Submitted: F. Stockmeier, D. Felder, S. Eser, M. Habermann, P. Perić, S. Musholt, K. Albert, J. Linkhorst, M Wessling, "Localized Electroconvection at Ion-Exchange Membranes with Heterogeneous Surface Charge", *Under Review in Nature Materials, Preprint available at Research Square*.

- In preparation for publication: F. Stockmeier, L. Stüwe, E. Evdochenco, N. Köller, S. Brosch, C. Kneppeck, S. Musholt, K. Albert, A. Kovalenko, V. Nikonenko, M. Urtenov, J. Linkhorst, and M. Wessling, "Interaction Between Spacer-Altered Bulk Hydrodynamics and Electroconvection", *Journal to be decided*.

- This work received funding from the European Research Council (ERC) under the European Union's Horizon 2020 research and innovation program (grant agreement no. 694946).
- The Deutsche Forschungsgemeinschaft (DFG, German Research Foundation) supported this work through the projects SFB 985 Functional Microgels and Microgel Systems in project B6, project no. 191948804 and project no. 430046158.
- The measurements were conducted with a high-speed stereomicroscope PIV funded by the Major Research Instrumentation Program according to Art. 91b GG in the Research Building NW1481006 "NGP2 – Center for Next Generation Processes and Products", project no. 319121241.
- Simulations were performed with computing resources granted by RWTH Aachen University under projects thes0630, thes0631, and thes0698.

This thesis also contains data based on the following student theses:

- Benedikt Perniok, Bachelor's thesis, "Electrokonvection at modified ion-exchange membranes", 2019.
- Lorenz Aldefeld, Bachelor's thesis, "Simulation of 3D electroconvection at ion-exchange membranes", 2019.
- Fabian Edwin, Bachelor's thesis, "Electroconvection at microgele-modified ion exchange membranes", 2019.
- Steffen Eser, Bachelor's thesis, "Simulation of electroconvection at patches on ion-exchange membranes", 2019.
- Michael Schatz, Master's thesis, "Measurement of the 3D electroconvective flow field at modified ion-exchange membranes using µPIV", 2019.

- Tarvo Schwager, Master's thesis, "CFD simulation of vortex formation at modified ion exchange membranes with microstructured surfaces", 2019.
- Malte Habermann, Master's thesis, "3D flow field stability of electroconvection at modified ion-exchange membranes analysed by µPTV", 2020.
- Christian Kneppeck, Master's thesis, "Characterization of electroconvection in a cross-flow module with and without spacers using 3D-µPTV", 2021.

2

Methodical details

Parts of this chapter have been published as:
Felix Stockmeier, Michael Schatz, Malte Habermann, John Linkhorst, Ali Mani, and Matthias Wessling, "Direct 3D observation and unraveling of electroconvection phenomena during concentration polarization at ion-exchange membranes", *Journal of Membrane Science*, 2021
DOI: 10.1016/j.memsci.2021.119846

Felix Stockmeier, Michael Schatz, Malte Habermann, John Linkhorst, Ali Mani, and Matthias Wessling, "Measurement of Electrokinetically Induced Hydrodynamics at Ion-selective Interfaces using 3D Micro Particle Tracking Velocimetry", *MethodsX*, 2022
DOI: 10.1016/j.mex.2022.101814

Parts of this chapter are submitted as:
Felix Stockmeier, Daniel Felder, Steffen Eser, Malte Habermann, Petar Perić, Stephan Musholt, Katharina Albert, John Linkhorst, and Matthias Wessling, "Localized Electroconvection at Ion-Exchange Membranes with Heterogeneous Surface Charge", *Under Review in Nature Materials*, 2021
Preprint available at Research Square as DOI: 10.21203/rs.3.rs-1093972/v1

Parts of this chapter are in preparation for publication:
Felix Stockmeier, Lucas Stüwe, Elizaveta Evdochenko, Niklas Köller, Sebastian Brosch, Christian Kneppeck, Stephan Musholt, Katharina Albert,

John Linkhorst, and Matthias Wessling, "Interaction Between Spacer-Altered Bulk Hydrodynamics and Electroconvection", *Journal to be decided*

This thesis aims at the investigation of the 3D velocity field of electroconvection (EC) and its interaction with surface-modified membranes or spacer structures in application-oriented modules. The basis for this investigation is an experimental methodology for recording the 3D EC velocity field close to a bare or modified cation-exchange membrane with or without forced flow. The last sections describe the processing of velocity data and nondimensionalization of the results to enable comparability between simulations and experiments.

2.1 Electrochemical cell

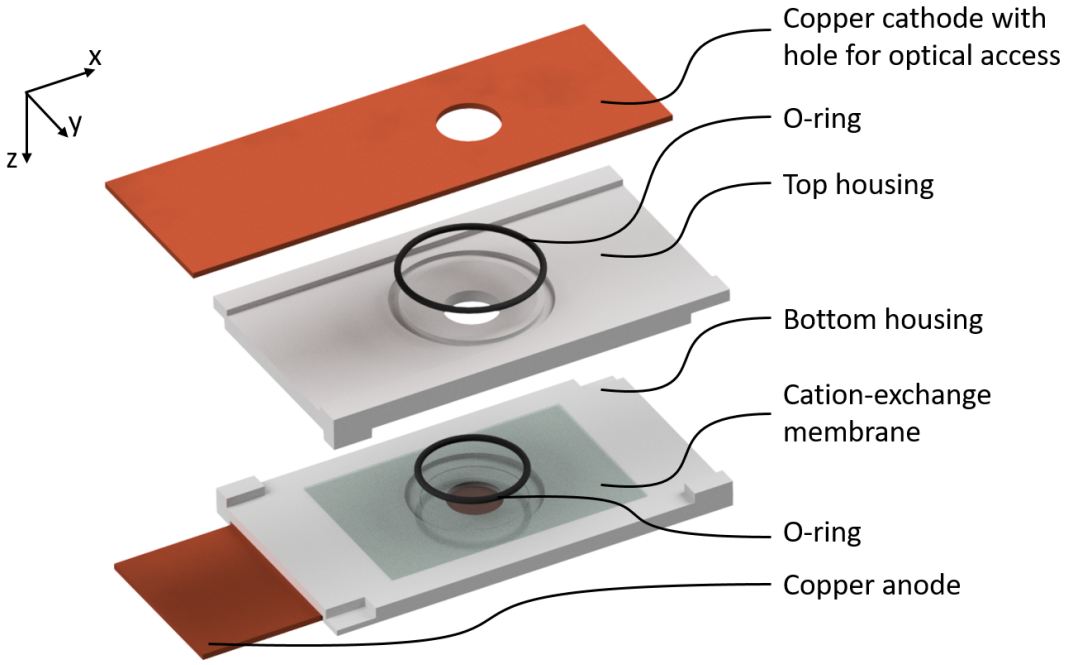

Figure 2.1: Cell design for electrochemical experiments with simultaneous µPTV recording. The electrochemical cell consists of two 3D printed housing parts which are sealed with O-rings against two copper electrodes and a Nafion N117 membrane. The cathode has a circular hole with a diameter of 9 mm to allow optical access. The hole is sealed with a microscope glass slide, which is not shown in the rendering, on top of the electrode.

The electrochemical experiments were conducted in the experimental cell shown in Figure 2.1 which is suitable for electrochemical experiments

with simultaneous recording of the evolving 3D velocity field using microparticle tracking velocimetry (µPTV). The cell is based on the publication of Linz et al. [Linz2021] and consists of a Nafion N117 (Chemours, Wilmington, Delaware, USA) cation-exchange membrane sealed between two housing parts. The transparency of the membrane allows for imaging of buoyancy stable EC through the membrane [Kara2016; Vale2017b]. Two copper plates (25 mm $\times$ 75 mm $\times$ 0.5 mm) seal the top and the bottom of the chip and act as electrodes in each half cell. The cathode has a circular hole (d = 9 mm) and is glued to a glass slide to enable optical access. This setup forms electrolyte chambers above and below the membrane, which are filled with 1 mM copper sulfate ($\mathrm{CuSO_4}$) as the electrolyte. The bottom chamber has a height of 0.8 mm, matching the maximum focal depth, and a diameter of 8 mm, resulting in an aspect ratio of 10. Such a large aspect ratio is desired to prevent the confinement of the EC vortices [Tsai2004; Davi2016].

A cell comprising two copper electrodes, a cation-exchange membrane, and $\mathrm{CuSO_4}$ in aqueous solution as electrolyte is a simple and well studied electrochemical system for evoking EC [Vale2015; Gu2019]. In this system, $\mathrm{CuSO_4}$ dissociates to $\mathrm{Cu^{2+}}$ and $\mathrm{{SO_4}^{2-}}$ and both electrodes favor copper deposition and dissolution as faradaic reactions [Deng2013]:

$$\mathrm{Cu^{2+}} + 2\,\mathrm{e^-} \rightleftharpoons \mathrm{Cu} \tag{2.1}$$

During operation, copper is dissolved at the anode, transported through the membrane, and deposited on the cathode. Additionally, this reaction system limits gas evolution at the electrodes and the membrane to a minimum, which ensures stable reaction conditions and clear optical access without gas bubbles.

The copper ions moving towards the cathode result in an ion flux i per membrane area also describes as the current density. The limiting current density of the process, described in Figure 1.5, can be derived from the one dimensional Nernst-Planck equation [Prob1994] formulated for the liquid

and membrane at the phase boundary:

$$J^{\text{liq}} = -D\frac{\partial c(x)}{\partial x} + \frac{i \cdot t_E}{z \cdot F} \tag{2.2}$$

$$J^{\text{mem}} = \frac{i \cdot t_M}{z \cdot F} \tag{2.3}$$

F is Faraday's constant, z the ionic valence, and D the diffusion coefficient. The transport numbers in the membrane and electrolyte t_M and t_E describing the ion velocity difference are 0.96 and 0.4, respectively [Vale2017a].

At the boundary, the ion flux through the liquid and the membrane phase needs to be equal ($J^{liq} = J^{mem}$) which yields:

$$i^{\text{boundary}} = \frac{z \cdot F \cdot D}{t_M - t_E} \cdot \frac{\partial c(x)}{\partial x}|_{x=0} \tag{2.4}$$

Further, the concentration gradient in the diffusion boundary layer of the liquid between the bulk and the interface can be approximated as a linear gradient between the bulk and interface ($\frac{\partial c(x)}{\partial x} = \frac{c_B - c_I}{\delta}$). At the limiting current density, the concentration at the interface is assumed to approach zero ($c_i \approx 0$) resulting in the following equation for the limiting current density first derived by Peers [Hill1956]:

$$i_{\text{lim}} = \frac{c_B}{\delta} \cdot \frac{F \cdot z \cdot D}{t_M - t_E} \tag{2.5}$$

According to Valenca [Vale2017a], the bulk concentration c_B is approximated with a linear gradient between electrode and membrane as twice the electrolyte starting concentration c_0 in the anode chamber. For a 1 mM $\mathrm{CuSO_4}$ solution, current densities larger than i_{lim} = 0.73 A m^{-2} will result in the EC vortex formation close to the membrane of the anode

chamber [Vale2015].

2.2 Micro particle image velocimetry

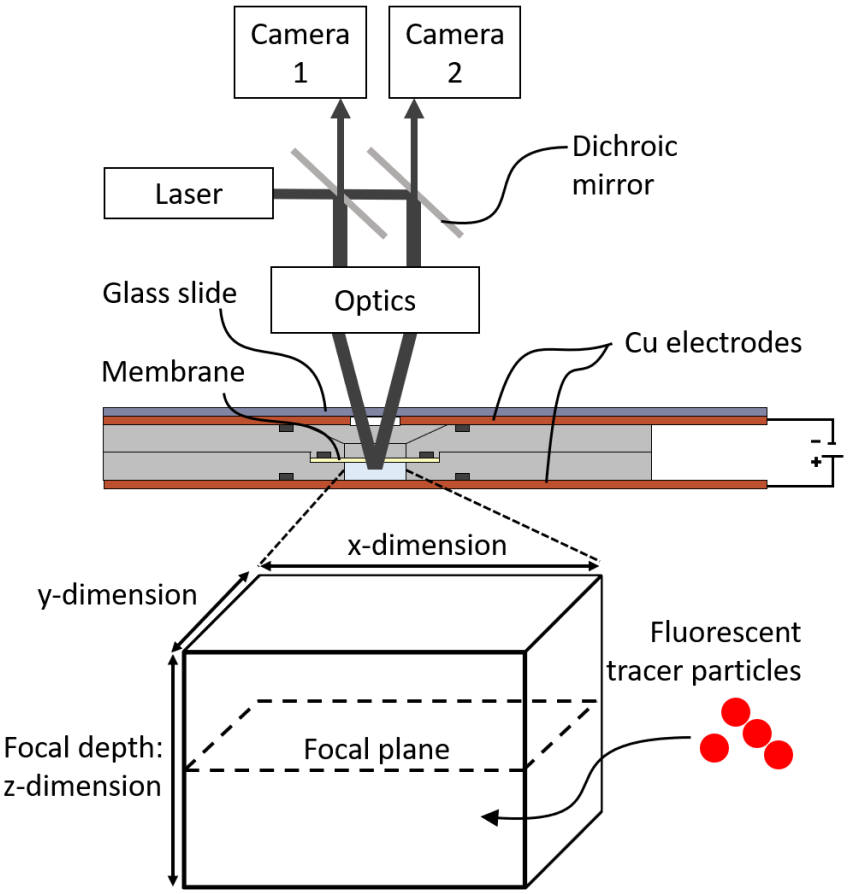

Figure 2.2: Schematic illustration of the setup for stereo micro particle image velocimetry. The setup for stereo micro particle image velocimetry consists of a laser that illuminates tracer particles in a sample volume through a stereo microscope which splits the laser beam in two separate beams. The fluorescence response returns through the microscope and is recorded by two slightly angled high-speed cameras. Returning laser light is blocked by a high-pass filter. This technique allows the recording of tracer particles in a 3D volume.

We use micro particle tracking velocimetry (µPTV), an optical technique for measuring fluid flow in millimeter-scale geometries [Sant1998], to record the velocity field of EC during our experiments. When using this method, tracer particles are illuminated by a high-frequency

532 nm Nd:YAG laser (DM150, Photonics Industries International Inc.) and recorded by two high-speed cameras (Phantom VEO 710L, Vision Research Inc.) through a stereo microscope (SteREO Discovery.V20, Carl Zeiss Microscopy Deutschland GmbH, Germany) containing a 1× objective (Plan-Aprochromat 1×, Carl Zeiss Microscopy Deutschland GmbH, Germany), see Fig 2.2. The cameras record the resulting particle images inside the microscope's focal depth from two different viewing angles. With our setup, the recorded volume at a magnification of $5.12\times$ and a halfway closed aperture has a size of 4.9 mm×3.1 mm×0.8 mm with 1280 px×800 px resolution in x- and y-direction. The depth of the recorded volume of 0.8 mm matches the depth of our electrochemical cell's anode chamber. Therefore, it is possible to reconstruct the full velocity field of EC between membrane and anode.

2.3 Electrochemical experiments with velocity recording

To conduct simultaneous electrochemical and µPTV experiments, the electrolyte in the anode chamber is seeded with 0.001 wt% inert, fluorescent polystyrene microspheres (Thermo Scientific, Waltham, MA, USA). These tracer particles have a diameter of 3.2 µm and a Zeta potential of −14.9 mV measured with a Malvern Zetasizer Nano ZS (Malvern Panalytical Ltd), which are comparable to the study of De Valenca et al. and Warren et al. [Vale2015; Warr2021]. Similar to both studies, the electrophoretic velocity of the particles is at least an order of magnitude lower than the velocity gain due to the EC vortices. In contrast to these studies, the microscope is focused below the membrane in the middle of the anode chamber enabling to record the particle tracks over the whole z-dimension of that chamber. The experiments are conducted without forced flow and electrolyte movement only results from EC.

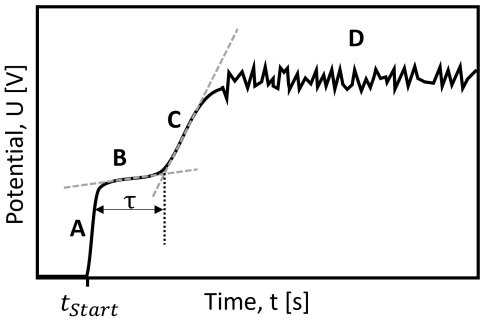

Figure 2.3: Illustration of a typical chronopotentiometric experiment in the overlimiting regime. The graph shows four phases: **A** Start of the experiment with ramp to Ohmic resistance. **B** Build-up of concentration polarization. **C** Depletion close to the membrane and evolution of electroconvection. **D** Overlimiting current sustained by electroconvection. Adapted from Krol, Wessling, and Strathmann [Krol1999].

The chronopotentiometric experiment are conducted at fixed multiples of the limiting current using a potentiostat (Interface 1010E, Gamry, Pennsylvania, USA). Figure 2.3 illustrates a typical potential response during a chonopotentiometric experiment in the OLC regime. For each potential, the time until CP is fully built-up and EC starts to develop can be calculated with Sand's equation, which is derived from Fick's second law [Sand1899; Krol1999; Prob1994]:

$$\frac{\partial c(x,t)}{\partial t} = D \cdot \frac{\partial^2 c(x,t)}{\partial x^2} \tag{2.6}$$

The solution of this equation requires a set of boundary conditions. The initial concentration in the whole domain is assumed homogeneous, the concentration at the bulk side of the diffusion layer ($x = \delta$) is assumed to equal the bulk concentration (c_B), and the concentration at the liquid-membrane-interface ($x = 0$) follows equation 2.4:

$$\begin{aligned} c(x=0,t=0) = c(x=\delta,t=0) &= c_0 \\ c(x=0,t) &= c_B \\ \frac{\partial c(x=0,t)}{\partial x} &= -\frac{i}{z \cdot F \cdot D} \cdot (t_M - t_E) \end{aligned} \tag{2.7}$$

By applying a Laplace transformation, assuming a constant current density, and a successive reverse transformation (the detailed numerical procedure can be found in Bard and Faulkner [Bard2000], pp. 307), Equations 2.6 and 2.7 result in [Sist1997; Bard2000; Vale2017a]:

$$c(x,t) = c_0 - \frac{i \cdot (t_M - t_E)}{z \cdot F \cdot D} \cdot \left[2\sqrt{\frac{D \cdot t}{\pi}} \cdot \exp\left(\frac{-x^2}{4 \cdot D \cdot t}\right) - x \cdot erfc\left(\frac{x}{2\sqrt{D \cdot t}}\right) \right] \quad (2.8)$$

For the concentration at the electrolyte-membrane-interface ($x = 0$), equation 2.8 yields:

$$c(0,t) = c_0 - \frac{2i \cdot (t_M - t_E) \cdot t^{1/2}}{z \cdot F \cdot D^{1/2} \pi^{1/2}} \quad (2.9)$$

The transition time at which $c(x,t) = 0$, equation2.9 assumes the form first derived by Sand [Sand1899]:

$$\tau = \frac{\pi D}{4} \cdot \left(\frac{c_0 z F}{t_M - t_E}\right)^2 \frac{1}{i^2} \quad (2.10)$$

Here, c_0 is the electrolyte's initial concentration in the anode chamber. The diffusion coefficient of the electrolyte D = 0.855 $\times$ 10^{-9} m^2 s^{-1} is calculated from both individual diffusion coefficients $D_{Cu^{2+}}$ = 0.714 $\times$ 10^{-9} m^2 s^{-1} and $D_{SO_4^{2-}}$ = 1.065 $\times$ 10^{-9} m^2 s^{-1} with the following equation [Lide2003]:

$$D = \frac{(z_+ + z_-) D_+ D_-}{z_+ D_+ + |z_-| D_-} \quad (2.11)$$

The + and - signs indicate the values for cation and anion, respectively. However, EC takes longer than the calculated transition time τ to reach a steady-state [Rogh2019]. Therefore, we analyze the flow well after the transition time in the steady sections of the chronopotentiometry to ensure evaluation of the steady-state.

2.4 Velocity processing

The recorded particle images are analyzed with the tools available in the software DaVis (version: 10.0.5.47779, LaVision GmbH, Göttingen, Germany). In a preprocessing step, static particle signals are removed by subtracting the time-averaged intensity for each pixel. For the reconstruction of the particle tracks, the Shake-the-Box algorithm is used [Scha2013; Schr2015]. However, experiments at current densities below $2 \cdot i_{lim}$ cannot be processed. Here, the particles move too slow and the velocities are too small to be detected.

A fine-scale reconstruction is used for transforming the particle tracks to velocities (u_x, u_y, u_z) on a regular grid. The fine-scale reconstruction is performed with the VIC# method implemented in the DaVis Software [Jeon2018; Schn2016].For our experiments, we chose a grid size of ten voxels, which results in reasonable computing times. Therefore, the final resolution of the reconstructed velocity fields is 128 px$\times$80 px$\times$21 px with a voxel size of 38.4 µm.

To visualize the vortex structure of EC, DaVis offers plotting coherent vortex structures with the λ_2-method [Jeon1995]. This method computes vortex core lines by evaluating the eigenvalues of the squared and summed symmetric and antisymmetric parts of the gradient velocity tensor. Coherent structures are visualized as isosurfaces at a specific eigenvalue λ_2.

2.5 Dimensionless numbers

To achieve comparability to the 3D DNSs of Druzgalski et al. [Druz2016]. We chose process parameters that best match their dimensionless numbers summarized in Tab. 3.1. The relevant dimensionless parameters concerning this comparison include: i) the applied voltage divided by the thermal voltage $\frac{V}{V_T} = \frac{Vze}{k_B T}$, ii) the Schmidt number $Sc = \frac{\mu}{\rho D}$, iii) the electrohydrodynamic coupling constant $\kappa = \frac{\epsilon}{\mu D} \cdot (\frac{k_B T}{ze})^2$, iv) the dimensionless Debye length $\lambda_d = \sqrt{\frac{\epsilon k_B T}{2c_b(zeL_z)^2}}$, and v) the aspect ratio $a = \frac{d}{L_z}$. Here, k_B, T, z, and e

are the Boltzmann's constant, temperature, ionic valence, and the electron charge, respectively. Furthermore, the electrolyte defines the permittivity ϵ, dynamic viscosity μ, diffusion coefficient D, and bulk concentration c_b. Lastly, d and L_z are the active membrane diameter and the distance between the membrane and electrode, respectively. We also plot our graphs with dimensionless values of time $t = \frac{t^*}{t_{diff}}$, velocity $u = \frac{u^*}{u_{diff}}$, and distance $l = \frac{l^*}{L_z}$ using the characteristic scales $t_{diff} = \frac{L_z^2}{D}$ and $u_{diff} = \frac{D}{L_z}$.

Out of these parameters, our main targets were a large channel aspect ratio, a large dimensionless Debye length, and the possibility to conduct experiments at large overlimiting currents, which is proportional to large applied voltages. Advantageous to simulation, our setup allows for dimensions and a Debye length found in practically relevant applications. This difference in Debye length of about three orders of magnitude leads to a smaller extended space charge region in the experiments and, thus, velocity generation closer to the membrane [Mani2020].

2.6 Velocity statistics

After exporting the velocity field data to MatLab (version: R2019b, The MathWorks Inc.), the mean square velocities is calculated as a spatial and temporal average in the steady-states of the experiments [Druz2013]:

$$\overline{u_i^2} = \frac{1}{N_t \cdot L_x \cdot L_y} \int u_i^2 \cdot dx \cdot dy \cdot dt \tag{2.12}$$

The equation includes the number of time steps N_t and the mesh points in x- and y-direction L_x and L_y.

The fluctuating velocity components are calculated by subtracting the temporal and spatial mean velocity from each velocity data point for evaluation of the temporal and spatial energy spectra. To this data, we apply a Hanning window. The Hanning window or Hann function is a weighting

function which is used to reduce the input signal from the middle of the x,y-domain towards its borders [Esse1986]:

$$w_i(n_i) = 0.5 \left(1 - cos\left(2\pi \frac{n_i}{N_i}\right)\right) \tag{2.13}$$

Here, n_i and N_i are the array of data points and the number of data points in x- or y-direction, respectively. The 2D window is created with $w_{x,y}(n_x, n_y) = w_x(n_x) \cdot w_y(n_y)$.

The fluctuating velocity components are further processed in a spectral analysis enabling the characterization of the energy dissipation in the system.

For spectral analysis, a Fourier transformation of the fluctuating velocity components over time or space is performed. The velocities, that were 1D Fourier transformed over time $\tilde{u_i}$, are then converted to temporal spectral energies and averaged in the x,y-planes with [Druz2013]:

$$E(z, \omega) = \frac{1}{2 \cdot N_t \cdot N_x \cdot N_y} \int |\tilde{u}_x|^2 + |\tilde{u}_y|^2 + |\tilde{u}_z|^2 dxdy \tag{2.14}$$

Here, N_t, N_x, and N_y are the number of data points in time, the x-direction, and the y-direction.

For spatial spectral analysis, a 2D Fourier transformation of each fluctuating velocity component in each z-plane for each time step is performed. The energy is normalized, and averaged over time:

$$E(z, k) = \\ \frac{1}{2 \cdot N_t} \cdot \frac{d^6}{(2 \cdot \pi)^3 \cdot L_x \cdot L_y \cdot L_z} \int |\tilde{u}_x|^2 + |\tilde{u}_y|^2 + |\tilde{u}_z|^2 dt \tag{2.15}$$

The result is integrated over annuli with a radius of $k = \sqrt{k_x^2 + k_y^2}$ and a thickness of one in the Fourier-space as schematically represented in Figure 2.4. Here, d is the mesh spacing, and L_x, L_y, and L_z are the domain

sizes in the x-, y-, and z-directions, respectively. This procedure results in energy graphs over the wavenumber k which is the spatial frequency in x,y-direction. During the integration, the mesh is refined by a factor of ten in both directions to generate smoother graphs.

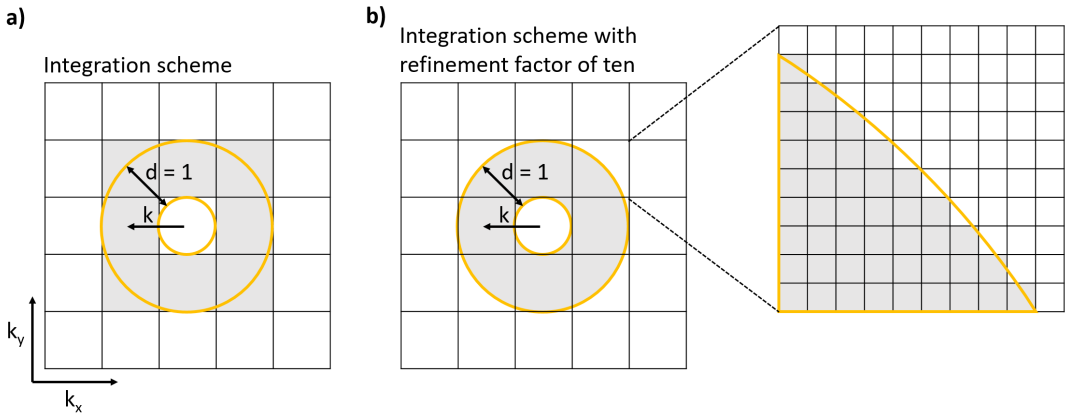

Figure 2.4: Graphical representation of the spatial spectra integration and refinement scheme. a) Example of the integration for k = 1. **b)** Example of the refined integration for k = 1. The detail on the right shows the selected fraction of the data point in one original pixel.

Figure 2.4 displays a graphical representation of the integration and refinement scheme for the spatial spectra also described by Druzgalski et al. [Druz2016]. On the left side (Figure 2.4 **a)**), the two yellow circles with a difference in radius of one form an annuls for integration. The wavenumber k increases from the center of the k-space in steps of one. The grey highlighted data points show the selection for the non-refined integration. In Figure 2.4 **b)**, an integration scheme with a refinement factor of ten in both directions is displayed. The refined integration results in a smoother graph especially for small wavenumbers by distributing the information in one cell between two adjacent annuli.

2.7 Governing equations of ion transport

This section outlines the equations that govern ion transport in electrically-driven membrane processes. These equations are also the basis for

the numerical model to predict the build-up of EC at a membrane with a heterogeneous surface charge, which is used and described in Chapter 4.

Throughout this thesis, the aqueous electrolyte is described as an incompressible, single-phase Newtonian fluid. The Navier-Stokes and continuity equations govern the conservation of its momentum [Prob1994]:

$$\begin{aligned} 0 &= -\nabla p + \mu \nabla^2 \mathbf{u} - \rho_E \nabla \mathbf{\Phi} \\ 0 &= \nabla \cdot \mathbf{u} \end{aligned} \tag{2.16}$$

Here, p is the pressure, μis the dynamic viscosity **u** is the velocity vector, ρ_E is the electric charge density, and Φ is the electrostatic potential. The studies of Yariv et al. and Drusghalski et al. showed that the Navier-Stokes equation's inertia term could be neglected for this physics problem [Yari2009; Druz2013].

The Nernst-Planck equation describes the ion transport under the action of an electric field within a low-ionic strength electrolyte.

$$\frac{\partial c_i}{\partial t} + \mathbf{u} \cdot \nabla c_i = \nabla \cdot (D_i \nabla c_i) - \nabla \cdot \left(D \frac{e z_i}{k_B T} c_i \nabla \mathbf{\Phi} \right) \tag{2.17}$$

where c_i is the concentration, $D = D^+ = D^- = 1 \times 10^{-9}\,m^2\,s^{-1}$ is the diffusion coefficient. Additionally, e is the elementary charge, z_i is the charge valence, k_B is the Boltzmann constant and T is the absolute temperature. The index i is used to mark each individual species in the electrolyte.

The electric potential distribution in a given domain can be computed from Gauss' law, ignoring polarization.

$$\nabla \cdot (\varepsilon \nabla \mathbf{\Phi}) = -\rho_E \tag{2.18}$$

with permittivity ε the charge density defined as

$$\rho_E = F\left(\sum_{i=1}^{m} z_i c_i\right) \tag{2.19}$$

where F represents Faraday's constant and m is the number of different ionic species.

2

3

Three-dimensional quantification of electroconvection

Parts of this chapter have been published as:
Felix Stockmeier, Michael Schatz, Malte Habermann, John Linkhorst, Ali Mani, and Matthias Wessling, "Direct 3D observation and unraveling of electroconvection phenomena during concentration polarization at ion-exchange membranes", *Journal of Membrane Science*, 2021
DOI: 10.1016/j.memsci.2021.119846

Felix Stockmeier, Michael Schatz, Malte Habermann, John Linkhorst, Ali Mani, and Matthias Wessling, "Measurement of Electrokinetically Induced Hydrodynamics at Ion-selective Interfaces using 3D Micro Particle Tracking Velocimetry", *MethodsX*, 2022
DOI: 10.1016/j.mex.2022.101814

3.1 Introduction

Ion-selective membranes are frequently used in industrial processes for water purification such as electrodialysis (ED) [Stra2010; Werb2016] and flow-electrode capacitive deionization (FCDI) [Gend2014; Romm2015; Tang2020] for water purification, and redox-flow battery systems [Park2017; Perc2020] for energy storage. In these processes, an electric potential between two electrodes acts as the driving force for ion transport through membranes in contact with an electrolyte. For small currents, the current density increases linearly with the applied potential. However, the transport stagnates at the limiting current density i_{lim} when concentration polarization (CP) leads to depletion of the Nernst diffusion layer close to the membrane, see Figure 1.5 **a)** [Niko2014]. This limitation is visible as a plateau region in a current density over potential plot in Figure 3.1.

When increasing the current density beyond i_{lim}, overlimiting currents emerge having their origin in a variety of superimposed phenomena, one of them being electroconvection (EC). Electroconvection can be observed as vortices, which convectively mix the boundary layer supplying the depleted layer with the ion-rich bulk solution, see Figure 1.5 **a)**. The increased ion concentration at the membrane allows for an overlimiting current beyond the diffusion limit, see Figure 3.1 [Mani2020].

Until now, quantitative studies on the hydrodynamics of EC were limited to computationally demanding 2D and 3D direct numerical simulations (DNSs) which unfortunately only offer limited length and time scales [Druz2013; Deme2014; Druz2016; Pham2016; Guan2020]: experimental quantification of velocity profiles could only be done using 2D experiments [Vale2015; Vale2017a; Warr2021]. In fact, understanding and controlling the hydrodynamics of EC is expected to facilitate mass transport observed as overlimiting currents. Multiple studies report membrane modification methods which result in an increased limiting current density or reduced plateau length. Further development of tailor-made modifications as developed by Roghmans et al. will expand the linear regime and

might extinguish the limiting plateau [Rogh2019]. This development will enable higher current densities resulting in lower membrane area required to achieve a desired desalination degree: this translates in a desired investment costs reduction. It is therefore obvious that understanding the details of the overlimiting transport, in particular EC, is a prerequisite for process optimization of an electrical-field driven membrane process. Also, understanding electroconvection's intricate details comprehensively is important to tailor membrane surfaces such that overlimiting can be actually utilized in practice.

3.2 Background

In a milestone paper of Rubinstein [Rubi2000], the authors predicted that the onset of electroconvection can be triggered at lower voltages if the surface of the membrane would be "wavy". This prediction has spurred research in understanding the phenomena itself, but also into the synthesis of new membrane surface topologies to avoid any potential drop in the plateau region prior to the overlimiting currents. With respect to experimental strategies to initiate early electroconvection, membrane modification methods developed by the Kuban research community have proven to be effective [Korz2016; Neba2017; Mare2018]. As early as 2007, Balster reported that line undulations on the membrane surface normal to the flow direction, having distances in the range of approximately 50-200 % of the boundary-layer thickness, lead to an earlier onset of the overlimiting current [Bals2007b]. Also 2D micropatterns of nanometer-thick lateral polyelectrolyte patches induce electroconvection, i.e. macroscopic electro-osmotic chaotic fluid instabilities [Wess2015]. Also Roghmans et al. described that inkjet printed microgel patterns induce electroconvection [Rogh2019]. Yet the work hypothesizes that the surface charge of the patterns may even determine the direction of vortices rendering them either effective or less effective for destabilizing the diffusion boundary layer and reducing the length of the plateau. Clearly, more experimental visualization methods are highly desired to elucidate and quantify the spatio-temporal fluid velocities during

electroconvection at the membrane/fluid interface.

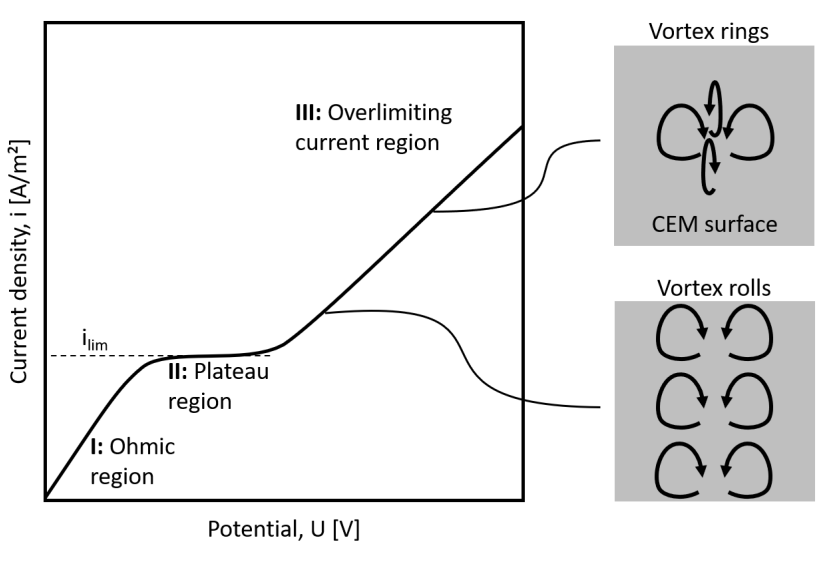

Figure 3.1: Stages of electroconvection along the current density over potential graph. Sketch of the current density over potential graph for an electrically driven membrane process. Three regimes appear the so-called the Ohmic, plateau, and overlimiting current regions. In the overlimiting region, two different vortex structures develop. First, EC appears as vortex rolls that order in a 2D fashion. At higher i/i_{lim}, the linear structure of vortex rolls breaks up into 3D vortex rings.

Historically, our 2D work on proving the existence of electroconvection through visualization with a particle imaging technique [Rubi2008] confirmed the predicted vortex-like features at the membrane/liquid interface with growing vortices at increasing current densities. Subsequently, De Valenca et al. quantified the 2D velocity field of EC in the cross-section of the CP layer [Vale2015; Vale2017a]. They correlated the vortex size and fluid flow velocity with the current density through the system. This approach was recently advanced by Warren et al. [Warr2021] who correlated the effect of the applied potentials and electrolyte concentrations to the 2D velocity field of EC. They focused their quantification on 2D flow phenomena for the characterization of electro-deposition phenomena by suppressing the evolution of 3D flow with their electrochemical chip's geometry. Therefore, their proposed chip had an aspect ratio non-existent in common electrochemical devices featuring a long membrane-to-electrode distance compared to the channel's width. Other studies also analyzed

EC by optically recording tracer substances in 2D but without quantification of velocities [Rubi2008; Yoss2008; Yoss2009; Kwak2013a; Kwak2013b; Kim2016; Bell2019]. Recently, Kang et al. visualized the structural transition of EC in the overlimiting current region with and without flow parallel to a membrane surface with confocal microscopy in 3D [Kang2020]. This transition from 2D vortex rolls towards 3D vortex rings, see Figure 3.1, was predicted by Demekhin et al. in the first 3D DNSs of EC [Deme2014]. Although qualitatively accurate, such confocal microscopy methods do not supply information on the 3D EC velocity field and its energy transfer.

The chaotic 3D velocity field of EC is up to now only accessible via intensive simulations simultaneously solving the Navier-Stokes, Nernst-Planck, and Poisson-Boltzmann equations [Mani2020]. In such a simulation, Druzgalski et al. analyzed and compared the statistics of chaotic EC form 2D to 3D results in an attempt to derive energy spectra needed for the development of a statistically averaged reduced-order model [Druz2013; Druz2016]. Such a statistical averaged model would enable low-cost simulations in the overlimiting regime for process optimization [Mani2020]. Experimentally, a simple reduced-order parameter approach has been suggested based on fitting the overlimiting currents utilizing a Schmidt number [Stod2014]. However, this approach has not been further explored until today. Furthermore, Druzgalski et al. also found qualitative and quantitative differences in their 2D and 3D simulations, emphasizing the need for an new methodology quantifying the 3D hydrodynamics. The required fine resolution in space and time limited their simulations to small geometries and short time spans only. Therefore, the ability to extrapolate their conclusions to the length and time scales of practically relevant devices remains unclear until experimental results of the 3D velocity field are available.

To overcome this lack of experimental data relevant for industrial electrochemical devices with gap sizes below 1 mm, we developed and report an electrochemical cell allowing the optical recording of the 3D EC velocity field close to a cation-exchange membrane using micro particle tracking

velocimetry (µPTV). With this setup, one can now make the important step from 2D to 3D velocity field quantification: at practically relevant length and time scales over a range of overlimiting current densities. We use the velocity data to analyze the structural change of EC from vortex rolls to vortex rings in terms of vortex rotational direction. Additionally, we evaluate the velocity field statistics and the fluctuating velocity component. While our approach excludes the consideration of applied tangential flow, this proposed methodology allows to unravel details of EC hydrodynamics experimentally which in future can be compared to simulated velocity statistics when the reported length and time-scales will be accessible through high performance computing efforts.

3.3 Methods

The following paragraphs give only a brief summary of the used methods. A detailed introduction of all methods can be found in Chapter 2.

3.3.1 Experimental procedure

The experiments presented in this chapter are conducted in the experimental cell shown in Figure 2.1 that is suitable for electrochemical experiments and simultaneous recording of the evolving 3D velocity field using microparticle tracking velocimetry (µPTV) which is described in Sec. 2.2.

The electrolyte in the anode chamber of the cell is seeded with tracer particles as described in Sec. 2.3. During each experiment, a set multiple of the limiting current density is forced through the electrodes by regulating the potential. At current densities above the limiting current density, the movement of tracer particles induced by the velocity field of electroconvection is recorded.

At $4 \cdot i_{lim}$, the formation of the EC vortices takes longer than the electrostatic exclusion of tracer particles from the ESC, effectively preventing recording the EC vortex field. In this experiment, the current density is linearly decreased from $8.1 \cdot i_{lim}$ to the desired current density at a rate of

$4 \times 10^{-3}\,\mathrm{A\,m^{-2}\,s^{-1}}$. Afterward, a steady-state at $4 \cdot i_{lim}$ could be measured. This approach ensures the presence of particles close to the membrane due to previous EC mixing of the domain.

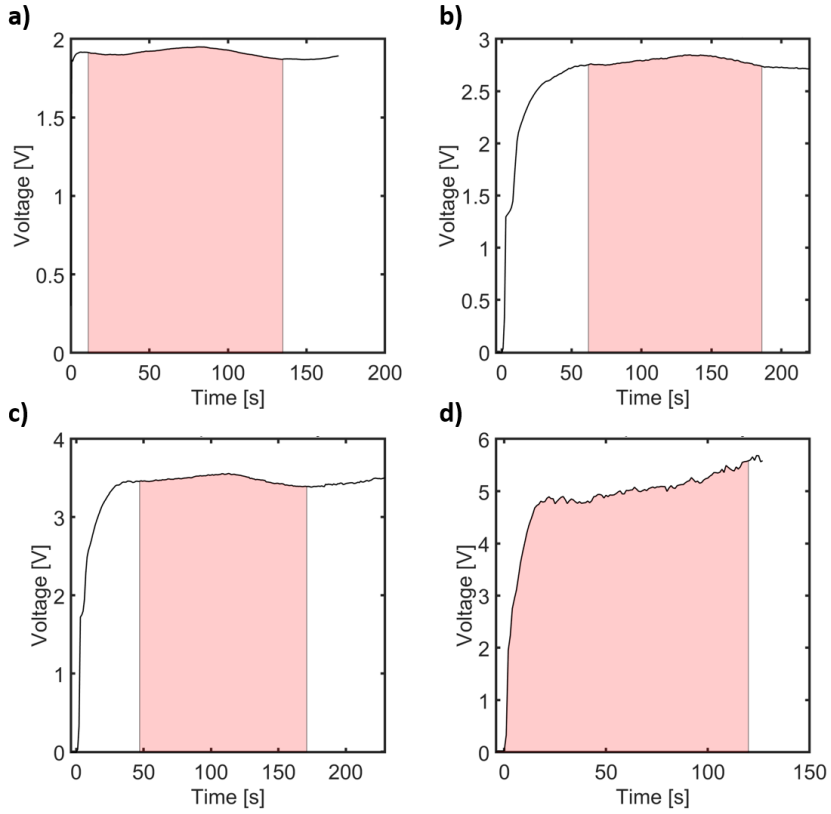

Figure 3.2: Chronopotentiometry graphs of the experiments. a) $4 \cdot i_{lim}$, b) $6.1 \cdot i_{lim}$, c) $8.1 \cdot i_{lim}$, and d) $10.8 \cdot i_{lim}$. The red area displays the recorded sections.

Figure 3.2 shows the chronopotentiometry graphs during the experiments at $4 \cdot i_{lim}$, $6.1 \cdot i_{lim}$, $8.1 \cdot i_{lim}$, and $10.8 \cdot i_{lim}$. The graph in Figure 3.2 a) directly starts at the steady-state potential due to the linearly decreased current density prior to the experiment as previously described.

At current densities of $6.1 \cdot i_{lim}$ and $8.1 \cdot i_{lim}$, the graphs (Figure 3.2 b) and d)) show a similar trend. After the calculated transition times of 3.94 s and 2.24 s, the systems resistance increases until EC reaches a steady state.

In the experiment at the highest current density of $10.8 \cdot i_{lim}$ (Figure 3.2 d)), the potential increases over the course of the measurement. This behavior indicates increasing resistance of the system due to chemical changes or gas bubble formation. Both phenomena could originate

from possible water dissociation at the membrane and the electrodes at this large potentials. The resulting $\mathrm{OH^-}$ ions possibly form solid CuO or $\mathrm{Cu(OH)_2}$ scaling at or inside the membrane [Chan2010]. In our experiments, we did not observe any visual changes of neither the membrane nor the electrodes. Excess $\mathrm{H^+}$ and $\mathrm{OH^-}$ would form $\mathrm{H_2}$ and $\mathrm{O_2}$ gas bubbles at the electrodes. However, gas bubble formation was only observed for experimental times larger than 500 s.

When a steady-state in the experiment was reached, the recording of the particle images is started. The flow is recorded for a maximum of 126 s at a frequency of 20 Hz. The time-resolved recording of the velocity field also enabled the reconstruction of the velocity field during the build-up of EC.

The 2D images are then post processed to reconstruct the 3D particle tracks and convert them into velocity fields as described in Sec. 2.4. The resulting velocity fields were then used to extract the statistics of the fluctuating velocity component according to Sec. 2.6.

3.3.2 Comparability to simulations

To achieve comparability to the 3D DNSs of Druzgalski et al. [Druz2016]. We chose process parameters (see Sec. 2.5) that best match their dimensionless numbers summarized in Table 3.1.

In this chapter, we plot our graphs with dimensionless values of time $t = \frac{t^*}{t_{diff}}$, velocity $u = \frac{u^*}{u_{diff}}$, and distance $l = \frac{l^*}{L_z}$ using the characteristic scales $t_{diff} = \frac{L_z^2}{D} \approx 748.54$ s and $u_{diff} = \frac{D}{L_z} \approx 1.07 \times 10^{-6}$ m s^{-1} with L_z = 800 µm and D = 0.855×10^{-9} m^2 s^{-1}.

Table 3.1: Dimensionless numbers. Comparison of dimensionless numbers of this study and the reference DNSs [Druz2016]. *The applied voltage in our experiments includes the voltage drop at the electrodes, in the membrane, and in the second electrolyte chamber.

Dimensionless number	DNS [Druz2016]	This study
Applied voltage	120 $\frac{V}{V_T}$	64 - 362 $\frac{V}{V_T}$*
Schmidt number	1×10^3	1.17×10^3
Electrohydrodynamic coupling constant	0.5	0.14
Dimensionless Debye length	1×10^{-3}	6×10^{-6}
Aspect ratio	6.3	10
i/i_{lim}	10	1.4 - 10.8

3.4 Results and discussion

Using the electrochemical chip, the movement of tracer particles between the membrane and anode can be followed. Particle tracking velocimetry reveals the 3D velocity field as a consequence of electroconvection at increasing current densities.

3.4.1 Evolution of the velocity field with increasing current density

First, I-V experiments identify the different current regimes in a current density over potential graph at multiples of the theoretical limiting current density ranging from $0 \cdot i_{lim}$ to $10.8 \cdot i_{lim}$, see Figure 3.3 **a)**. The plateau is clearly visible between potentials of about 0.4 V to 0.64 V matching the calculated theoretical limiting current density of 0.73 A m^{-2} (Eq. 2.5). At larger potentials, the system enters the overlimiting current region where EC vortices appear. Graphs of the chronopotentiometric experiments are shown in the Figure 3.2. The data points shown are time-averaged values of the fluctuating signals having their origin in the dynamic nature of the chaotic flow conditions close to the membrane surface.

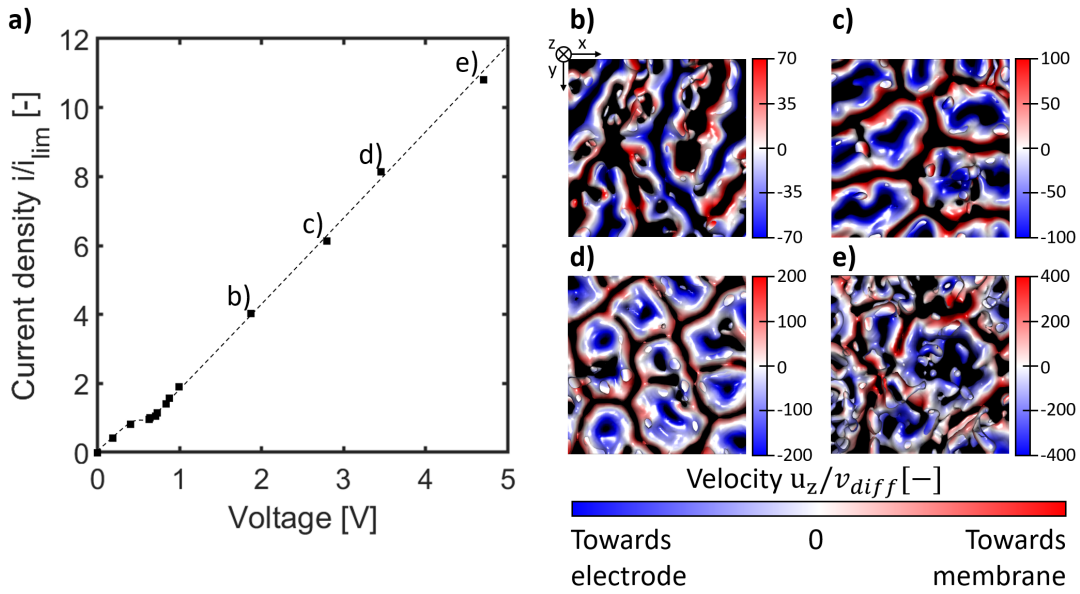

Figure 3.3: Development of electroconvection in the overlimiting regime. a) The graph shows mean voltages of chronopotentiometry experiments at increasing multiples of the limiting current. The dotted line is drawn for visual guidance. **b) - e)** Top views on isosurfaces of coherent vortex structures during experiments at **b)** 4 · i_{lim} (at 90 s), **c)** 6.1 · i_{lim} (at 70 s), **d)** 8.1 · i_{lim} (at 70 s), and **e)** 10.8 · i_{lim} (at 81 s) in the steady-state. The velocity is colored in magnitude and direction according to the scale bar from blue to red.

We record the velocity fields with our setup during experiments at different magnitudes of the overlimiting current. Figure 3.3 b)-e) show snap-shots of the top view on iso-surfaces of coherent vortex structures at 4 · i_{lim}, 6.1 · i_{lim}, 8.1 · i_{lim}, and 10.8 · i_{lim}, respectively. With increasing current density, the roll-like structure seen in Figure 3.3 b) collapses and vortex rings of oval shape emerge, see Figure 3.3 c). With even higher current densities, the vortex rings first become more regular, see Figure 3.3 d), before chaotic changing of patterns emerges, see Figure 3.3 e). While we show the quantification of such 3D velocity field for the first time, this transition from vortex rolls to vortex rings matches the qualitative observations of Demekhin et al. [Deme2014] and Kang et al. [Kang2020].

Additionally to the vortex structure, the measurement of velocity vectors enables the evaluation of rotational directions. At 4 · i_{lim}, pairs of counter-rotating vortex rolls are the dominant structure. Figure 3.3 b) shows that

the rolls of a pair connect in the vicinity of other vortex rolls. The velocity between two rolls of a pair is directed towards the membrane. Contrary, the velocity in the centers of vortex rings (Figure 3.3 c)-e)) is directed away from the membrane. This change in rotational direction indicates that vortex roll pairs do not simply split up in sections and recombine with themselves when transitioning to rings. Two other mechanisms seem more likely: First, vortex roll pairs could split up in sections and recombine but reverse their rotational direction. This change in direction could be induced by the emergence of a smaller vortex ring with a reversed rotational direction in the center of a recombined vortex roll. This smaller ring could increase in size and consume the recombined vortex ring resulting in a ring with a reversed rotational direction. Second, vortex roll pairs could split up at their contact points with other pairs and recombine at the contact point. This observation needs further investigation for a certain explanation.

Particle tracks of vortex rolls

Figure 3.4 shows the 3D reconstructed particle tracks at $4 \cdot i_{lim}$ which is in the region of vortex rolls. The vortex roll pairs, described in the previous section, are visible in the top view as pairs of particle tracks with opposing rotational directions. De Valenca et al. and Davidson et al. already reported that the slight Zeta potential of the tracer particles leads to their exclusion from locations with high anion concentration [Vale2015; Davi2016]. These locations appear as black areas which are void of particles. Another distinct observation is particles moving on separate orbits along each vortex roll, forming hollow cylindrical structures (Figure 3.4). The cross-section A-A shows that the particles are moving on exclusive trajectories. A possible explanation could be the formation of secondary vortices between these separate circles comparable to Taylor flow [Fane2009]. These vortices could exclude the particles from the rest of the roll. Another explanation could be the formation of regions of high ion concentration inside the vortex rolls. Such regions would also exclude tracer particles similar to the

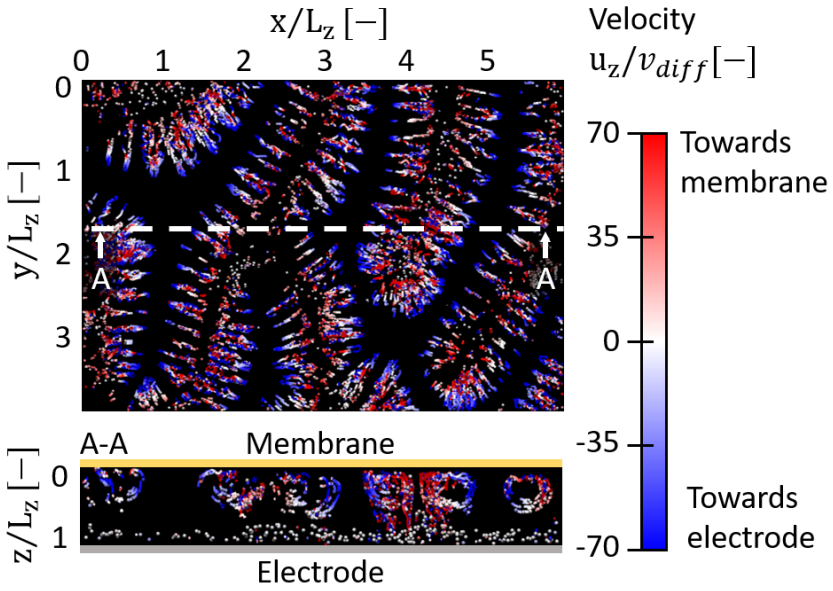

Figure 3.4: Snapshot of particle tracks for 4 · i_{lim} at 90 s. Top view of the particle tracks in the reconstructed 3D volume and a cross-section (A-A) with a track length of 49 time steps (2.45 s). A-A shows a 2D cross-section of the 3D particle field between the electrode and membrane. The velocity is colored in magnitude and direction according to the scale bar from blue to red. The axes are scaled by the channel height L_z = 800 µm. Black domains indicate regions where no tracer particles are present due to space charge exclusion as proven by [Davi2016].

reported phenomenon by De Valenca et al. and Davidson et al. [Vale2015; Davi2016]. To identify the validity of these hypotheses, quantitative information on the concentration field would be necessary.

Velocity field of chaotic vortex rings

Figure 3.5 shows a snapshot of the steady-state of EC in the regime of chaotic vortex rings at $10.8 \cdot i_{lim}$. The top view of reconstructed particle tracks in Figure 3.5 **a)** reveals the appearance of vortex rings with varying diameters. In the cross-section A-A, the particle tracks show circular movement at the borders of vortex rolls, for example, at $x/L_z = 4.5$. These circular tracks strongly resemble structures recorded in the 2D experiments of Valenca et al. [Vale2015].

For further investigation, the particle tracks are converted to a 3D velocity field. From this velocity field, coherent vortex structures are extracted and displayed as isosurfaces as shown in Figure 3.5 **b)**. The top view of the vortex field structure shows coherent vortex rings as reported by Demekhin et al. [Deme2014]. The largest displayed velocities seem to appear in the centers of small vortex rings and at contact points of multiple rings. To confirm this observation, cross-sections of the vortex field through such structures are displayed in Figure 3.5 **c)** B-B, C-C, and D-D. The analysis of the cross-sections prove that the largest absolute velocities in the respective planes appear close to the membrane and between coherent vortex rings. These velocities are up to 4.8 times larger than the average absolute velocities in their respective plane. This velocity distribution can be explained by continuity. The area with velocities towards the electrode is proportionally larger than the area with velocities towards the membrane (Figure 3.5 **b)**) which results in higher velocities for the latter.

These local velocity hot spots might be connected to local current density hot spots at the membrane. At the positions of high velocities towards the membrane, a larger quantity of high-concentrated electrolyte

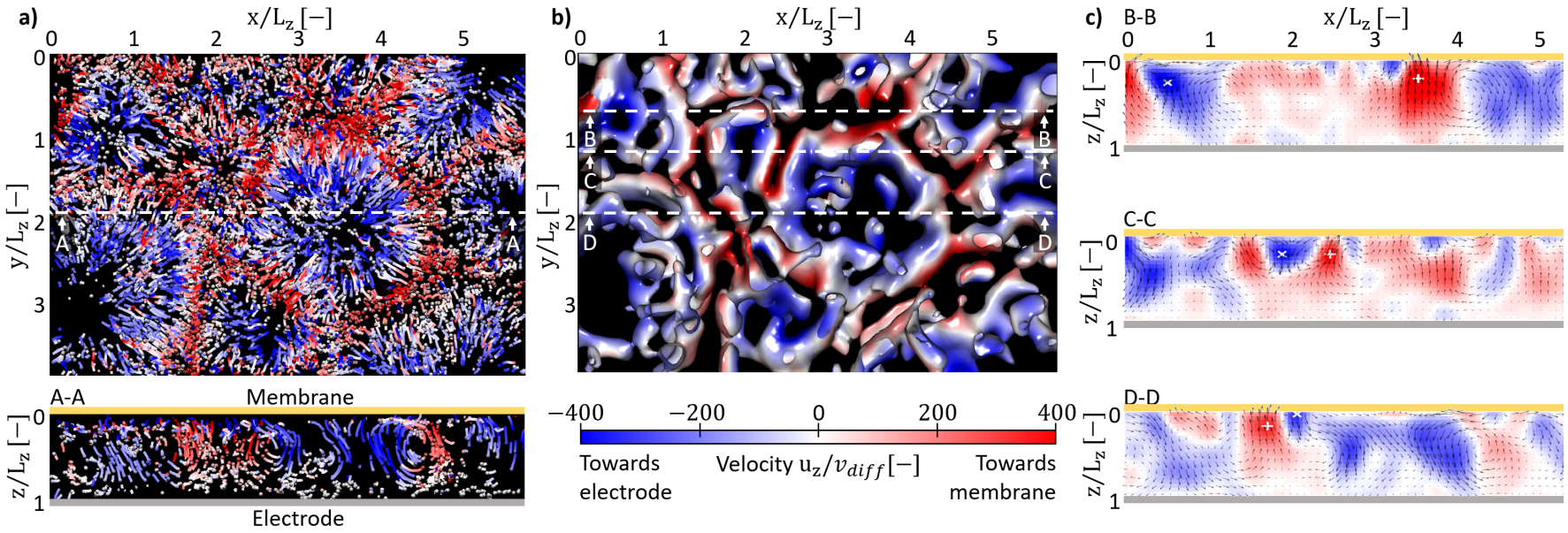

Figure 3.5: Snapshot of particle tracks and the corresponding velocity correlation for 10.8 · i_{lim} at 81 s. a) Top view of the particle tracks in the reconstructed 3D volume with a track length of 1 s . A-A shows a 2D cross-section of the 3D particle field between the electrode and membrane. b) Top view of the isosurface of coherent vortex structures in the reconstructed 3D volume showing a chaotic pattern of vortex rings at 81 s. c) Velocity maps of the cross-section B-B, C-C, and D-D. The white symbols mark the positions of the highest positive (plus) and negative (cross) velocities in each cross-section. The cross-sections A-A and D-D show velocity fields calculated from the particle tracks. Videos of the time-resolved particle tracks and vortex structure can be found as supporting information to the corresponding paper [Stoc2021b]. The velocity is colored in magnitude and direction according to the scale bar from blue to red.

solution is transported from the bulk to the cation-depleted membrane surface. The resulting local jump in cation concentration will, in turn, lead to a local jump in ionic current through the membrane. Thus, the numerically-predicted formation of current density hot spots [Druz2016] could be connected to the velocity hot-spot and verified by our experiments.

3.4.2 Velocity statistics of electroconvection

The spatio-temporal 3D velocity information allows to quantify the velocity statistics with increasing current density. This enables to compare the experimental statistics for chaotic vortex rolls to the velocity statistics simulated by Druzgalski et al. from 3D DNSs [Druz2016].

Comparison of velocity statistics to simulation

Figure 3.6 shows the velocity statistics calculated from our experiment with the statistics extracted from the simulations by Druzgalski et al. [Druz2016] for 3D DNSs. The statistical analysis quantifies (a) the mean square velocity and (b) the energy distribution across frequencies.

The mean square velocity for the 3D µPTV measurements and 3D simulation [Druz2016] are plotted over the normalized distance to the membrane z/L_z in Figure 3.6 **a)** and **b)**. The mean squares of the in-plane and out-of-plane velocity components show local maxima at about the same distances to the membrane of z/L_z = 0, 0.25, and 0.75 in the experiment and the simulation. A deviation is identified at the z/L_z = 0 and 1 positions that can be attributed to the ideal boundary conditions of the simulations compared to the experiments. The maxima positions originate from the vortex generation close to the membrane leading to the first maximum. The second maximum in the out-of-plane component marks half the vortex height with mostly velocity towards or away from the membrane. The last local maximum in the in-plane velocity is located at the average vortex height where the fluid turns its direction. However, the ratio between the amplitudes of both components differs between our measurements and the DNS.

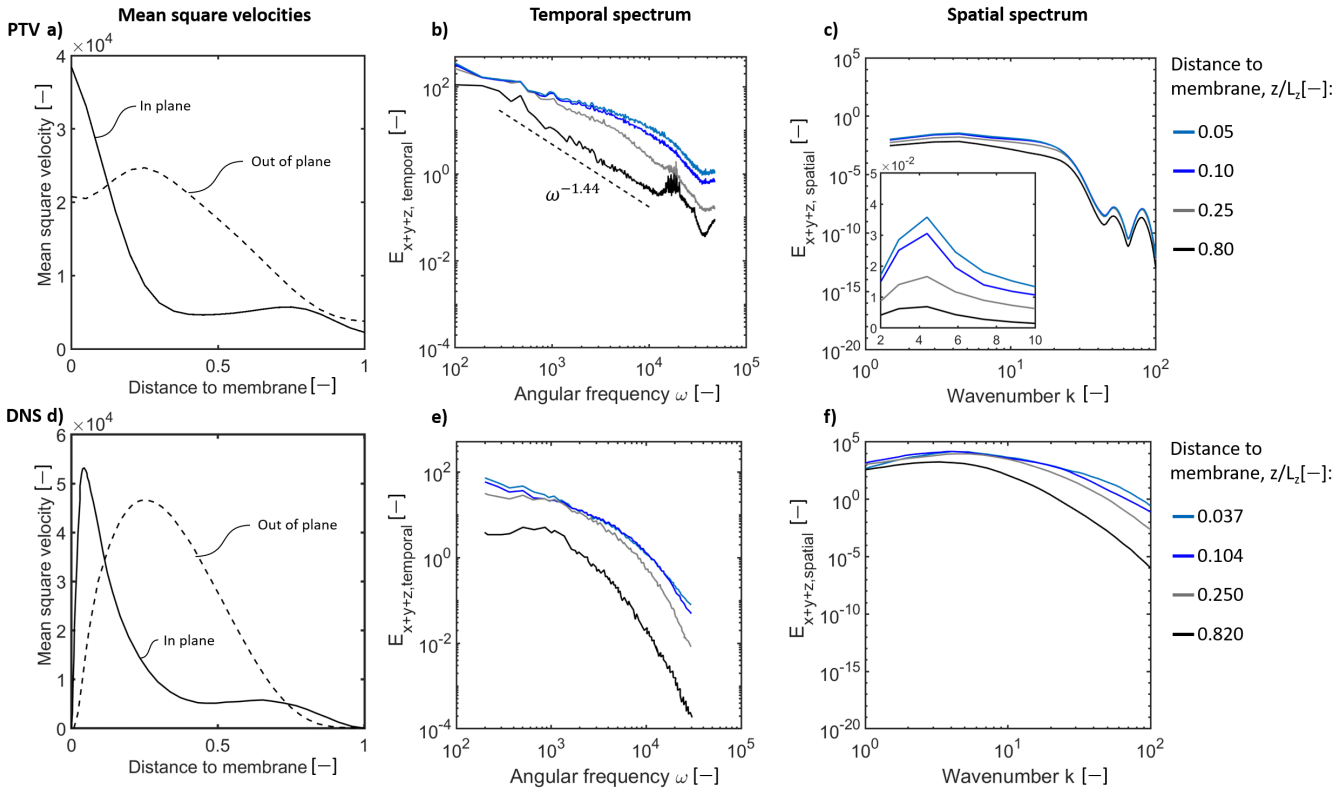

Figure 3.6: Comparison of mean square velocity, kinetic energy, and temporal and spatial energy spectra between 3D µPTV and the 3D DNSs [Druz2016]. The graphs present a direct comparison of our 3D µPTV results at 10.8 · i_{lim} (1000 time steps, 74.5 s to 124.5 s) a) - c) to the 3D DNSs results of Druzgalski et al. d) - f). Figures d) - f) reprinted with permission from C. Druzgalski and A. Mani, *Phys. Rev. Fluids*, 1, 1-21, 2016. [Druz2016] Copyright (2016) by the American Physical Society. a) and d) show the mean square of one in-plane and the out-of-plane velocity components over the dimensionless distance to the membrane z/L_z with $L_z = 0.8mm$. b) and e) show temporal energy spectra of the fluctuating velocity components. c) and f) show spatial energy spectra of the fluctuating velocity components. The spectra of 3D µPTV results b) and c) are plotted for dimensionless distance to the membrane of 0.05, 0.10, 0.25, and 0.80. The linear zoom of the spatial spectrum emphasizes the maxima at low wavenumbers. e) and f) are plotted for the normalized distances to the membrane of 0.037, 0.104, 0.250, and 0.820.

An explanation for the differences between our measurements and the DNSs of Druzgalski et al. can be the discrepancy in the electric double layer thickness by three orders of magnitude, see Tab. 3.1. The consequence of this difference is a decreased ESC region and, thus, the appearance of the maximum in-plane velocities closer to the membrane in the experiments [Druz2016]. Additionally, the velocities in z-direction are averaged in segments of 38.4 µm ($\sim 0.05 \cdot z/L_z$) height. This averaging always results in values above zero, even in the planes next to the membrane and electrode at which a no-slip boundary applies. Furthermore, the use of finite-sized tracer particles excludes volume close to the surfaces. Compared to DNSs, our experiments also include electrodes, the membrane, and a second electrolyte chamber, which influences the electrochemical cell's resistance and chemistry. This comparison proves that the velocity fields and its statistical mean features originating in the EC can be successfully extracted at practically relevant length and time scales.

The µPTV velocity field data is used to calculate the temporal spectra in planes parallel to the membrane, which indicate the dissipation of energy in the system, shown in Figure 3.6 **b)**. The energy graphs show similar trends in energy levels compared to the numerical results of Druzgalski et al. [Druz2016] in Fig 3.6 **e)**.

Close to the membrane (z/L_z = 0.05 and 0.10), the graphs' slope continuously decreases from small to large frequencies. At z/L_z = 0.25, a similar energy level is reached in the beginning but shows a more prominent decrease in slope afterwards. The temporal spectrum closest to the electrode notably start at similar energy levels. Different to the DNSs reference, the energy follows a linear decrease that can be fitted by a power-law of $E_{x+y+z,\,temporal} \sim \omega^{-1.44}$ between angular frequencies of $\omega = 2.8 \cdot 10^2$ and $\omega = 1.3 \cdot 10^4$. Between frequencies of $\omega = 1.3 \cdot 10^4$ and $\omega = 2.1 \cdot 10^4$, fluctuations appear followed by a decrease in energy. All graphs show a change in slope above an angular frequency of $\omega = 3.5 \cdot 10^4$.

The fluctuations and changes in slope most probably originate from

small-scale noise in the experiments and the measurement error of PTV at small scales [Herp2008].

The spectra for planes close to the membrane indicate the dissipation of kinetic energy across all frequencies without power-law dependencies, as also reported by Druzgalski et al. for all x,y-planes (Figure 3.6 **e)**) [Druz2016].

The power-law relation close to the electrode can be explained by the forces that evoke EC. The body force that generates EC vortices is located close to the membrane [Mani2020]. Therefore, vortices will propagate from the membrane towards the electrode. The shape of the spectra also indicates the generation of fluctuations of all time scales at the membrane. The fluctuations with small frequencies, e.g. large vortices, could propagate towards the electrode and dissipate their energy, whereas fluctuations with larger frequencies might not reach the regions close to the electrode.

The spatial energy spectra calculated from our experiment's velocity fields are displayed in Fig 3.6 **c)**. All graphs follow the same trend at different energy levels. They show a local maximum at a wavenumber of $k \sim 4.40$. The slope of the graphs decreases at k = 22 with two local maxima above k = 44. These local maxima at high frequencies in the spatial µPTV energy spectra can also be linked to small-scale noise and the measurement error of µPTV for small scales [Herp2008]. The spatial energy spectra reported by Druzgalski et al. [Druz2016] are reproduced in Fig 3.6 **f)**. Comparable to our experiment, all graphs show an increase in energy with a maximum at a wavenumber of $k \sim 4$ [Druz2016].

The peak at a wavenumber $k \sim 4.40$ in the experiment (Figure 3.6 **c)**) corresponds to a length of 1.43 times the electrode-to-membrane distance (L_z) carrying the largest energy. This length of $1.43 \cdot L_z$ matches well with literature and the diameter of the vortex rings in Figure 3.5 **b)**.

Due to the time-resolved recording of the velocity field, the evolution of the EC statistics over the whole experimental time are additionally analyzed in Section 3.4.3.

3.4.3 Development of velocity statistics with increasing current density

Figure 3.7 shows the mean square velocity, temporal and spatial energy spectra for the experiments at $4 \cdot i_{lim}$, $6.1 \cdot i_{lim}$, $8.1 \cdot i_{lim}$, and $10.8 \cdot i_{lim}$. All graphs have shapes typical for EC as also seen in Figure 3.6.

The overall mean square velocities increase with an increasing current density, as expected due to the higher energy input. The biggest difference appears between $8.1 \cdot i_{lim}$ and $10.8 \cdot i_{lim}$. Here, the sharp maximum in the out-of-plane velocity and the local maximum in the in-plane velocity seen at $8.1 \cdot i_{lim}$ broaden at $10.8 \cdot i_{lim}$. Additionally, the local maximum in the in-plane velocity shifts it's position from $\sim$0.5 L_z to $\sim$0.75 L_z. This behavior can be explained by the change from the distinct vortex ring pattern into a more chaotic pattern, described in Figure 3.3, with vortices that span the whole distance between membrane and electrode as seen in Figure 3.5.

The energy spectra in Figure 3.7 also reflect the overall higher velocities with increased energies for temporal and spatial fluctuations with increasing current densities. Again, the quality of the results at high frequencies in the temporal as well as the spatial energy spectra suffer from small-scale noise and the measurement error of PTV at small scales [Herp2008].

All temporal energy spectra in Figure 3.7 can be partly fitted by a power-law relation which was also seen in Figure 3.6 **c)**. The slope of the fitting first increases from $\omega^{-0.68}$ at $4 \cdot i_{lim}$ to $\omega^{-0.36}$ at $8.1 \cdot i_{lim}$ and then decreases to $\omega^{-1.39}$ at $10.8 \cdot i_{lim}$.

The graphs at $4 \cdot i_{lim}$ additionally show a region of constant energy between ω = 1 $\times 10^3$ and ω = 1 $\times 10^4$ which is less visible at higher current densities. The reason for this steady section could be the absence of information on velocities between the vortex rolls, as seen in Figure 3.4. The velocities in these regions potentially fluctuate in small length scales and at

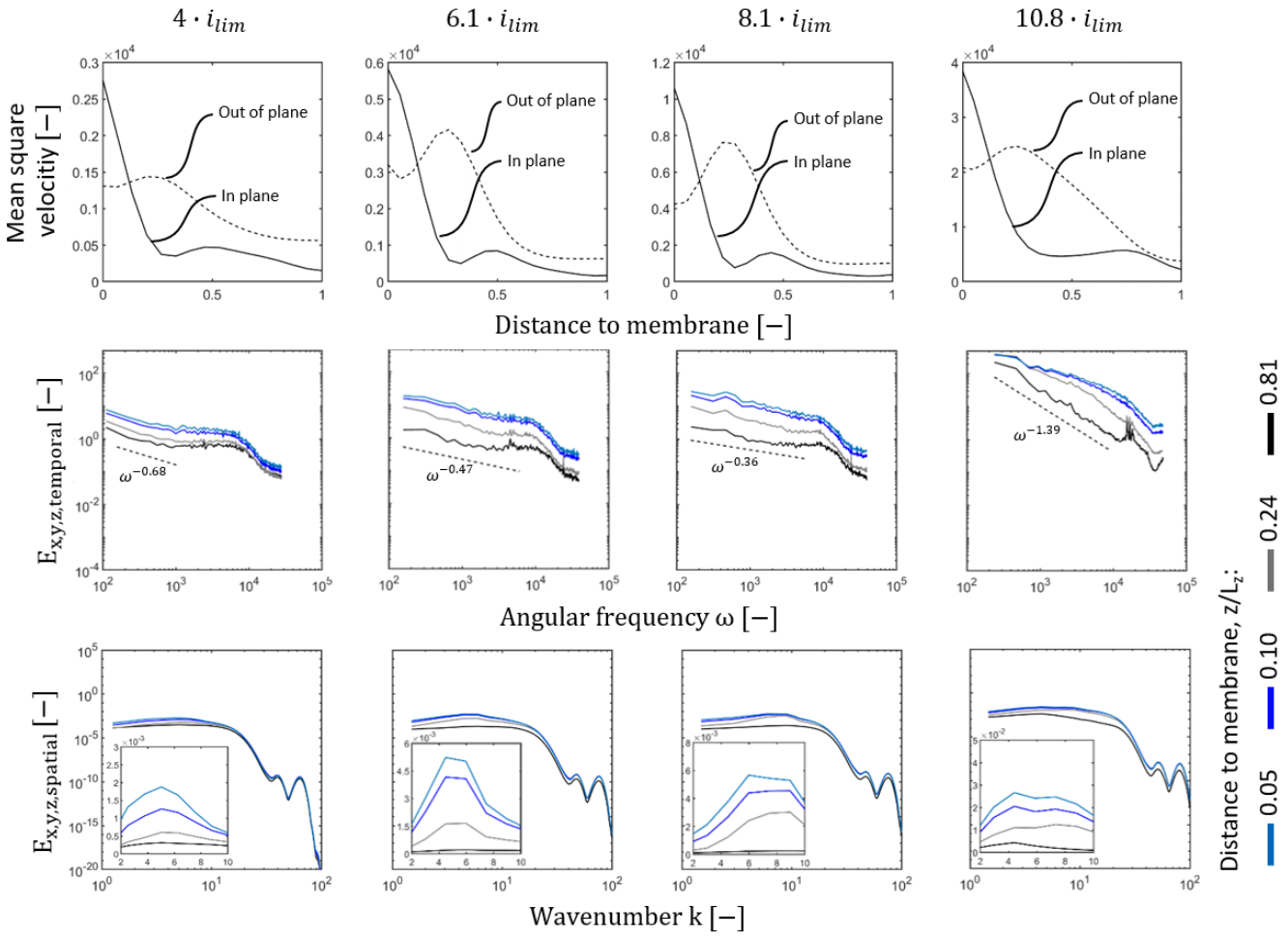

Figure 3.7: Development of the mean square velocity, temporal and spatial energy spectra in the overlimiting regime for 4 · i_{lim}, 6.1 · i_{lim}, 8.1 · i_{lim}, and 10.8 · i_{lim}. The graphs represent an average over 1000 time steps (74.5 s to 124.5 s). The first row shows the development of the mean square of one in-plane and the out-of-plane velocity components over the plane-to-membrane distance from 3D experiments. The second and third row show the development of the temporal and spatial energy spectra, respectively. Note the changing axes for the graphs showing the mean square velocities and the linear zoom on the maxima of the spatial energy spectra.

high frequencies.

The difference in the temporal energy graphs between $4 \cdot i_{lim}$ and $6.1 \cdot i_{lim}$ coincides with the structural transition from vortex rolls to vortex rings already seen in Figure 3.3. Moreover, the changes between the graphs at $8.1 \cdot i_{lim}$ and $10.8 \cdot i_{lim}$ match the transition from regular vortex rings to chaotic vortex rings shown in Figure 3.3.

In contrast, the shapes of the spatial spectra do not change significantly between current densities. However, the overall energy increases and the maxima emphasized in the linearly scaled inserts change positions from 5.02 k and 4.48 k to 8.95 k and finally to 4.40 k. These maxima positions reflect the changes in structure that were seen in Figure 3.3. The correlated diameter of the vortex structures first reduces from $6.1 \cdot i_{lim}$ to $8.1 \cdot i_{lim}$ and then increases again at $10.8 \cdot i_{lim}$. The linearly scaled insert at $10.8 \cdot i_{lim}$ shows a broader energy distribution over multiple wavenumbers compared to the graphs at lower current densities. The absence of a sharp maximum indicates that no single dominant length scale exists but a composition of different length scales. This composition is caused by the chaotic change in vortex structure at this large overlimiting current density with the fluctuating size of vortex rings.

Overall, our experiments confirm that large vortices are the dominant actors during EC [Druz2016]. The results additionally indicate that an increasing current density seems to have a more considerable impact on the mean square velocities and temporal spectra than on the spatial spectra.

Temporal Development of EC

Our set up also allows to analyze the development of the EC velocities, vortex structure, and statistics over time. Figure 3.8 and 3.9 show this development for the case of $10.8 \cdot i_{lim}$ in steps of 20 seconds for the first 120 s of the experiment.

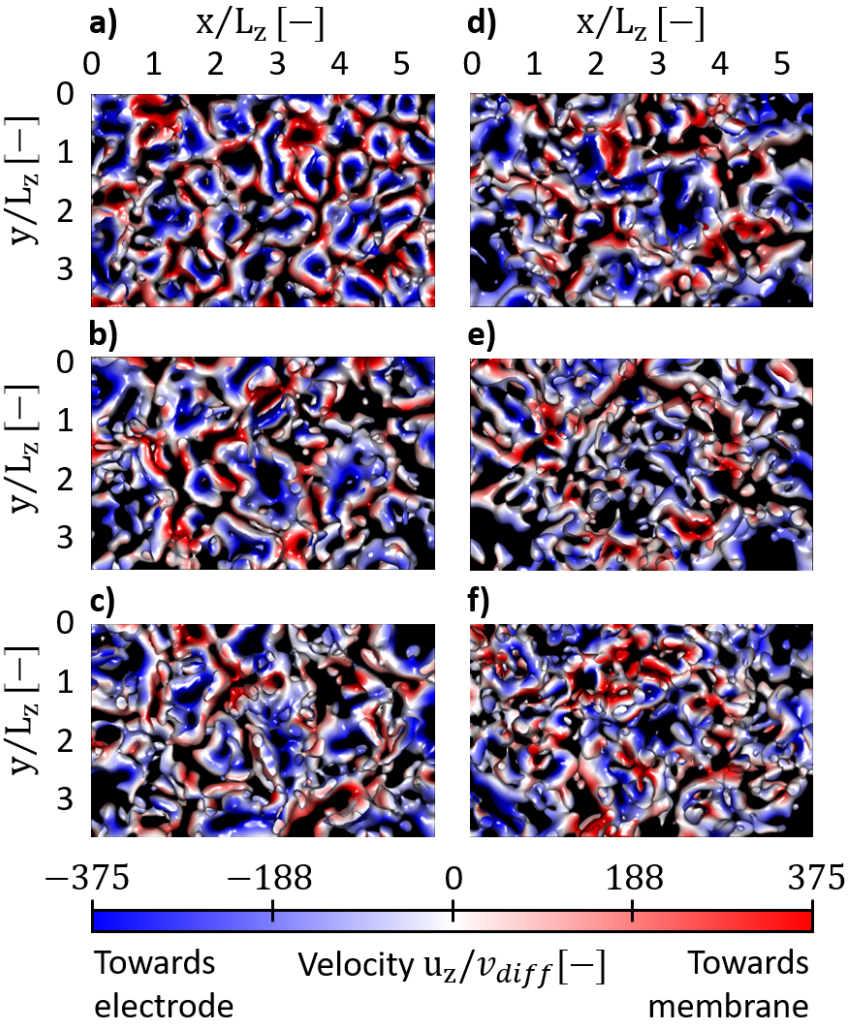

Figure 3.8: Temporal development of the EC vortex structure for 10.8 · i_{lim}. The top views of the structure of coherent vortices is depicted at **a)** 20 s, **b)** 40 s, **c)** 60 s, **d)** 80 s, **e)** 100 s, and **f)** 120 s of the experiment.

The development of the coherent vortex structures is depicted in Figure 3.8. The first coherent structures already build up at 20 s of the experiment appearing as mostly regular vortex rings. The structures grow in diameter over the course of 80 s while loosing their regular size and shape. Up to this stage, the velocity in most centers of coherent structures is directed towards the electrode. The velocity field becomes more chaotic between 100 s and 120 s. In this stage, coherent structures appear in a wide range of shapes and sizes with velocities directed both ways.

Figure 3.9 shows the change in one in-plane and the out-of-plane mean square velocities. The distinct velocity profile of EC is not completely build up in the first 20 s. Similar to later stages of EC, the maxima of both velocity components are close to the membrane. However, the out-of-plane velocity is higher than the in-plane component. Both velocity maxima first increase between 20 s to 40 s and decrease to a steady state value thereafter. At this point, the profiles are fully developed.

The above perceptions reflect in the development of the temporal and spatial spectra (Figure 3.9). As explained in the previous section, the local maxima at high frequencies in both the temporal as well as the spatial energy spectra and the following change in slope originate from small-scale noise and the measurement error of PTV for small scales [Herp2008]. Only slight changes are visible in the overall shapes of the spectra for both temporal and spatial analysis. However, some distinct observations can be made. First, the slope of the temporal spectrum for the plane closest to the electrode ($0.8 \cdot L_z$) changes between 0 s and 40 s from $\omega^{-0.79}$ to $\omega^{-1.35}$ indicating that the energy reaching the region closer to the electrode dissipates faster when EC is fulls developed. Second, the energy levels in both spectra increase from 0 s to 20 s and decrease again after 40 s as already seen in the mean square velocities. Third, the position of the maxima of the 2D spatial spectra change to smaller wavenumbers for all planes over time. The maxima positions shift from 11.6 k to 5.8 k between 0s and 100s as can be seen in the linear zoom of each spectrum. The shift of the maxima correlates to increasing contributions to the energy of vortex structures with larger length scales in the respective planes. The structures with the

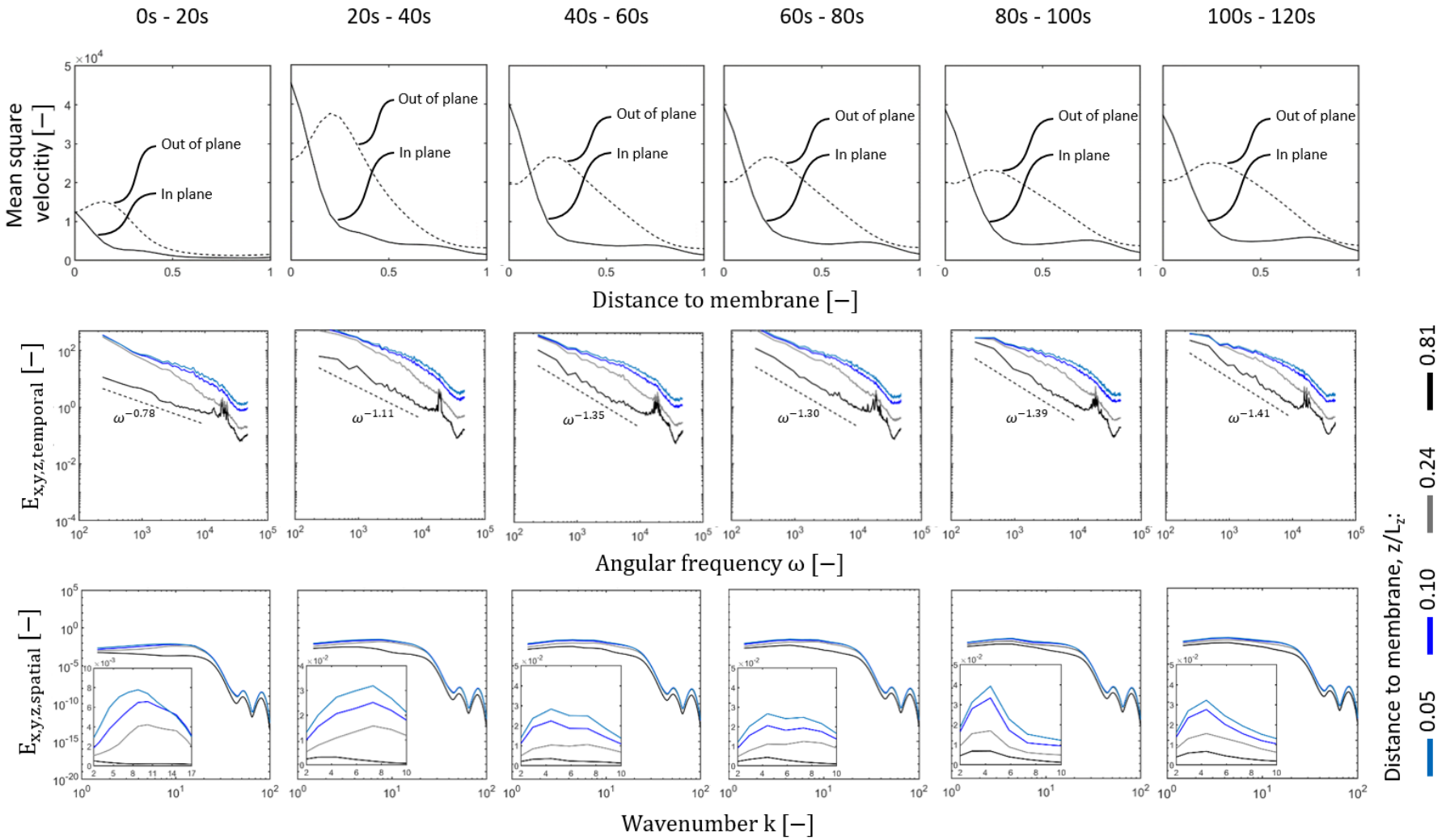

Figure 3.9: Temporal development of the mean square velocity, temporal and spatial energy spectra for 10.8 · i_{lim}. The first row shows the development of the mean square of one in-plane and the out-of-plane velocity components over the plane-to-membrane distance from 3D experiments between 0 s and 120 s. The second and third row show the development of the temporal and spatial energy spectra between 0 s and 120 s, respectively. Note the changing axes for the graphs showing the linear zoom on the maxima of the spatial energy spectra.

highest energy share grow from $0.61 \cdot L_z$ to $1.43 \cdot L_z$ over the course of 80 s. The negligible changes in all graphs confirm that the experiment was in a statistical steady state after about 40 s.

3.5 Conclusions

We established the first experimental setup for the time-resolved recording of the 3D velocity field during electroconvection (EC) close to a cation-exchange membrane. With this setup, Whe EC velocity field was recorded in the steady-state at multiples of the overlimiting current density covering length and time scales found in industrial applications inaccessible by current 3D direct numerical simulations (DNSs).

We visualized coherent vortex structures and revealed the change in vortex structure from vortex rolls to vortex rings along the iV-graph. This change in structure is coherent with the findings reported by Demekhin et al. and Kang et al. [Deme2014; Kang2020]. Additionally, our method enables evaluating the rotational direction of vortex structures. We found reversed rotational directions between vortex roll pairs and vortex rings, raising the question of the fluid mechanics during the transition from rolls to rings.

The particle tracks in the regime of vortex rings showed the movement of particles on separate orbits. However, possible explanations for this behavior need further physical evidence.

The velocity measurement in the regime of chaotic vortex rings revealed local velocity hot spots between the vortex rings directed towards the membrane. These possibly enable the transport of the cation-rich solution at the electrode towards the membrane. This phenomenon could explain the predicted current density hot spots by 3D DNSs [Druz2016].

Further statistical analysis of the velocity field disclosed the nature of energy transfer with a partial power-law behavior in the temporal spectrum. The spatial energy spectrum showed that the length scale carrying the largest energy is $1.43 \cdot L_z$. These findings showed good agreement of general trends with the reported statistics of Druzgalski et al. for 3D

DNSs [Druz2016]. Differences were found especially for high frequencies.

Lastly, the evolution of the vortex statistics for increasing limiting current densities was analyzed. The results reveal changes in the mean square velocities and the temporal energy spectra during the transition of EC from vortex rolls over vortex rings to chaotic behavior. The spatial energy spectra showed similar trends for all analyzed current densities. These findings indicated a more significant impact of EC's structural change on the temporal spectra than the spatial spectra.

All in all, the presented results provide a first insight of the fundamental physics of EC at practically relevant length and time scales. The experimental technique also builds a foundation to solve the remaining challenges in future detailed 3D studies. Especially the combination of experimental studies, that cover larger scales, and simulations, that more precisely resolve small scales, could lead to significant progress. Furthermore, the methodology permits studying the impact of membrane surface modifications on the hydrodynamics of EC. These modifications aim to manipulate the 3D vortex build-up and reduce the limiting current plateau with increasing success [Bals2007a; Davi2016; Vale2018b; Benn2018b]. Further investigation of the influence of a modified membrane surface on the vortex build-up is presented in Chapter 4. Additionally, knowledge of the velocity statistics enables the development of a RANS-like statistically averaged reduced-order model. Such a model will allow for feasibility analysis and optimization of electrically driven membrane processes in the overlimiting regime at a low computational cost. Full comprehension of EC will push the feasibility of desalination processes beyond the limiting current.

3.6 Appendix

3.6.1 Videos of particle tracks and vortex structure

Videos with a top view on the particle tracks corresponding to the snapshot in Figure 3.5 a) and of isosurfaces of coherent vortex structures corresponding to the snapshots in Figure 3.5 b) and Figure 3.8 of the experiment at $10.8 \cdot i_{lim}$ can be downloaded as supplementary material to the corresponding paper [Stoc2021b].

4

Electroconvection at charged patches

Parts of this chapter have been published as:
Florian Roghmans, Elizaveta Evdochenko, Felix Stockmeier, Sven Schneider, Amel Smailji, Rahul Tiwari, Annabel Mikosch, Elif Karatay, Alexander Kühne, Andreas Walther, Ali Mani, and Matthias Wessling, "2D Patterned Ion-Exchange Membranes Induce Electroconvection", *Advanced Material Interfaces*, 2019
DOI: 10.1002/admi.201801309

Parts of this chapter are submitted as:
Felix Stockmeier, Daniel Felder, Steffen Eser, Malte Habermann, Petar Perić, Stephan Musholt, Katharina Albert, John Linkhorst, and Matthias Wessling, "Localized Electroconvection at Ion-Exchange Membranes with Heterogeneous Surface Charge", *Under Review in Nature Materials*, 2021
Preprint available at Research Square as DOI: 10.21203/rs.3.rs-1093972/v1

4.1 Introduction

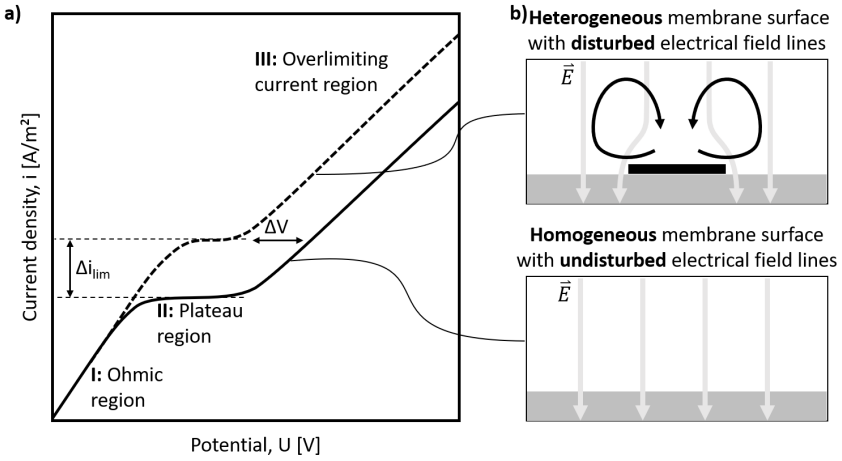

Figure 4.1: Current density over potential graph for a homogeneous and heterogeneous membrane and difference in electric field lines. a) Sketch of the current density over potential graph for an electrically driven membrane process with a homogeneous (solid line) or heterogeneous (dashed line) membrane. For both cases, three distinct regimes appear with a difference in the limiting current density i_{lim}. **b)** Electric field lines at a homogeneous and heterogeneous membrane surface.

The operation range of electrically driven membrane processes like electrodialysis (ED), capacitive deionization (CDI), and flow-capacitive deionization (FCDI) is limited by the fluid-sided resistance evolving during operation at high driving force [Mani2020]. In these processes, ions are transported through charge-selective membranes by an electric field. The ion flow, measured as a current density, increases linearly with increasing driving force in terms of an electric potential between two electrodes. However, the current increase is disrupted by a diffusion-limited plateau region (see Figure 4.1 **a)**) [Mani2020]. Today, it is known that a significant share of the current increase is due to a hydrodynamic instability called electroconvection (EC). EC overcomes the limiting current density due to the formation of convective 3D vortices, recently quantified by Stockmeier et al. [Stoc2021b], which mix the depleted layer close to the membrane. In fact, EC balances with unwanted water splitting and a maximum contribution of EC to the overlimiting current density is desired [Belo2006].

The possibility to evoke and intensify EC also at low driving forces has been the focus of multiple studies [Pham2012; Wess2014; Abdu2014; Davi2016; Vale2018a; Benn2018a; Gil2018; Rogh2019; Kim2021; Guan2021]. In general, the limiting current density and the length of the plateau region have been found to depend on the ion concentration, distance between the bulk electrolyte and membrane (i.e., the laminar boundary layer), and membrane characteristics like surface heterogeneity [Mani2020]. A heterogeneous membrane surface causes a disturbance of the electrical field lines close to the membrane, which, in turn, triggers EC, see Figure 4.1 **b)**. As a result, the plateau is shortened. The results of Roghmans et al. [Rogh2019] suggest that EC even emerges in the ohmic region at their pattern structure, increasing the limiting current density.

Modifying membranes as a means to control surface heterogeneity has gained increasing interest in the literature. Various studies focused on heterogeneity in surface geometry, conductivity, hydrophobicity, and zeta potential. It has been shown that these four parameters, in particular, have a significant influence on the formation of electroconvection and the rotational direction of the vortices. [Zabo1993; Mish1998; Choi2001; Volo2005; Bals2007a; Zabo2017; Neba2017; Mare2018; Pism2019; Rogh2019; Bell2022].

To elucidate the effect of a 2D geometrically heterogeneous surface, Valenca et al. recorded the velocity and orientation of EC vortices at a patterned cation-exchange membrane using 2D particle image velocimetry [Vale2018a]. The membrane was cast onto a linear gird, creating a surface topology with valleys and hills. Their recordings revealed the formation of pairs of counter-rotating vortices at the ridges of the pattern. The rotation of these vortices was directed towards the patterns' valleys, which resulted in the transport of ion-rich bulk solution towards the valleys. Overall, the 2D geometrically heterogeneous surface decreased the system's resistance of about 50%.

A similar observation was made by Davidson et al. in 2D DNSs at a membrane patterned with non-conductive sections [Davi2016]. Although these patterns did not alter the membrane's geometry, vortices formed at the pat-

tern's edges and rotated towards the patches' centers. This rotational direction results in the transport of ion-rich bulk solution towards the non-conductive patches. Even though the existence of patches increased the overall ion transport and strength of EC, one can imagine that membranes with similar EC-enhancing properties but either ion-conductive patches or a vortex field that transport ion-rich solution towards the free membrane surface will result in even more increased ion transport. They found that the optimal pattern length for a stable vortex structure and highest current density correlated with the diffusion boundary layer's height.

Kim et al. ranked the current increase of different, spacer-like structures on top of the membrane surface under forced flow [Kim2021]. They found that segmentation of the boundary layer and, therefore, creating intentional dead zones is beneficial for the build-up of EC. Square patterns, forming large dead zones, resulted in the highest vortex intensity in the overlimiting regime.

Recently, we presented a method to simultaneously engineer the surface geometry, conductivity, and charge of membrane surfaces in a controlled manner [Rogh2019]. An ink-jet printing technique was used to apply a pattern of circular patches of polymer microgels with varying zeta potential. Such modified membranes were found to double the limiting current density with a 40% reduced plateau length and only slightly increased membrane resistance. The hypothesis behind this successful modification was a combination of an early start of EC even at limiting current densities, the ion conductivity of the pattern, an altered rotational direction due to the direction of the surface charge gradient, and the formation of a 3D vortex pattern compared to the 2D structures of Valenca et al. and Davidson et al. Valenca et al. [Vale2018a] and Davidson, Wessling, and Mani [Davi2016].

The examples mentioned above show the vast potential that engineered ion-exchange membranes with tailored surface properties possess to increase the efficiency of electrically driven membrane processes. However, the physics behind the current density increase, especially of Roghmans

et al.'s multi-influential microgel patterns, are still unclear. Therefore, the EC vortex field structure at such patterns needs to be analyzed, isolating important properties for future membrane modifications.

In this paper, we evaluate the effect of patterning a cation-exchange membrane surface, with the technique described by Roghmans et al., on the 3D hydrodynamics of EC using micro particle tracking velocimetry (µPTV) [Rogh2019; Stoc2021b]. Our numerical and experimental investigation aims at revealing the effect of patterning the membrane surface on the electroconvective vortex field. First, we analyze the orientation of coherent vortex structures and their rotational direction in 2D direct numerical simulations (DNSs) and confirm these results by recording the 3D velocity field during its build-up close to a modified membrane with µPTV. We then affirm that a change in the vortex structure compared to an unmodified membrane also persists in the steady-state of our experiments. At last, we conclude the potential of the findings by exploring the possibility of fully controlling and shaping EC's vortex field with our modification method.

4.2 Model problem

We use the open-source, OpenFOAM-based, finite-volume solver rheoTool by Pimenta and Alves to simulate the electroconvective flow driven by an electric field of a symmetric binary electrolyte between an ideal cation-exchange membrane and a reservoir, see Figure 4.2 [Pime2018]. The solver couples transport of charged species described by the Poisson-Nernst-Planck equations with the Navier-Stokes equations for fluid flow by viscous drag. In this investigation, we extend rheoTool's 'Charge transport across an ion-selective membrane' case, which is based on the work of Druzgalski et al. [Druz2013].

Figure 4.2 shows the 2D rectangular domain, which has an aspect ratio of 6 lengths per height with periodic boundary conditions at each end. The ion transport is driven by the external applied potential difference $\triangle V$ between reservoir and membrane. The reservoir boundary condition is im-

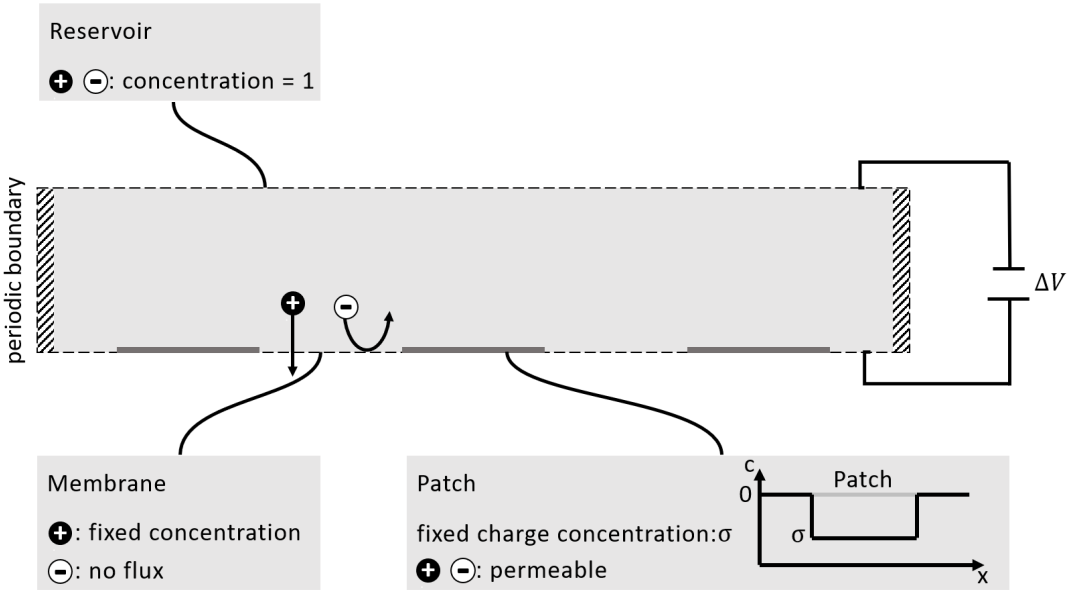

Figure 4.2: Domain and boundary conditions of the direct numerical simulations. The domain is rectangular shaped between a mixed reservoir, an ideal cation-exchange membrane, and two periodic boundaries.

plemented as an electro-neutral electrolyte with fixed concentrations. The boundary condition for the ideal cation-exchange membrane has a fixed cation concentration and is impermeable for anions. We add a pattern of patches that introduce additional charge through the location-dependent background charge σ to the membrane surface. The patches are fully ion-permeable, and the complete flow equations are solved inside of them. The length of the patches, as well as their distance to each other, is chosen equal to the domain height, which was shown to evoke an optimal vortex structure when using non-permeable patches [Davi2016]. We implement the patches with an aspect ratio of 100, similar to our previous study [Rogh2019].

4.2.1 Governing equations

The simulation is based on the governing equations described in Chapter 2. Additionally, we extend the electric model and define the charge density as

$$\rho_{E,P} = F(\sum_{i=1}^{m} z_i c_i + \sigma) \tag{4.1}$$

where F represents Faraday's constant and m is the number of different ionic species. Additionally, σ is the background fixed charge introduced by the patches. In the rest of the domain, σ is set to zero.

4.2.2 Computational methods

The above equations are solved on a 2-dimensional mesh with 480 uniformly distributed cells in the x-direction, and 90 cells in the y-direction stretched with a scaling factor of 1.042. This setup achieves a minimum cell height of 0.001 H at the membrane and ensures a sufficient resolution. Furthermore, compared to the study of Druzgalski et al. [Druz2013], we increased the temporal resolution to time steps of $1 \cdot 10^{-7}$ s to ensure convergence when introducing patches.

Table 4.1: Dimensionless simulation parameters.

Parameter	Description	Value
$\Delta\Phi$	Applied voltage	5, 20, 30, 60, 120
σ	Patch charge	-0.5 to 0.5
λ_d	Dimensionless Debye length	10^{-3}
κ	Electrohydrodynamic coupling constant	0.5
Sc	Schmidt number	1000
$c^{\pm}_{res}$	Reservoir ion concentration	1
c^{+}_{mem}	Cation concentration on membrane surface	2

The selected parameters (see Table 4.3 in the supporting information) correspond to dimensionless values typical for the direct numerical simulation of EC, see Table 4.1 [Druz2013; Kara2015; Davi2016]. The applied potential was set to $\Phi = 20 \cdot V_t$ with the thermal voltage $V_t = \frac{k_B T}{ze}$ which is equivalent to a potential difference at which almost no velocity is induced at a homogeneous membrane. The electrohydrodynamic coupling constant $\kappa = \frac{\varepsilon}{\mu D} \cdot (\frac{k_B T}{ze})^2$ and Schmidt number $Sc = \frac{\mu}{\rho D}$ are fixed by choice of solution and absolute temperature. The chosen values are typical for aqueous solutions at 300 K. The dimensionless Debye length $\lambda_d = \sqrt{\frac{\varepsilon k_B T}{2 c_b (z e L_z)^2}}$ is mostly dependent on the size of the examined system and electrolyte concentration. For example, a value of $\lambda_d = 10^{-3}$ corresponds to a reservoir to membrane distance of H = 1 $\times$ 10^{-5} m using a 1 mM electrolyte. This value is commonly chosen in numerical examinations of EC, resulting in a small system size with reasonable computational cost while providing physically relevant results [Druz2013; Davi2016]. Experimental investigations have larger system sizes in the order of millimeters with electrolyte concentrations of 1 mM and above [Vale2015; Rogh2019; Kang2020].

We plot our graphs with dimensionless values of time $t = \frac{t^*}{t_{diff}}$, velocity $u = \frac{u^*}{u_{diff}}$, concentration $c_i = \frac{c_i^*}{c_{bulk}}$, and distance $l = \frac{l^*}{H}$ using the characteristic scales $t_{diff} = \frac{H^2}{D} = 0.1$ s and $u_{diff} = \frac{D}{H} = 1 \times 10^{-4}$ m s^{-1}.

4.3 Experimental details

We conduct experiments using the previously described electrochemical cell that is suitable to evoke simultaneously and optically record electroconvective vortices, see Chapter 2 Figure 2.1. We record and analyze the difference in vortex fields evolving at different modified cation-exchange membranes in this cell. The following sections point out differences in the electrochemical experiments and velocity recording to the description in Chapter 2. Additionally, the method of membrane modification is described.

4.3.1 Velocity measurement

We use an optical technique called micro particle tracking velocimetry (µPTV) to reconstruct the 3D flow field of EC during operation which is described in detail in Section 2.2. The operation of the µPTV setup and the processing of the recorded images is done in the software DaVis, which is also used for data post-processing, velocity reconstruction, and plotting of coherent vortex structures, see Section 2.4.

4.3.2 Experiments with velocity reconstruction

During each experiment, a set multiple of the limiting current density is forced through the electrodes by regulating the potential in chronopotentiometric experiments with a potentiostat (Interface 1010E, Gamry, Pennsylvania, USA). The electrolyte is not pumped during the experiments, and the observed movement only results from EC vortices. When the electrochemical experiments start, we record the build-up of the EC vortex field at $4 \cdot i_{lim}$ for a maximum of 126 s at a frequency of 20 Hz.

After the experiments, we color the membrane inside the module with a diluted fluorescent dye (Staedler, Lumocolor, Germany) to visualize the otherwise transparent patches' positions.

4.3.3 Velocity statistics

We calculate velocity statistics according to Section 2.6 which are plotted as dimensionless numbers as described in Section 2.5.

4.3.4 Membrane surface modification

The modified Nafion membranes are produced by ink-jet printing of microgel suspensions using an Autodrop Compact 2.21 ink-jet printer with an MD-K-140 print head (microdrop Technologies, Germany) as described by Roghmans et al. [Rogh2019].

Table 4.2: Microgel types used for membrane modification. In contrast to the microgels' zeta potential, Nafion has a reported zeta potential of -80 mV [Barb2014].

Microgel type	Synthesis	Zeta potential	Cross-linking degree	Reference
PNIPAM-co-Aac (11.5 wt% Aac)	surfactant free emulsion polymerization	-9.5 mV	1:25	Burmistrova et al. [Burm2011]
P2VP	surfactant free emulsion polymerization	+45.3 mV	1:100	Roghmans et al. [Rogh2016]

The ink is prepared by diluting suspensions of either PNIPAM-co-Aac or P2VP microgels, see Tab. 4.2 to a concentration of 0.05 wt% with HPLC grade water. We produce patterns of circular patches with either 400 µm or 600 µm diameter and a spacing of 450 µm or 900 µm, respectively.

Nafion membranes have a reported zeta potential of -80 mV [Barb2014]. The used microgels are expected to change the surface charge towards positive zeta potentials with -9.5 mV for PNIPAM-co-Aac and +45.3 mV for P2VP measured with a Malvern Zetasizer Nano ZS (Malvern Panalytical Ltd).

4.4 Results and discussion

Our numerical and experimental investigations aimed at revealing the effect of patterning the membrane surface on the electroconvective vortex field. First, we analyze the orientation of coherent vortex structures and their rotational direction in 2D DNSs and confirm these results by recording the velocity field during its build-up close to a modified membrane with µPTV. Second, we affirm a change also in the steady-state vortex structure during experiments. Third, we explore the possibility to fully control and shape the vortex field of EC with our modification method.

4.4.1 Vortex orientation and rotational direction at heterogeneous surface charge - simulation

We performed 2D simulations in a rectangular domain with an aspect ratio of 6 described in detail in the Methods section. The simulations assume a potential difference between the top reservoir and the ideal bottom cation-exchange membrane.

Figure 4.3 **a)** displays the steady-state current densities over the potential for simulations with patches of 10 % reduced or increased charge ($\sigma = -0.1$ and $\sigma = 0.1$) and the case with homogeneous surface charge ($\sigma = 0$). In all three cases, the plateau starts at a potential of 5 V_t with a limiting current density of 20 A m^{-1}. For the case with homogeneous surface charge ($\sigma = 0$), the plateau region extends to 22.5 V_t, transitioning in the overlimiting current density at 25 V_t with a linearly increasing current density thereafter.

The simulations with patches both show a shortened plateau region that ends at 15 V_t. The overlimiting current region starts at 17.5 V_t. However, the graphs do not steadily increase. Instead, both exhibit a local minimum at 30 V_t again overlapping with the patch-less case graph showing a similar increase from thereon. This behavior indicates that the patches' influence dwindles with increasing potential. The experimental study of Roghmans et al. [Rogh2019] showed a more pronounced effect even in the overlimiting region, indicating that our simulation does not consider all relevant effects. Still, these results provide valuable insights into the physics at play.

Figure 4.3 **b)** shows a zoom on the transition through all three regions. The zoom reveals that the current densities of the simulation with negative patch charge reach up to 8.4% higher values at the beginning of the overlimiting current region compared to the positive charge case. This difference possibly results from the 15.6% higher root mean square velocity in the first case, which might, in turn, originate from the membrane's higher net charge as EC depends on the concentration gradient close to the membraneμ [Mani2020].

The images in Figure 4.3 **c)** show the steady-state of simulations at 20 V_t

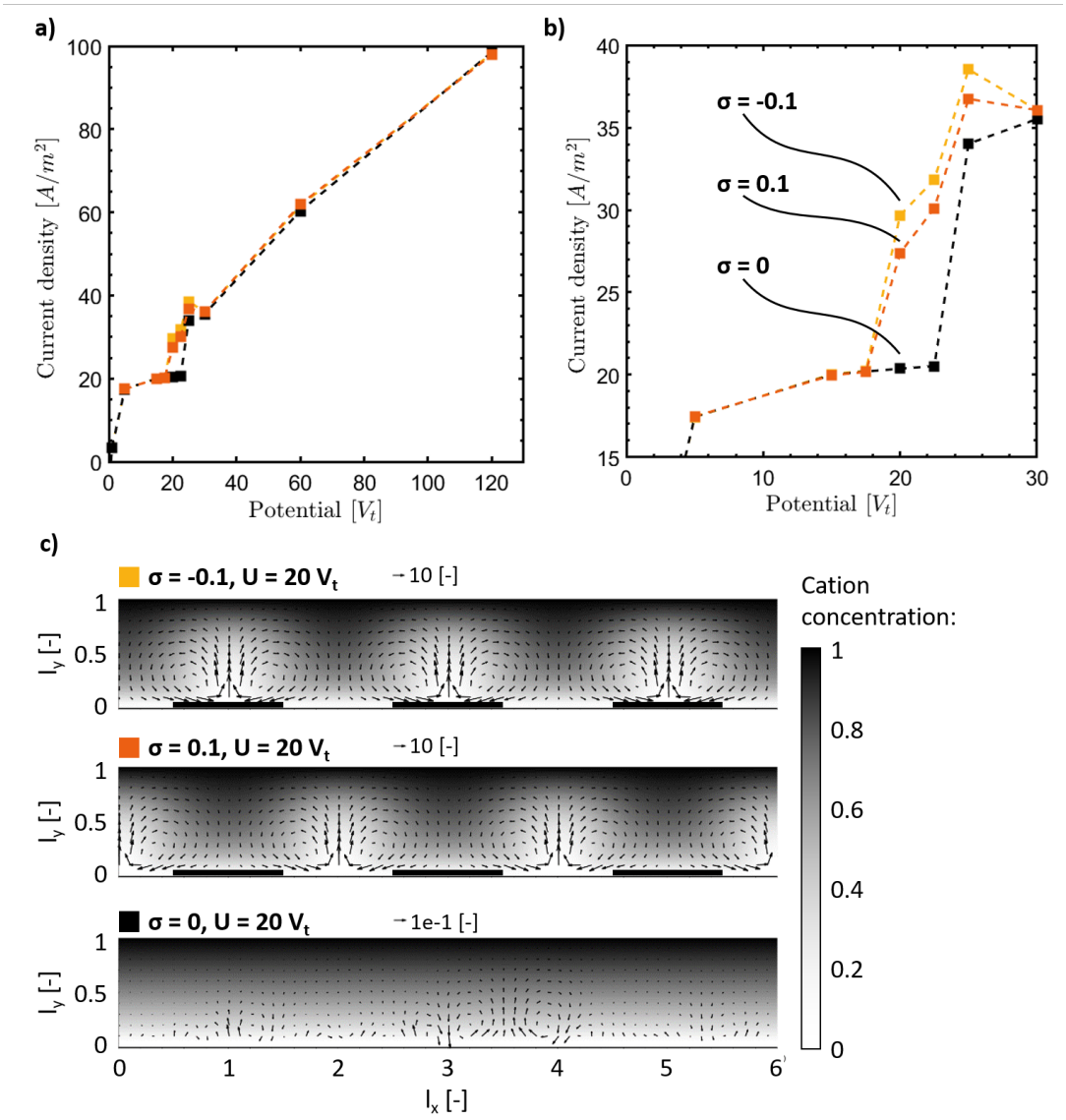

Figure 4.3: Simulation results for current densities, vortex structure, and rotational direction. a) shows the current density over potential plot for an untreated membrane, two patched membrane one with positive and one with negative zeta potential. **b)** shows an enlarged graph of the plateau region seen in **a)**. **c)** displays the corresponding cation concentration field as gray-scale background and the velocity field as an arrow plot for simulations at 20 V_t (thermal volts).

for all three cases. The gray-scale background indicates the cation concentration, and the overlaid arrows show the velocity field.

At the membrane with homogeneous surface charge ($\sigma = 0$), the cation concentration gradient between bulk and membrane stays constant over the channel's width. As a result, emerging velocities are small with little vorticity and maximum velocities in the order of $1 \cdot 10^{-5}$.

For patched membranes, convection cells of low concentration emerge as light gray areas that span from the membrane to close to the bulk phase. Inside the convection cells, velocities are larger than two orders of magnitude than for a homogeneous membrane and are directed towards the bulk. Between the cells, the velocities are directed towards the membrane. This way, vortex pairs form inside the cells. In both simulations ($\sigma = -0.1$ and $\sigma = 0.1$) the convection cells locate above the regions with more negative surface charge.

These results indicate that the patches lead to early and strong EC development even at potentials where the homogeneous membrane shows limiting current densities. In addition to the early EC occurrence, the regular patch pattern leads to the EC vortex field's orientation alongside that pattern. In combination with the relative surface charge change, this orientation dictates the positions of the low concentration cells and, therefore, the rotational direction of the EC vortices above the patches. The resulting current densities predict that the rotation of vortices toward the bare membrane between patches in the negative charge case is favorable. To validate the findings of the 2D simulations, namely the change in rotational direction and localization of vortex field features, 3D experiments were conducted with membranes modified with patches of defined surface charge contrast to the base material.

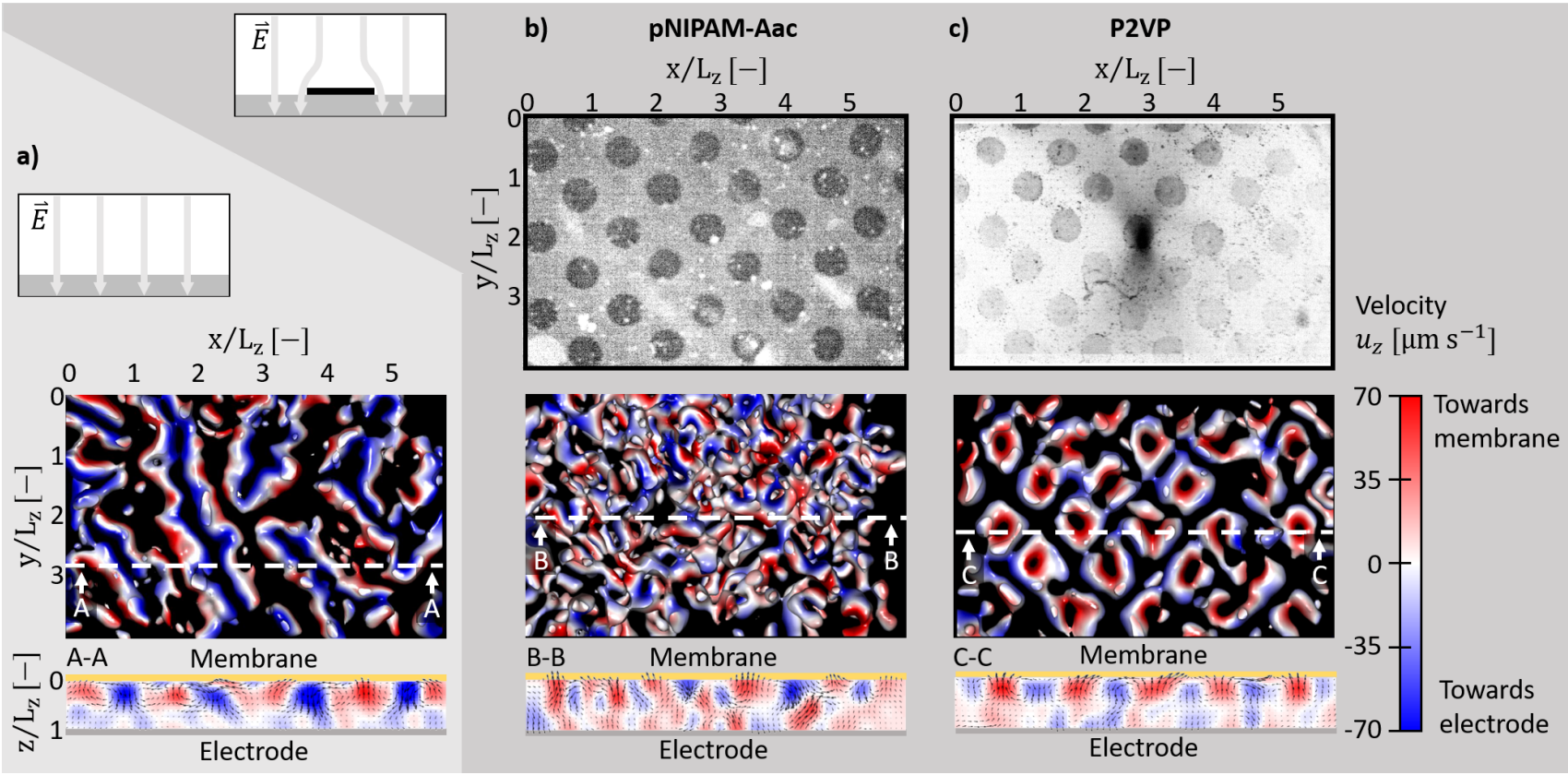

Figure 4.4: Vortex structure and rotational direction during electroconvection. **a)** Top view on the steady-state vortex structure and cross-section of the velocity field developing at a bare membrane. **b)** & **c)** Patch patterns, vortex structures, and velocity fields for membranes modified with pNIPAM-co-Aac an P2VP microgels, respectively. The velocity is colored in magnitude and direction according to the scale bar from blue to red.

4.4.2 Vortex orientation and rotational direction at heterogeneous surface charge - experiment

Figure 4.4 **a)** shows a top view on the 3D velocity field measured at $4 \cdot i_{\text{lim}}$ between the anode and an untreated membrane. The velocities are plotted in a symmetric red, white, and blue spectrum on iso-surfaces of coherent vortex structures.

The experiment shows a typical, stable vortex roll pattern for relatively small overlimiting current densities visible as linearly stretched coherent vortex structures [Deme2014; Kang2020; Stoc2021b]. These rolls occur as counter-rotating pairs visible as tube-like coherent structures. At spots where multiple roll pairs would collide, the parallel rolls of a pair connect to form a half-circle. The velocity between clearly visible vortex roll pairs is directed towards the electrode indicated by the blue coloring.

The top picture of Figure 4.4 **b)** displays the PNIPAM-co-Aac microgel pattern structure with a patch diameter of 400 µm. Despite the patch pattern, no regular structure is visible in the vortex field. However, the structure also differs from the case of an untreated membrane. Instead of vortex rolls, single ring-shaped vortices can be found with velocities in their centers directed towards the membrane.

The P2VP microgel patch pattern in Figure 4.4 **c)** is similar to the pattern produced with PNIPAM-co-Aac microgels. Nevertheless, the vortex structure differs to a large degree forming a regular pattern of vortex rings. The vortex ring positions match the patch pattern structure in position and size. Furthermore, this experiment proves validates the simulations in Figure 4.3 with the velocities in the centers of rings being directed towards the patches.

The observed transition in Figure 4.4 from a regular vortex roll pattern **a)** to an unorganized vortex field **b)**, and an ordered structure **c)** with the introduction of increasing surface charge differences between membrane and pattern shows that a minimum charge difference is necessary to trig-

ger ordered pattern formation. This dependence is supported by additional simulations presented in the supplementary material S2. The zeta potential difference between the Nafion membrane and the PNIPAM-co-Aac patches is not large enough to enforce vortex orientation. However, the introduced heterogeneity is still sufficient to disturb the usual regular vortex roll pattern seen at an untreated membrane. The P2VP microgel pattern introduces a strong zeta potential contrast towards Nafion, which enforces vortex orientation as predicted by the simulations. The results show a clear and stable vortex formation along the pattern perimeters.

4.4.3 A change in the steady-state is achieved

Figure 4.5 shows a series of snapshots over time of the build-up of EC towards a steady-state for a P2VP microgel treated membrane. The first time step (12.5 s) shows only a small amount of coherent structures without particular order. At 25 s, an ordered structure of vortex rings is clearly visible, as already described in the previous section (see Figure 4.4 **c)**). The velocity in the centers of vortex rings is directed towards the patches on the membrane. The structure is preserved at 37.5 s, but the overall velocities are increased. The next snapshot (50 s) shows a different vortex field. The regular structure vanished, showing vortex rings or ellipses of different shapes instead. Additionally, the rotational direction in the vortex ring centers changes towards the electrode, similar to the direction of EC vortex rolls at an untreated Nafion membrane at higher current densities [Stoc2021b]. Later, the chaotic vortex rings approximately double in diameter between 50 s and 62.5 s, which stays constant in the steady-state at 112.5 s. The changed rotational direction is dominant throughout the steady-state. Compared to the case of an untreated Nafion membrane in Figure 4.4 **a)**, no vortex roll pattern forms.

The loss of orientation occurs for two reasons. First, the current density of $4 \cdot i_{\mathrm{lim}}$ might already be too large to sustain the orientation. The simulations in supplementary materials S2 show that the electrokinetic

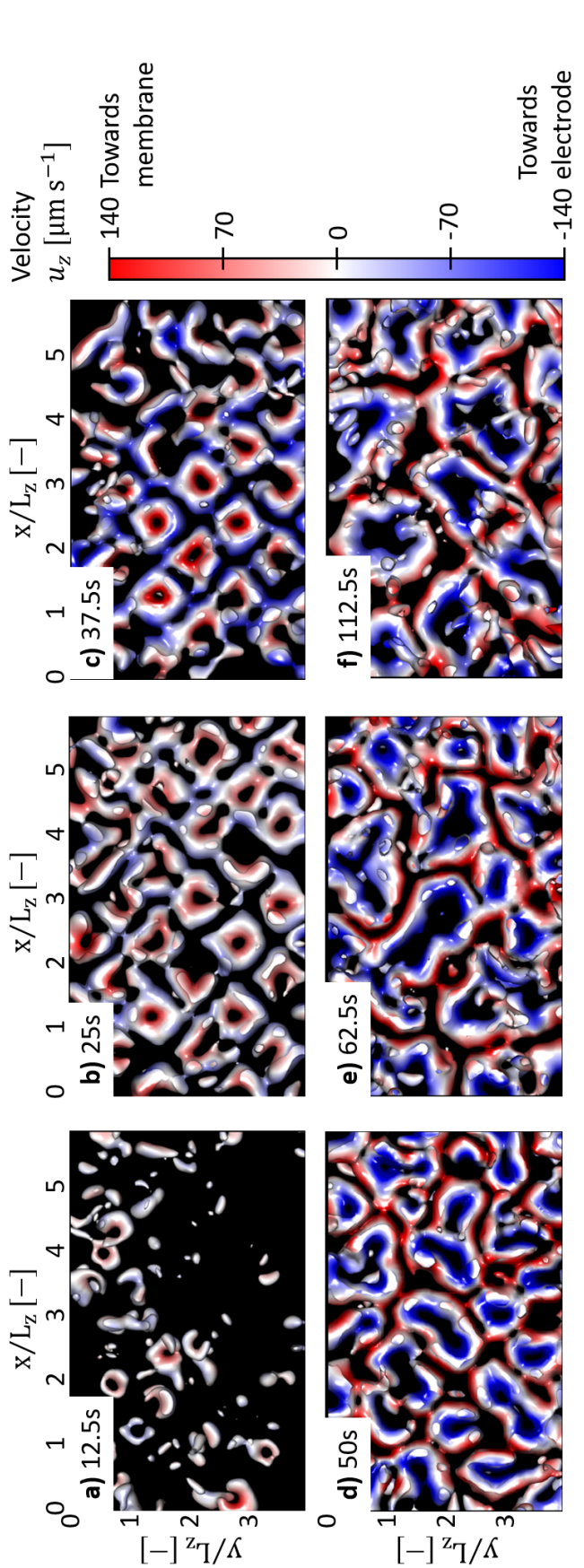

Figure 4.5: Change in the vortex structure and rotational direction towards steady state at the 400 µm P2VP microgel patches. Temporal development of the top view on the vortex structure of the experiment shown in Figure 4.4 **c)** between **a)** 12.5 s to **f)** 112.5 s. The velocity is colored in magnitude and direction according to the scale bar from blue to red.

forces dominate the patches' influence at current densities increasing beyond 30 V_t. Second, the results of Valenca et al. and Davidson et al. suggest that the optimal 2D pattern size is equal to the boundary layer height [Vale2018a; Davi2016]. In our experiment, this would be equal to the membrane to electrode distance of 800 µm. However, we chose this diameter to investigate the influence of a smaller patch diameter on the steady-state vortex field. As a result, the vortex ring diameter doubles from 25 s to 112.5 s, spanning over multiple patches. Interestingly, the presence of the pattern still hinders the formation of the vortex roll structure that would form at an untreated membrane at this current density.

4.4.4 Surface modification offers full control over vortex structure

Surface modification offers full control over vortex structure

We conducted further experiments at 10.08 × magnification with smaller tracer particles with a diameter of 0.86 µm to better compare the vortex ring and patch positions.

Figure 4.6 **a)** and **c)** show two Nafion membranes patterned with P2VP microgels with a 400 µm diameter and a 600 µm diameter, respectively.

The vortex field reconstruction of the experiments at both membranes is shown in Figure 4.6 **b)** and **d)**. In both images, coherent vortex rings emerge that resemble the patterns. Interestingly, the vortices also resemble the slight imperfections in the pattern for the 400 µm case. The rotation of the vortex rings is directed towards the patches as in the experiments at lower magnification with larger particles, see Figure 4.4.

The results show that the patches enforce their structure on EC's build-up in its development regardless of shape and size. Furthermore, even

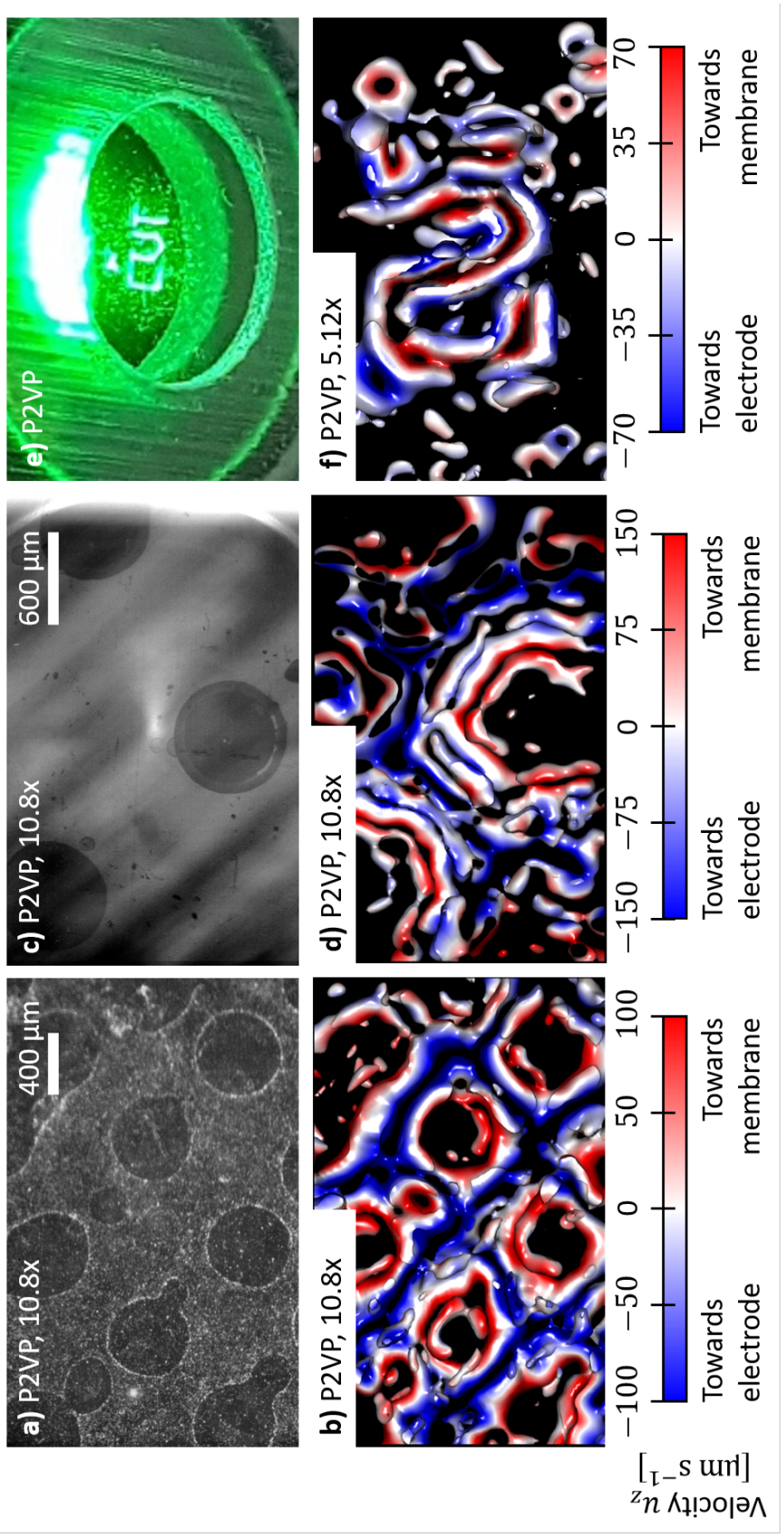

Figure 4.6: Complex P2VP microgel pattern proof full control over vortex field. a) & **c)** P2VP microgel patch pattern with 400 µm and 600 µm diameter show a clear orientation at a magnification of 10.08 ×. **b)** & **d)** Top view of the resulting vortex structures. **e)** Image of the membrane modified with the CVT-logo structure inside the module illuminated by green light. **f)** Top view of the coherent vortex structure after 1.6 s of the experiment at a magnification of 5.12 ×. The velocity is colored in magnitude and direction according to the scale bar from blue to red.

slight imperfections in the patches' geometry are reproduced in the vortex structure, demonstrating that complete geometric control of the EC vortex field can be achieved using this membrane modification method. Therefore, we printed our chairs' 'CVT'-lettering to achieve a structure with varying line distances and direction changes. The pattern was produced by printing lines of overlapping circular patches (see Figure 4.6 **e)**).

Figure 4.6 **f)** shows a snapshot of the vortex structure during the build-up of EC. The vortex field's shape clearly follows the printed structure. The velocity's color map reveals that a pair of vortices builds at the structures with velocity towards the structure in between. This rotational direction was also observed in the previous experiments.

These results prove that the P2VP microgel pattern enforces the build-up of vortex pairs at the structure, completely resembling its shape. The emergence of strong EC vortices only at the structure also shows that a P2VP pattern structure leads to a faster EC build-up. It also gives additional proof that vortices move towards P2VP-coated surfaces.

4.4.5 Velocity statistics of electroconvection at a modified membrane

In an attempt to quantify the effect of the pattern structure on the development of the velocity statistics of the system, we compare the mean square velocity, temporal and spatial energy spectra for the experiments with the untreated (Figure 4.4 **a)**) and 400 µm P2VP-patterned (Figure 4.4 **c)**) membranes plotted in Figure 4.7 and Figure 4.8, respectively.

The mean square velocities in Figure 4.7 show only little velocity build-up until 40 s. Thereafter, the in-plane and out-of-plane velocities develop EC typical maxima. For the in-plane velocity two local maxima emerge, one at the membrane and the other in the middle of the channel. The maximum of the out-of-plane velocity develops at about 0.25 distance to the membrane

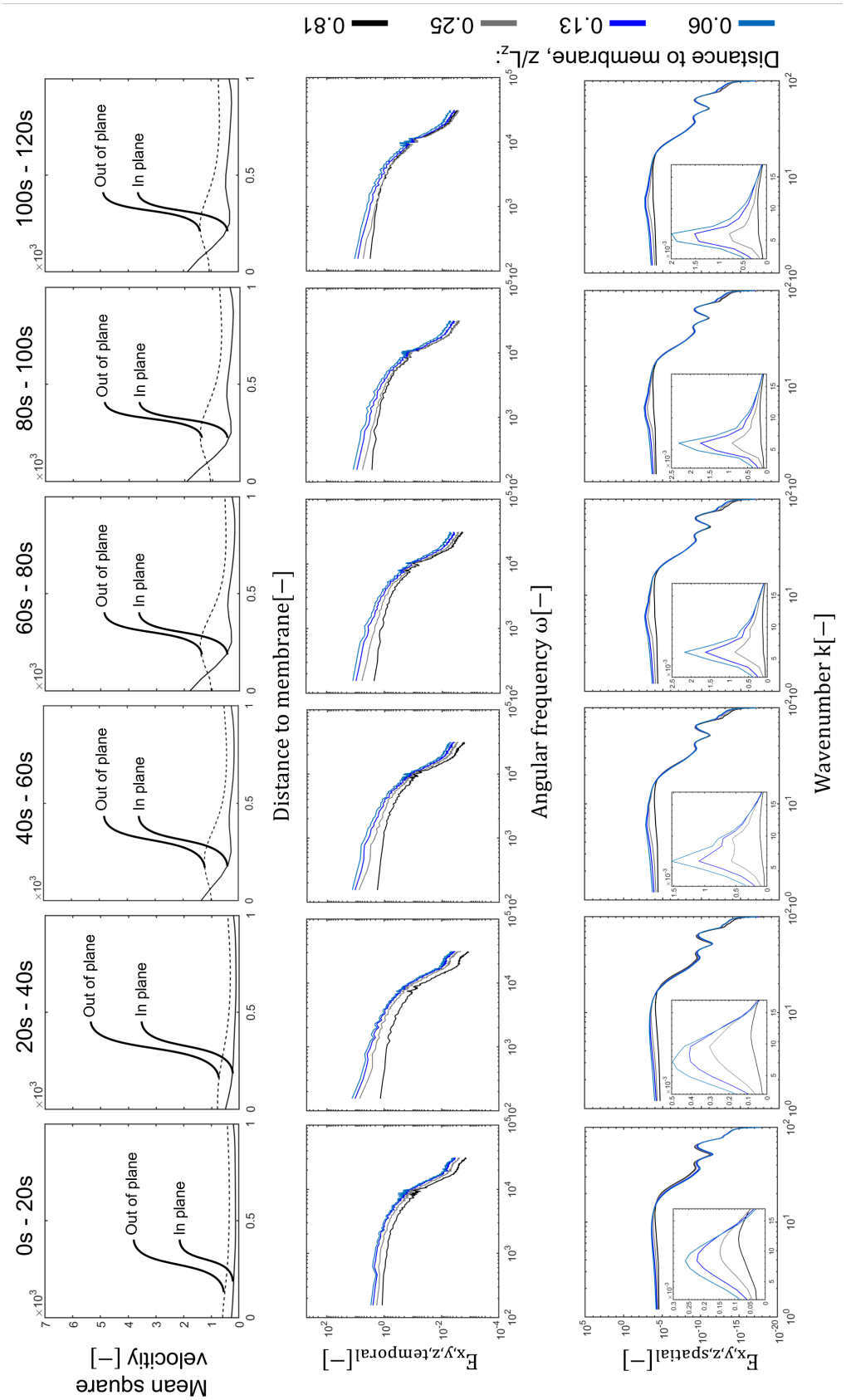

Figure 4.7: Development of the velocity statistics during the experiment with the bare membrane between 0 s to 120 s. The top row shows the mean square velocities of the out-of-plane and one in-plane velocity component. The middle row shows the temporal energy spectra with a double logarithmic scaling at four distances to the membrane. The dotted lines indicate linear sections. The bottom row shows spatial energy spectra with a double logarithmic scaling at four distances to the membrane. The inserts provide a linear scale zoom on the global energy maxima.

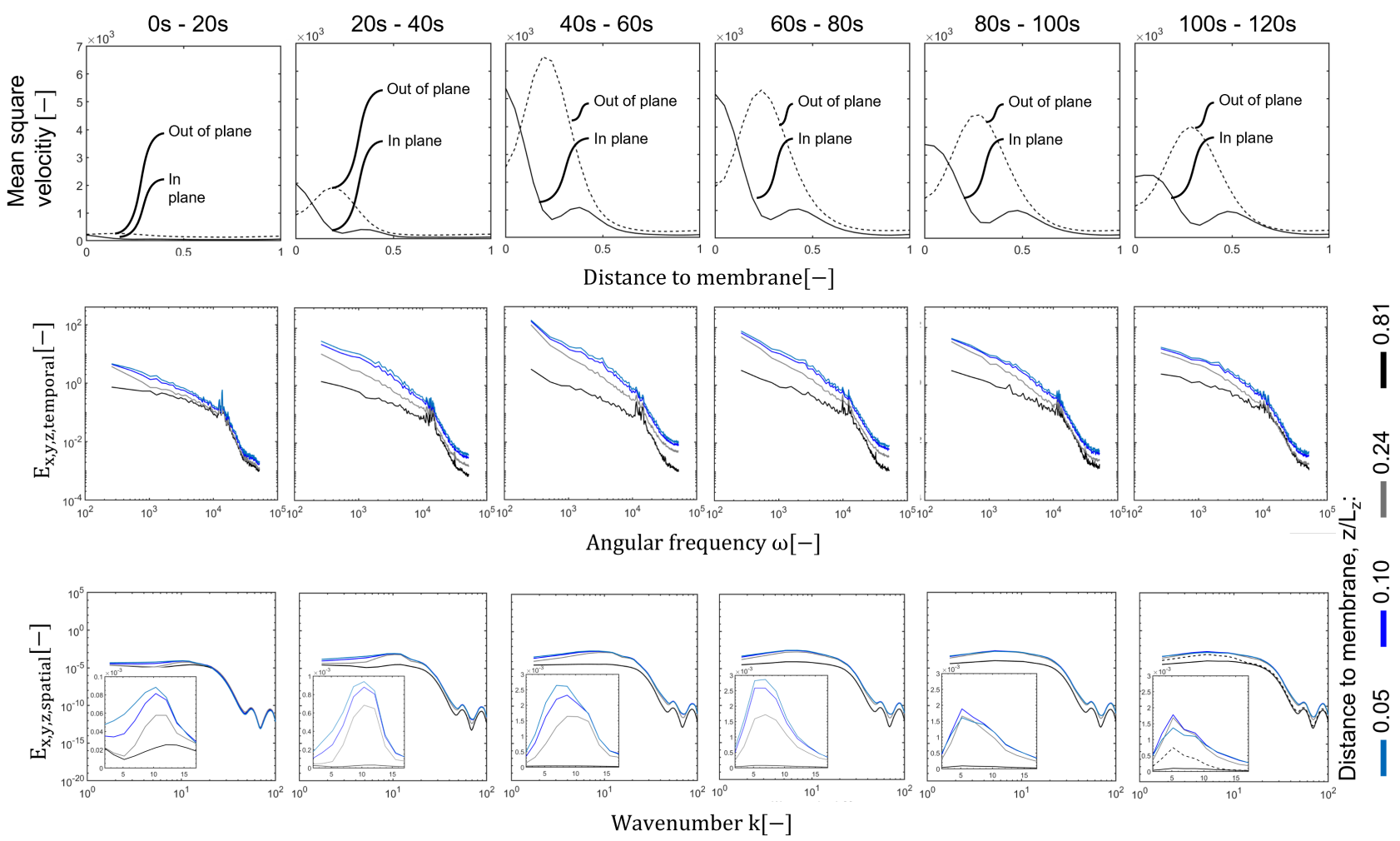

Figure 4.8: Development of the velocity statistics during the experiment with the P2VP-patterned membrane between 0 s to 120 s. The top row shows the mean square velocities of the out-of-plane and one in-plane velocity component. The middle row shows the temporal energy spectra with a double logarithmic scaling at four distances to the membrane. The dotted lines indicate linear sections. The bottom row shows spatial energy spectra with a double logarithmic scaling at four distances to the membrane. The inserts provide a linear scale zoom on the global energy maxima.

which is also the position of the local minimum of the in-plane velocity. Both global maxima reach about the same velocity. The profiles do not change at later time steps suggesting that a steady-state is reached at this point.

These observations are supported by the course of the temporal energy spectra. From 0 s to 20 s, energies of small frequencies show a slow decrease that grows exponentially with increasing frequency. After 20 s, the energies at small frequencies increase in planes close to the membrane which is accompanied with a stronger decrease resulting in the same course of the graphs as described before. This behavior is also observed for the following time steps.

The spatial spectra are evaluated with the same processing and integration scheme described in Chapter 2 even though the vortex field of vortex rolls is not isentropic. The 2D Fourier transformation still exhibits maxima at wavenumbers corresponding to the vortex roll distance. The spatial spectra support the vortex growth seen in the mean square velocities. Between 0 s and 20 s, the graphs' maxima appear at wavenumbers between 8.40 and 12.00 which correspond to dimensionless distances of 0.75 to 0.52. The maxima of planes close to the membrane get more pronounced and shift their locations to 6.00 k corresponding to a dimensionless distance of 1.05 after 40 s.

These results confirm that the vortex rolls reach their maximum size with a roll diameter of 0.5 and a roll-to-roll distance of 1.05.

The mean square velocities of the P2VP-patterned membrane develop differently compared to the untreated membrane, see Figure 4.8. Until 20 s, velocities are low but strongly increase over the first 60 s. At this time step, the maxima positions and their relations are similar to the graphs of the untreated membrane but with approximately 5 times higher velocities. Afterwards, the velocities decrease in each time step to approximately half the values in the out-of-plane velocity and to a third in the in-plane velocities. During that time the positions of the out-of-plane maximum and the local in-plane maximum slightly relocate from 0.19 and 0.38 to 0.29 and 0.48, respectively.

The increase and decrease of the overall velocities also shows in the energy levels of the temporal and spatial spectra. Additionally, both spectra reflect the increased velocities compared the the untreated membrane. Another difference is that the temporal spectra close to the membrane carry a larger share of the energy.

The maxima of the spatial spectra shift from 10.37 to 12.10 at 0 s to 20 s to 5.18 to 6.91 at 100 s to 120 s. These maxima translate to dimensionless vortex ring diameters of 0.61 - 0.52 and 1.21 to 0.91. The spectra at later time steps also seem to be characterized by a broader range of modes. The vortex size changes visible in the maxima of the mean square velocities and the spatial energy spectra correspond to the change in vortex structure analyzed in Figure 4.5.

The statistics reveal that although the vortex sizes of both cases are similar their rotation speeds are different by a large degree as also predicted by the DNSs, see Figure 4.3. This behavior proves that the heterogeneity introduced by the P2VP patches influences the electrical field resulting in larger body forces.

4.5 Conclusions

Our results show that the membrane modification technique offers complete control over the vortex structure of electroconvection.

Patches of P2VP microgels that introduce a large zeta potential contrast to the membrane lead to the structuring of the vortex field. While the patch geometry has an optimum range in current density to structure the vortices, the orientation is lost beyond this range. This behavior allows not only a geometric control of the vortices but also a control of the onset of fully-developed EC at a certain operating point in an electrochemical process. Even with PNIPAM-co-Aac microgel patches, the usual vortex roll pattern observed at homogeneous Nafion membranes is suppressed, although the zeta potential difference contrast is significantly lower. We attribute the effects seen in the experiments of Roghmans et al. [Rogh2019] in part to this

change in the vortex structure. Therefore, future micro- and macroscopic studies should focus on the effect of tailored 3D vortex structures on the limiting current density and plateau length.

Our simulations additionally show that the vortices orientate towards the surface with the higher zeta potential. In accordance, our experiment with P2VP microgel patterns shows localization of vortex rings with a vortex rotational direction towards the patches' centers. Control over the rotational direction of the EC vortex rings was previously hypothesized to be a key to an optimized membrane modification [Rogh2019]. The experiments presented in this study demonstrate that the geometry and the zeta potential allow for control of the rotational direction of the vortex rings.

The possibility of controlling both the shape and rotational direction of the electroconvective vortex field motivates the development of more complex, transport enhancing modifications of ion-exchange membranes. With the increasing influence of EC, the share of water splitting to the ion transport will also decrease. Additionally, the modification method is easily upscalable to cover larger membrane areas. Further progress will enable efficient use of the overlimiting current region in industrial-scale processes leading to decreased material and investment costs.

4.6 Appendix

4.6.1 Simulation parameters

The parameters used in the simulation are presented in Table 4.3 in their dimensional form.

Table 4.3: Simulation parameters.

Parameter	Description	Value
ΔV	Applied voltage	2.7×10^{-3} V to 3.1 V
σ	Patch charge	–0.1 mol m^{-3} to 0.1 mol m^{-3}
D	Diffusion coefficient	1×10^{-9} m^2 s^{-1}
ρ	Mass density	1×10^3 kg m^{-3}
μ	Dynamic viscosity	1×10^{-3} kg m^{-1} s
ε_r	Relative permittivity	84.11
z_i	Charge valence	± 1
T	Absolute temperature	300.68 K
H	Distance between membrane and reservoir	10×10^{-5} m
c_{res}	Reservoir ion concentration	1 mol m^{-3}
c_{mem}	Cation concentration on membrane surface	2 mol m^{-3}

4.6.2 Steady-state current density over patch charge in simulations

Additional to the simulation results at 0, -0.1, and 0.1 patch charges presented in the chapter, simulations with varying patch charges were also conducted. The steady-state results between 5 · V_t to 120 · V_t with patch charges between 0 and 0.1 in positive and negative direction are shown in Figure 4.9.

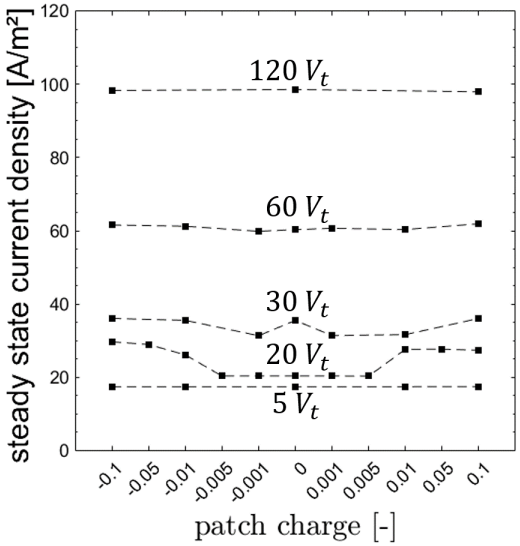

Figure 4.9: Steady-state current density reached at varying patch charge and potential in the simulations.

For both the lowest potential of 5 · V_t and the highest of 120 · V_t, the patch charge does not influence the reachable current density, which is in line with the results presented in Figure 4.3. At 60 · V_t, the current density only slightly increases with increasing positive or negative patch charge. The patch charge shows a more pronounced effect at 30 · V_t and 20 · V_t. At 30 · V_t, the simulations with patch charges of -0.001, 0.001, and 0.01 reach lower current densities as the reference and the other cases. Only the simulations at 20 · V_t show a significant increase in current density for patch charges larger than 0.01 in the positive and negative direction.

On the one hand, the results indicate that a minimum potential is needed to evoke electroconvection (EC) even when using a surface charge modified membrane. On the other hand, a too large potential introduces forces with a bigger influence than the patches. When looking into the velocity field of such simulations, the EC vortices freely move over the membrane surface without any patches' structuring effect.

The simulations with decreased current density at $30 \cdot V_t$ additionally show that vortices are held steady at the patches, while in the cases with high current density, movement of vortices is visible. In contrast, the simulations at $20 \cdot V_t$ show vortex formation only at sufficiently high patch charges. These findings indicate that charged patches improve ion transport when leading to an early onset of EC at potentials in the plateau region and result in a current density decrease when hindering the free movement of established EC vortices. Therefore, a sufficient coating should introduce a zeta potential difference which on one side leads to pronounced EC development but on the other side is low enough to enable vortex movement.

4.6.3 Membrane scaling

The presented experiments were conducted at a current density of 148 µA to operate close to the plateau region. Additionally, We conducted experiments at larger current densities to evaluate EC's effect also at large overlimiting currents. However, increasing resistance in such experiments were found. Such a behavior is not observed with untreated membranes.

When opening the module after the experiments, a blue scaling was found on the membrane, see Figure 4.10 **a)**. SEM and EDX imaging were performed to determine the structure and chemical composition of the crystalline scaling. The SEM image in Figure 4.10 **b)** reveals flat star-shaped crystals in the highlighted area. In the simultaneously recorded EDX, only little carbon and fluoride (Figure 4.10 **c)** and **d)**) are detected compared to the bare membrane. The rest of the images show

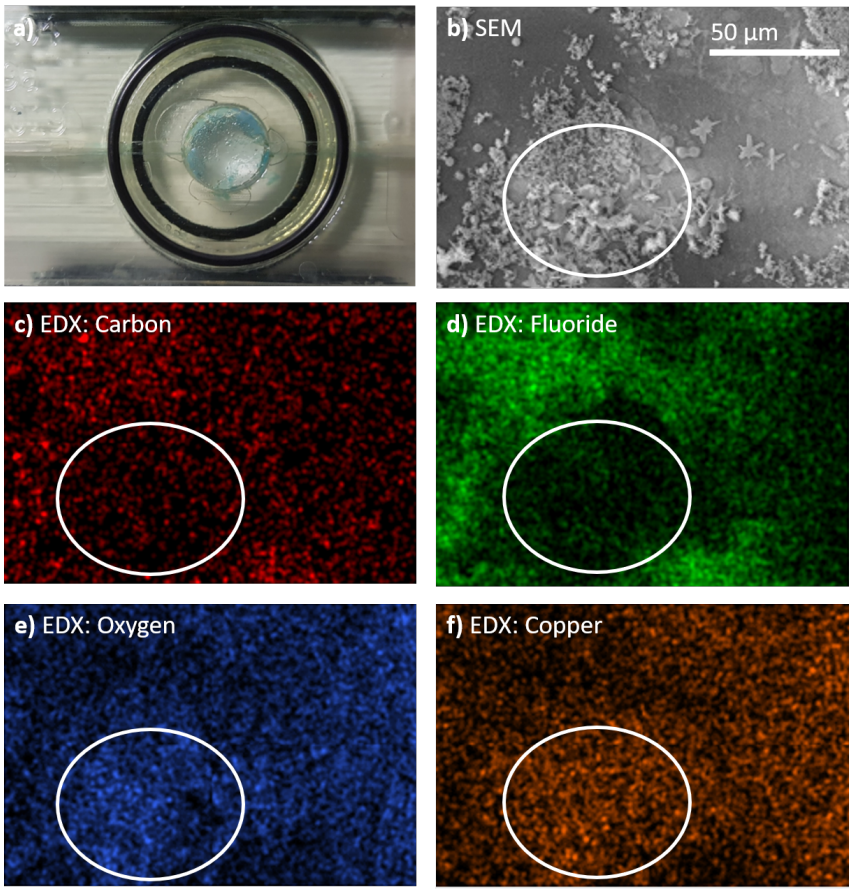

Figure 4.10: Analysis of scaling found on a membrane after an experiment at 400 µA. a) Image of the blue scaling layer on top of the membrane. **b)** SEM image showing the crystalline structure of the scaling. **c)** - **f)** EDX analysis for carbon, fluoride, oxygen, and copper, respectively.

a higher content of both substances matching the membrane material's chemical composition. Figure 4.10 **e)** and **f)** show larger oxygen and copper contents instead. These molecules indicate the formation of CuO or $\mathrm{Cu(OH)_2}$, which appears as a mostly water-insoluble crystalline substance, as also concluded by Hang et al. [Chan2010].

The formation of CuO occuring only at modified membranes at increased potentials would further indicate that the microgel patches enhance water dissociation. Water dissociation would supply $\mathrm{OH^-}$ to the fluid-membrane interface, which could directly crystallize with copper ions transported towards the membrane surface.

5

Interaction between spacer hydrodynamics and electroconvection

Parts of this chapter are in preparation for publication:
Felix Stockmeier, Lucas Stüwe, Elizaveta Evdochenko, Niklas Köller, Sebastian Brosch, Christian Kneppeck, Stephan Musholt, Katharina Albert, John Linkhorst, and Matthias Wessling, "Interaction Between Spacer-Altered Bulk Hydrodynamics and Electroconvection", *Journal to be decided*

5.1 Introduction

Industrial-scale electrically-driven membrane processes like electrodialysis (ED) are operated only in a limited current density range [Mani2020]. During operation at a high driving force, concentration polarization (CP) evolves as a fluid-sided resistance in such membrane systems. This increased resistance manifests as a plateau region in a current density over potential plot, see Figure 5.1 **a)**.

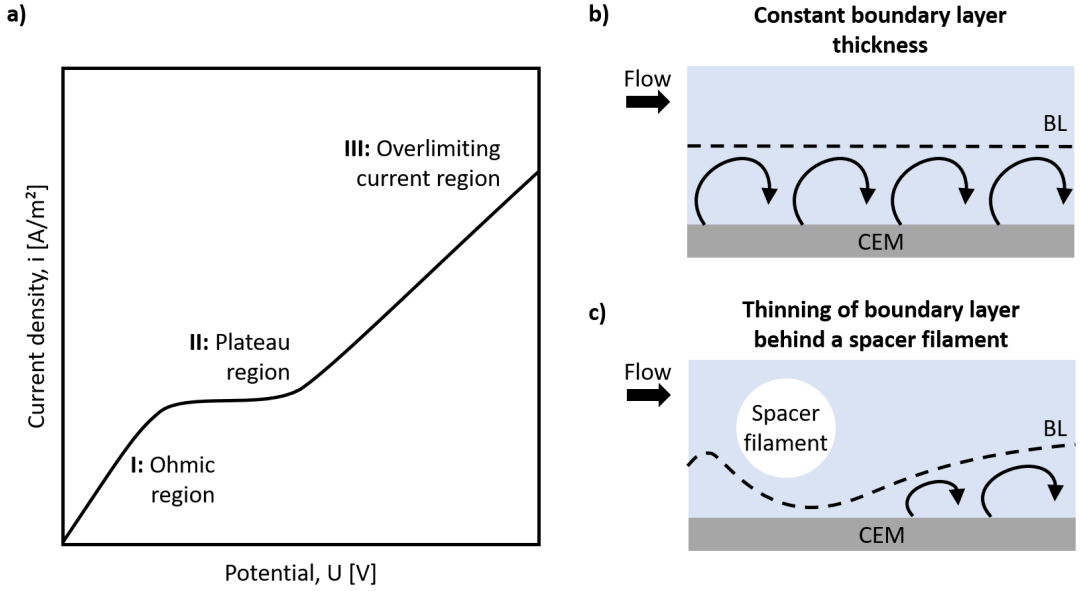

Figure 5.1: Current density over potential graph and influence of spacer structures of the diffusion boundary layer. **a)** Sketch of the typical current density over potential graph for an electrically driven membrane process showing three distinct regimes. **b)** Cross-flow over the membrane results in a constant boundary layer (BL) thickness. EC vortices form helical structures in the BL. **c)** Circular-shaped spacer structure located in the bulk flow resulting in a thinning of the boundary layer (BL).

This limiting current density can be overcome when applying large potentials resulting in an overlimiting current (OLC). At these potentials, convective vortices, so-called electroconvection (EC), mix the depleted layer close to the membrane in the OLC region. Thereby, the EC vortices transport ion-rich solution from the bulk towards the membrane. The increased concentration enables larger current densities. In systems with highly efficient membranes, the OLC is mainly enabled by EC while

only a small portion of the current is attributed to unwanted water splitting [Niko2014; Niko2017; Mani2020]. In cases with significant water splitting, the dissociation of water to H^+ and OH^- ions at the membrane supplies additional ions and allows a higher current density [Zabo1988]. However, this transport is not desired and decreases the process efficiency. Additionally, pronounced water dissociation leads to drastic pH changes accompanied by other negative effects like scaling [Stra2010].

On industrial scale, ED processes are usually run in the underlimiting regime to avoid water splitting and its negative effects. Instead, spacers are introduced in the electrolyte channels, which provide stability to the stack of membranes and promote mixing, see Figure 5.1 **b)** and **c)**. The increased mixing influences the boundary layer thickness and, therefore, the limiting current density which expands the operational range [Cowa1959].

With recent advances in the production of membrane materials that reduce water splitting and membrane surface modifications promoting EC, the industrial use of OLC comes into reach. The operation at high current densities in smaller membrane modules would significantly decrease the investment costs of industrial processes. Belova et al. [Belo2006] also described a balancing interaction between water dissociation and EC. Therefore, the complex interaction of EC and spacer-altered hydrodynamics in the OLC regime is of particular interest when aiming for a maximum contribution of EC to the OLC.

Kwak et al. [Kwak2013a] demonstrated that EC appears in settings found in the industry. Additionally, they visually analyzed EC vortices' movement in a pumped electrolyte in a micro-fluidic chip. Kwak et al. [Kwak2013b] found that the vortex movement speed is independent of the applied voltage. Their research confirmed that electroconvection occurs in application-oriented systems in which the boundary layer is primarily affected. Pham et al. [Pham2016] reported the 3D structure of EC vortices in a pumped electrolyte in direct numerical simulations (DNSs). Their simulation showed that the vortices move as helices along with the flow over the membrane surface. In further DNSs, Guan, Riley, and Novosselov [Guan2020] con-

firmed the organizing effect of shear flow on the 3D vortex structure of EC. Vortex structures were suppressed in the perpendicular flow direction. This effect might be important when considering EC's interaction with the flow conditions in spacer-filled channels.

Various studies analyzed the effect of different flow conditions on ion transport in ED stacks. It becomes evident that shear flow reduces the boundary layer thickness leading to shorter diffusion lengths. However, electroconvection is also suppressed [Tana1991; Khai2011; Urte2013]. Tanaka [Tana2012] concluded that the ion transport in the boundary layer of a static electrolyte is governed by gravitational convection or electroconvection while migration and diffusion dominate in a thin boundary layer of a pumped electrolyte. However, all the above studies neglected the presence of spacers.

Tadimeti et al. [Tadi2016] modeled a spacer-filled electrodialysis channel in 2D. Their results show a high dependency of the ion removal on the flow profile in the channel. Additionally, they found that the boundary layer thickness is reduced to a minimum in corrugated membrane channels. Experimental studies of the hydrodynamics in a spacer-filled ED channel are also limited to 2D visualization [Kim2017; Kim2021]. Kim et al. [Kim2017] showed the impact of hydrodynamic change for varying spacer placement on the ion transfer. They report that a central positioning of spacer filaments results in an about 40% limiting current increase. However, the study was limited to 2D parallel rods instead of a 3D spacer structure with low flow velocities. These rods also had small diameters compared to the channel height, which leaves extrapolation to industry-relevant conditions an open question. The influence is reported only in the limiting current regime without extension of their experiments to the OLC regime.

In industry-relevant 2D and 3D simulations, Fimbres-Weihs and Wiley [Fimb2007] identified differences in mass transfer enhancement of non-woven net spacers in a membrane channel of a pressure-driven process. They stressed the importance of 3D effects such as stream-wise vortices,

open span-wise vortices, and higher wall shear rates vertically to the bulk flow direction. Another correlation in 3D simulations was revealed between locations of highest mass transfer and the presence of both stream-wise and span-wise vortices. Since these simulations considered a pressure-driven process, the additional effect of EC was omitted.

Current studies lack the analysis of EC with forced flow in a spacer-filled channel at significant flow velocity, current density, and aspect ratio. However, this knowledge is a prerequisite for the effective use of the OLC in industrial electrically-driven membrane processes.

This chapter describes a method to reconstruct the 3D velocity field of a pumped electrolyte in a spacer-filled channel at industry-relevant length and time scales under the action of an electric field. The results indicate the share of EC on the boundary layer mixing.

5.2 Experimental details

The experiments are conducted similar to the description in Chapter 2. However, recording of EC in forced electrolyte flow demanded the design of an advanced electrochemical cell described in the following section.

5.2.1 Electrochemical flow-through module

For experiments with forced flow, an advanced electrochemical cell was designed, see Figure 5.2. The cell design's core features are Nafion (Nafion perfluorinated resin solution 20 wt. %, Merck KGaA, Germany) coated microscope glass slides (75 mm $\times$ 25 mm $\times$ 1 mm) that act as transparent ion-exchange membranes as well as cation-bridges inspired by Kang and Kwak [Kang2020]. To prevent the Nafion from detaching, the glass slides need to be chemically treated. The desired membrane area is masked with tape and then plasma-activated. The activated glass is silanized with N-Trimethoxysilylpropyl-N,N,N-trimethylammonium chloride (TTACl, 50% in

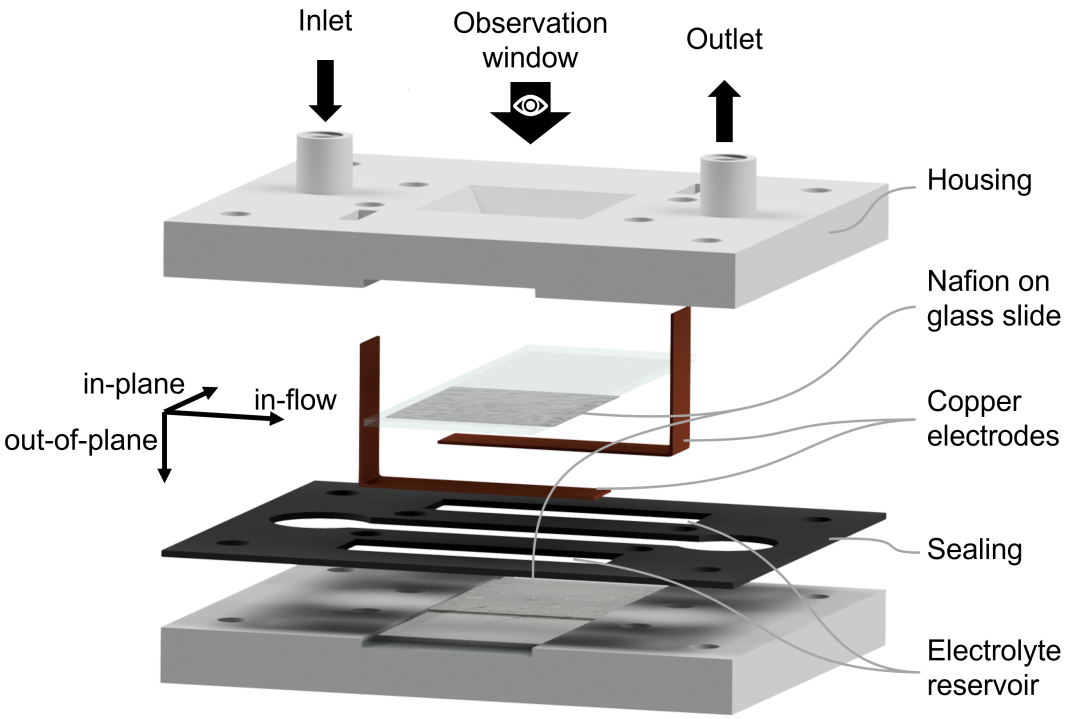

Figure 5.2: Cell design for electrochemical experiments in a pumped electrolyte with simultaneous µPTV recording. The electrochemical cell consists of two 3D printed housing parts which are sealed with a flat sealing forming the flow channel and two electrolyte reservoirs. The coordinate system has its origin at the upper, desalinating membrane. A cross-section of the module is illustrated in Figure 5.3

Methanol, Thermo Fisher (Kandel) GmbH, Germany) for 30 minutes before coating [Szen1986]. The channel's width of 10 mm confines the active membrane area to 2.5 cm^2. For sealing, we use a 2 mm thick, foamed EPDM sheet, which allows adjusting the channel height between 1 mm and 0.5 mm.

The chosen cell design also features the delocalization of the copper electrodes to the sides of the cell. Thereby, one layer of housing and sealing can be omitted, the flow channel can be easily integrated in the sealing layer, and the electrodes do not obstruct the view through the membrane compared to the previous design illustrated in Chapter 2.

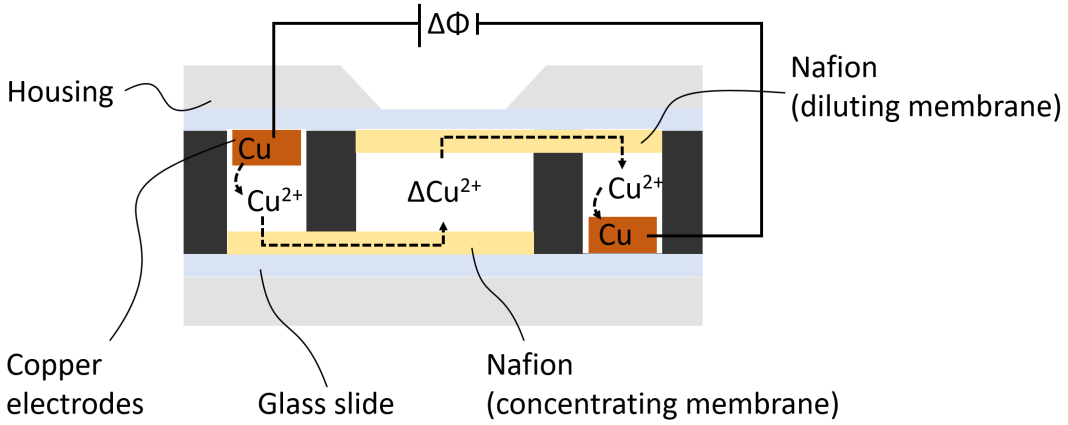

Figure 5.3: Ion pathway and concentration gradient in new cell design. The illustration shows a cross-section of the newly desigend module. the pathway of copper ions is indicated with arrows.

A concentration gradient is sustained during operation between the cathode and anode electrolyte reservoir due to faradaic copper deposition and dissolution, respectively. This gradient is carried over to the flow channel through the Nafion. This concept is illustrated in Figure 5.3. Since the cation transport in Nafion is faster than in the electrolyte, a homogeneous cation concentration inside the Nafion can be assumed. The gradient between both Nafion coatings further results in an electric field as given by Poisson's equation 2.18. A concentration difference between the electrolyte reservoir (5 mM) and the flow channel (1 mM) ensures stronger desalination and, thus, the evolution of EC in the latter.

5.2.2 Velocity measurement

Micro particle tracking velocimetry (µPTV) is used to reconstruct the 3D flow field of the electrolyte, which is seeded with 0.001 wt% tracer particles. The cameras record the inert, fluorescent polystyrene microspheres (Thermo Scientific, Waltham, MA, USA; diameter = 3.2 µm; zeta potential = −14.9 mV). The recorded volume at a magnification of $5.12\times$ and a halfway closed aperture is 4.9 mm $\times$3.1 mm $\times$0.8 mm with 1280 $\times$ 800 pixel resolution in x- and y-direction. The depth of the recorded volume of 0.8 mm is larger than the height of the electrolyte chamber with 0.5 mm. Therefore, it is possible to reconstruct the velocity field over the full height of the chamber, see Fig 5.4.

The recorded images are then post-processed to reconstruct the 3D particle tracks and convert them into velocity fields as described in 2.4. The software DaVis (version: 10.0.5.47779, LaVision GmbH, Göttingen, Germany) also enables plotting coherent vortex structures using the λ_2-method [Jeon1995]. This method is used to visualize coherent vortex structures depicted as isosurfaces at a specific eigenvalue λ_2. The 3D velocity field can also be visualized as streamline in ParaView (version: 5.9.1, Kitware, Inc., USA). The velocity fields statistics can be further extracted according to Sec. 2.6.

5.2.3 Experiments with applied flow and velocity reconstruction

We conduct experiments with specific combinations of current density, Reynolds number, and spacer configuration. The current density through the module is fixed by a potentiostat (Interface 1010E, Gamry, Pennsylvania, USA). In experiments with forced flow, the electrolyte is pumped with a syringe pump (PHD ULTRA Syringe Pump, Harvard Apparatus, MA, United States). Additionally, a commercial non-woven net-spacer structure

(0.25 mm^2 fiber diameter, 0.5 mm spacer height, 1 mm$\times$1 mm rectangular base shape) is inserted into the flow channel in some experiments.

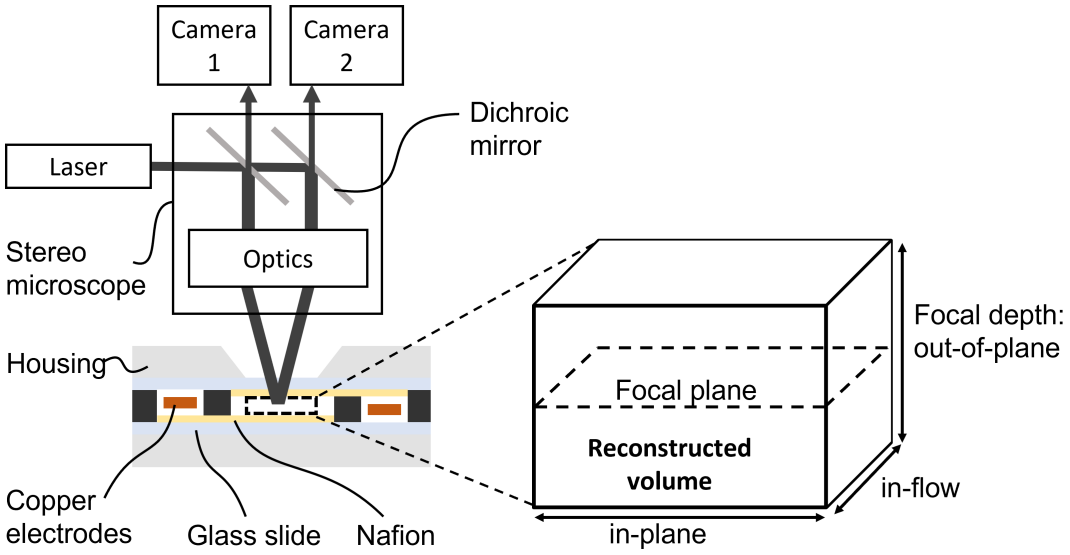

Figure 5.4: Schematic illustration of the setup for stereo micro particle image velocimetry. The setup consists of a laser that illuminates a sample volume through a stereo microscope which splits the laser beam into two separate beams. The fluorescence response returns through the microscope and is recorded by two slightly angled high-speed cameras. This technique allows the recording of tracer particles in a 3D volume of the electrochemical cell's flow channel depicted as a cross-section.

During an experiment, the electrolyte solution in the flow channel of the electrochemical chip is seeded with the tracer particles. The microscope is focused in the channel's middle enabling the reconstruction of the velocity field over the entire channel height as illustrated in Figure 5.4. The recording is started when the flow reaches a steady state.

5.3 Results and discussion

Before quantifying the interaction of electroconvection (EC), forced flow, and spacer hydrodynamics, we first conducted experiments similar to Chapter 3 in the newly designed module for validation of the concept.

5.3.1 New module design validation

The validation experiment was conducted at about 6 · i_{lim} without pumped electrolyte comparable to the conditions in Chapter 3.

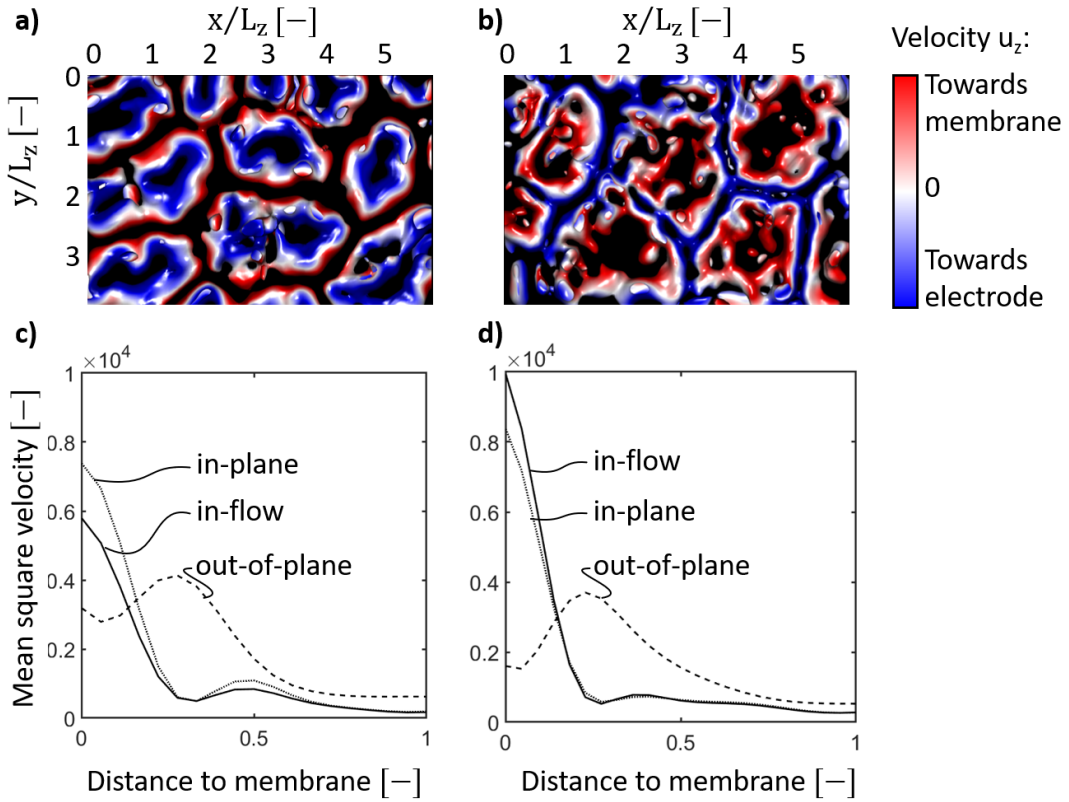

Figure 5.5: Comparison of vortex structure, rotational direction, and velocity components between the conventional and new module design. **a)** and **c)** are reprinted results measured in the conventional cell from Chapter 3. **b)** and **d)** show the results measured with the new module design at about 6 · i_{lim}. **a)** and **b)** display top views on isosurfaces of coherent vortex structures and their rotational directions. The velocity is colored in magnitude and direction according to the scale bar from blue to red. The graphs in **c)** and **d)** plot the respective mean square velocities of all three velocity components over the distance to the upper, desalinating membrane.

Figure 5.5 shows the comparison of the coherent vortex structures and velocity profiles in the cell used in Chapter 3, **a)** and **c)**, and the newly designed cell presented in this chapter, **b)** and **d)**. The vortex structures in Figure 5.5 **a)** and **b)** are similar in shape and size, both forming oval slightly edged vortex rings with diameters between 1 to 2 times the channel height. However, while the vortex centers in Figure 5.5 **a)** rotate towards

the electrode, the centers in the new cell shown in Figure 5.5 **b)** rotate in the opposing direction.

For the conventional cell, the graphs of each of the three velocity components over the cell height in Figure 5.5 **c)** exhibit the typical shapes known from Chapter 3. The in-plane and in-flow velocities have their maxima at the diluting membrane (0 distance to membrane) followed by a local minimum 0.28 distance to membrane and a local maximum at 0.5 distance to membrane. The distance between both maxima marks the turning points and therefore the average height of the electroconvective vortices. The out-of-plane velocity has a maximum at the position of the local in-plane and in-flow minima. At this height, the vortices have the largest velocity normal to the membrane. The out-of-plane velocity decreases towards both ends of the graph.

The velocity profiles recorded in the new cell design in Figure 5.5 **c)** are in the same order of magnitude with good agreement in their distinctive maxima and minima. Significant differences are seen in slightly larger in-plane and in-flow velocities at the diluting membrane and their flattened local maxima at 0.5 distance to membrane.

The results validate that the new module design is suitable for quantitative analysis of EC, yielding comparable data to the conventional design. However, the reversed rotational direction poses a significant challenge for interpretation. Considering the theory discussed in Chapter 4, disturbances in the electric field lines could cause this phenomenon. These disturbances could result from the casting of Nafion on glass which might result in slightly inhomogeneous membranes. Despite this disparity, the similarities in vortex structure and velocity profiles prove enough comparability to use the new module design for experiments with forced electrolyte flow.

5.3.2 Electroconvection under forced flow

After validation of the new module, we conduct experiments that investigate the interaction of electroconvection with increasing forced flow. In these experiments, we vary the Reynolds number between 0.1 and 8.

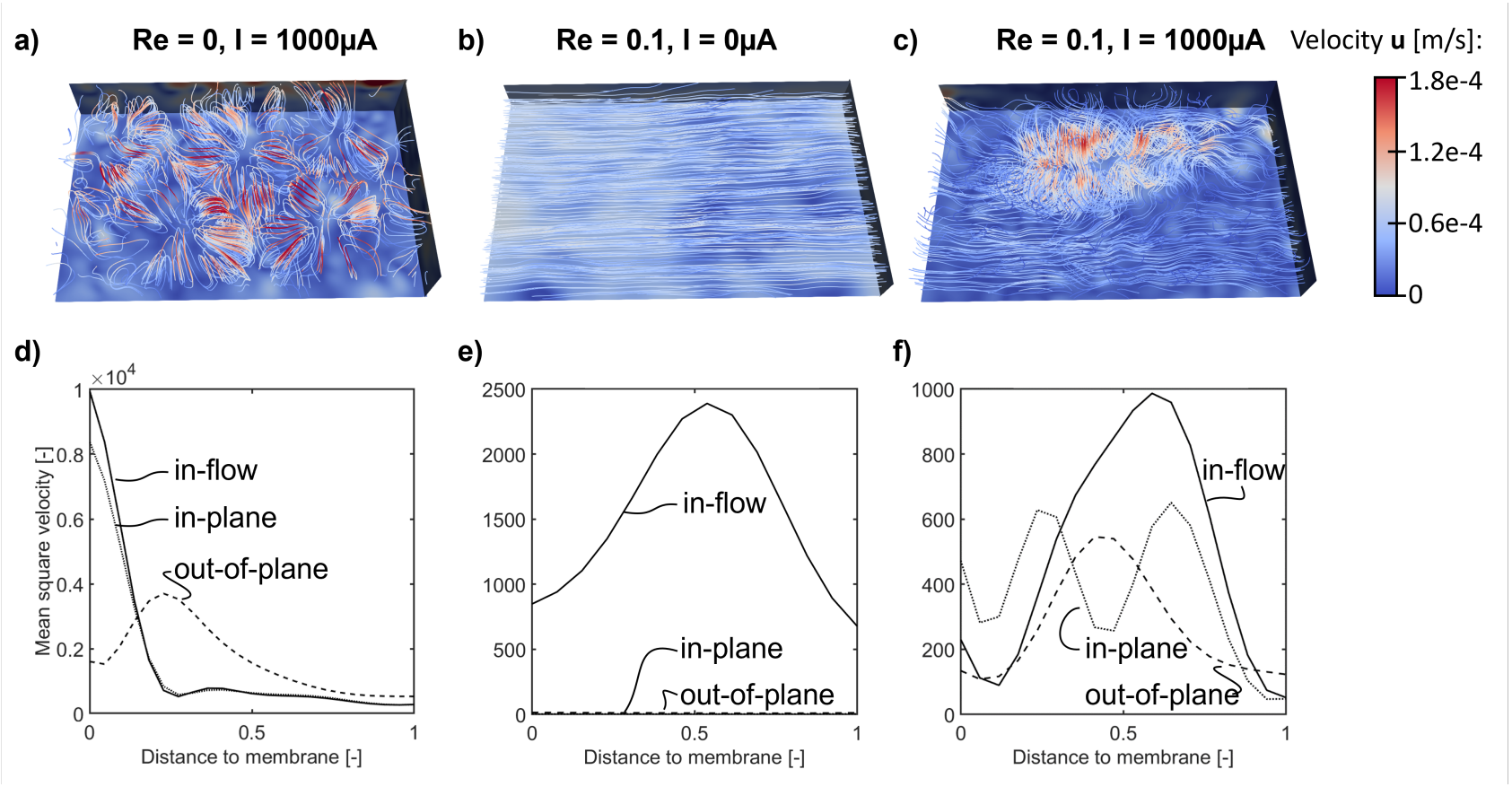

Figure 5.6: Flow field and velocity profiles of electroconvection and forced flow. The flow field is shown as streamlines colored by the magnitude of the absolute velocity from blue to red. **a)** and **d)** show the reference at Re = 0 and 1000 μA. **b)** and **e)** show the experiment with forced flow at Re = 0.1 and 0 μA. **c)** and **f)** show the combined experiment at Re = 0.1 and 1000 μA.

Figure 5.6 shows streamlines of the flow field with and without the presence of an electric field and graphs of their respective velocity components. As a reference, Figure 5.6 **a)** shows a streamline representation of the previous data from Figure 5.5 **b)** and the velocity profiles from Figure 5.5 **d)**. The streamlines capture the vortex ring structure as torus shapes but drop the additional information on the rotational direction instead of showing the absolute flow velocity. The absolute flow velocity is highest close to the desalinating membrane and declines with distance to that membrane.

In contrast, pumping the electrolyte at a Reynolds number of Re = 0.1 without applied current density results in a laminar flow profile with only slight disturbances and lower velocities visible in Figure 5.6 **b)** and **e)**. The graph of the velocity components emphasizes this observation showing a parabolic flow profile in the in-flow direction and negligible in-plane and out-of-plane velocities. The velocities at both membranes differ from zero due to low resolution. Close to surfaces, the prevailing large velocity gradients lead to significant averaging, as already discussed in Chapter 3.

The combined effects of a forced flow and an electric field result in stretched oval-shaped vortex rings carried along with the flow as shown in Figure 5.6 **c)**. In this case, the largest absolute velocities are found close to the top membrane. Streamlines divert from a straight, laminar profile in the whole volume. The velocity profiles in Figure 5.6 **f)** also confirm the superposition of the EC vortex field with the laminar flow profile. The in-flow velocity profile slightly defers from a parabolic shape with its maximum shifted towards the bottom membrane. The in-plane and out-of-plane components show distinct maxima and minima typical for EC vortices indicating that the vortices stretch over the whole module height.

While the overall flow velocities in the cases of forced flow with and without applied current density are in the same order of magnitude, the velocities in the case without flow reach values four times as high.

The results conclude that the superposition of EC and forced flow slows down in the rotational velocities generated by the EC.

The impact of increasing velocity on the superimposed flow profiles of EC and forced flow is further investigated at Reynolds numbers of Re = 1

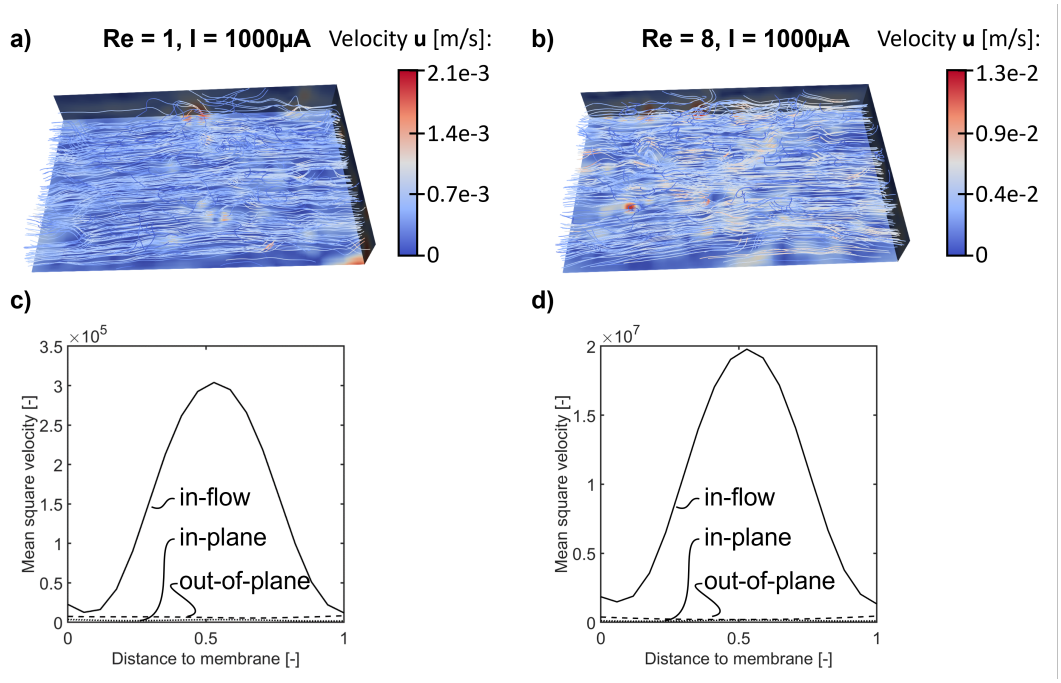

Figure 5.7: Flow field and velocity profiles of electroconvection with increasing forced flow. The flow field is shown as streamlines colored by the magnitude of the absolute velocity from blue to red. **a)** and **c)** show the experiment with forced flow at Re = 1 and 1000 µA. **b)** and **d)** show the experiment with forced flow at Re = 8 and 1000 µA.

and Re = 8 in Figure 5.7. In both cases, disturbances in the streamlines still indicate the appearance of EC, see Figure 5.7 **a)** and **b)**.

Comparable to Re = 0.1, the velocity components in Figure 5.7 **c)** and **d)** show laminar profiles in the in-flow velocity. However, impact of EC is only slightly visible in the in-plane and out-of-plane velocity components.

These results emphasize that forced flow suppresses EC with increasing Reynolds number. The increasing shear in the boundary layer with increasing velocity restricts the height of the EC vortices before the faster cross-flow disrupts their structure. Therefore, recordings close to the membrane surface with larger magnification and smaller particles become necessary to visualize the layer in which strong in-plane and out-of-plane velocities prevail. However, the movement of the currently used particles might be influenced by electrostatics in the direct vicinity of the membrane surface. This interaction negates the assumption of inert tracer particles. Novel

tracer particles with adjustable zeta potential could offer a solution to this challenge.

5.3.3 Electroconvection under forced flow with commercial spacer

This chapter builds on the insights of the previous results and aims to evaluate the interaction of EC and laminar flow profiles through a spacer-filled channel. Therefore, we inserted a commercial net-type spacer into the flow channel. Figure 5.8 displays the streamlines and flow profiles of EC, forced electrolyte flow at Re = 0.1, and their combination.

The vortex structure visualized by streamlines of the reference experiment without forced flow in Figure 5.8 **a)** displays chaotically distributed vortex rolls. Similar to the experiment without spacer, the largest velocities are located close to the desalinating membrane. The velocity profiles in Figure 5.8 **d)** show the typical high in-flow and in-plane velocities close to the top membrane and their local maximum at about 0.38 distance to the membrane, marking the height of the EC vortices, which is smaller compared to the case without a spacer. In between, the out-of-plane velocity has its maximum. The overall velocities are also smaller compared to the case without a spacer.

The EC that emerges between the spacer structure is hindered in developing its typical structure resulting in smaller and slower vortices. However, its specific flow profile can still be observed.

When applying a forced flow without electric field, the previous laminar flow profile is disturbed by the spacer. Figure 5.8 **b)** depicts the streamlines through the spacer structure. The streamlines flow in a regular, wavy pattern around the spacer with the largest velocities close to the desalinating membrane. The velocity profiles in Figure 5.8 **e)** reflect this observation. The in-flow velocity decreases from the top to the bottom membrane. The in-plane and out-of-plane velocities are an order of magnitude smaller, with

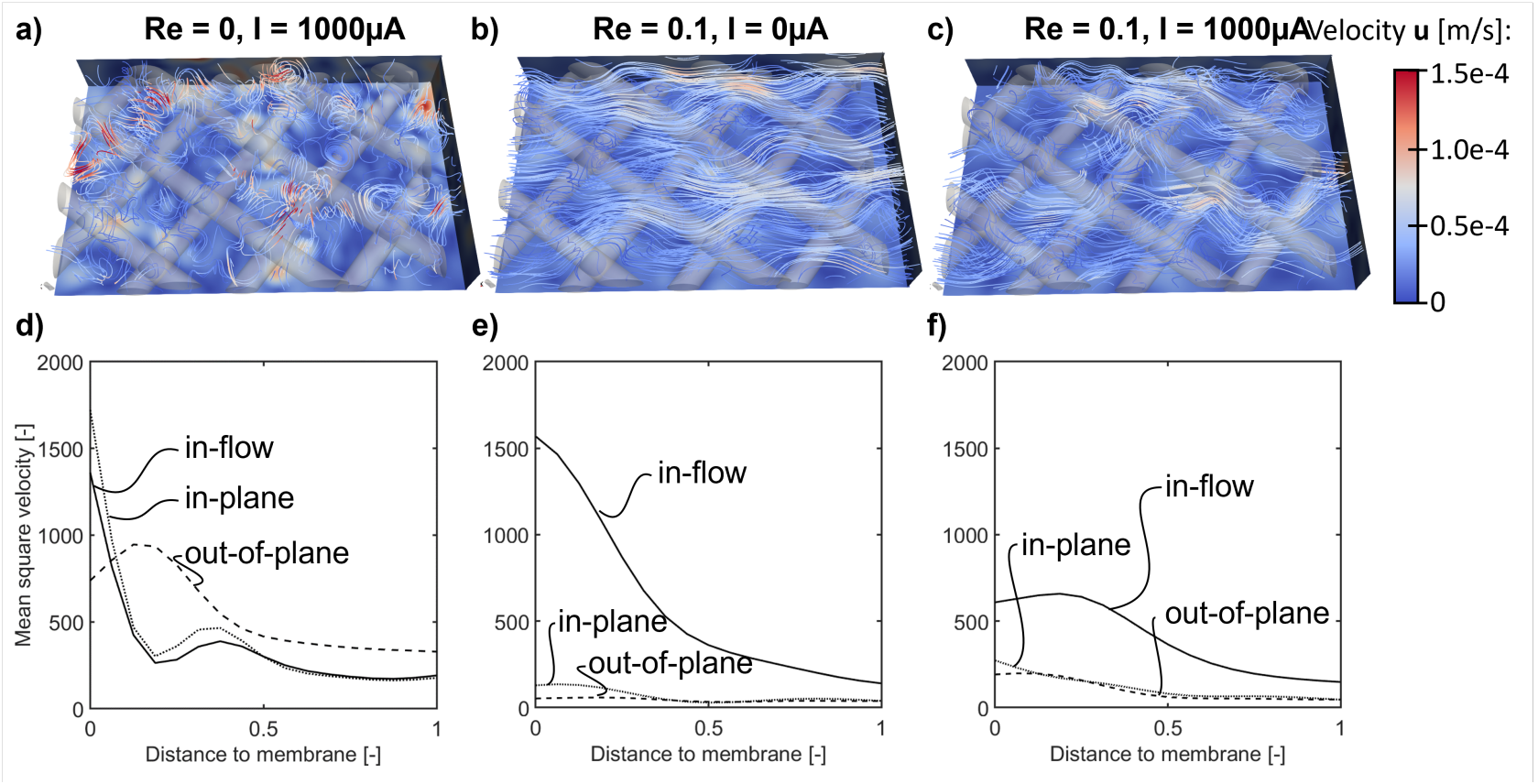

Figure 5.8: Flow field and velocity profiles of electroconvection and forced flow under influence of a commercial spacer. The flow field is shown as streamlines colored by the magnitude of the absolute velocity from blue to red. **a)** and **d)** show the reference at Re = 0 and 1000 μA. **b)** and **e)** show the experiment with forced flow at Re = 0.1 and 0 μA. **c)** and **f)** show the combined experiment at Re = 0.1 and 1000 μA.

their minima in the middle of the module.

There can be two explanations for the unbalanced velocity profiles. First, the streamlines and profiles indicate that the spacer sits more in the bottom half of the channel resulting in increased volume flow and velocity in the top half. Second, particles that pass under the structure are not detected, and their velocity information is lost.

Figure 5.8 **c)** depicts the streamlines resulting from the combined flow field of EC, forced flow, and spacer hydrodynamics. No distinct vortex rolls or rings emerge, but the previously regular flow profile is disrupted. The largest absolute velocities are still seen close to the top membrane. As seen before in Figure 5.6, the in-flow velocity shown in Figure 5.8 **f)** is smaller close to the desalinating membrane compared to both other cases increasing towards a maximum at 0.19 distance to the membrane. The superposition of the flow fields also leads to increased in-plane and out-of-plane velocities close to the top membrane.

The spacer structure still allows for the evolution of an EC vortex field but constrains the vortex dimensions and shape. In superposition with forced flow at a low Reynolds number, the effect of EC is still visible in the streamlines as well as the velocity profiles.

The effect of increasing Reynolds numbers of Re = 1 and Re = 8 is depicted in Figure 5.9. Contrary to the experiments without spacer, only little disturbances can be observed in the streamlines, see Figure 5.9 **a)** and **b)**.

The velocity components in Figure 5.9 **c)** and **d)** show profiles that are similar to the profile at Re = 0.1 as seen in Figure 5.8 **e)** but with larger overall magnitudes with increasing Reynolds number. The impact of EC is also only slightly visible in the in-plane and out-of-plane velocity components.

These results further strengthen the implication that the increasing Reynolds number suppresses the impact of EC on the velocity field. The in-

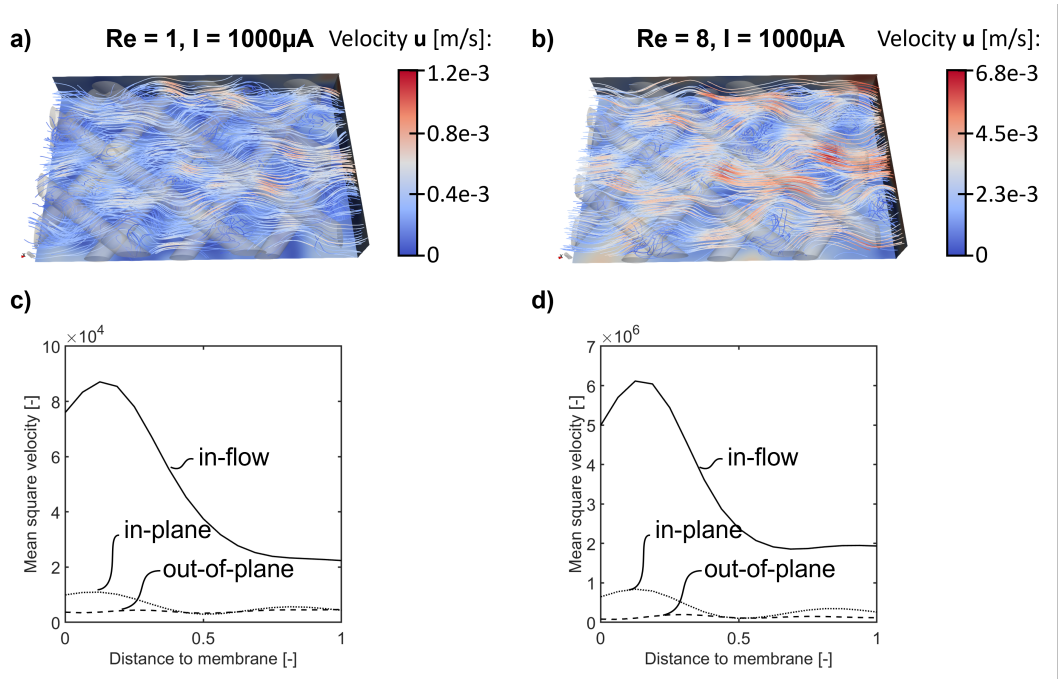

Figure 5.9: Flow field and velocity profiles of electroconvection with increasing forced flow under influence of a commercial spacer. The flow field is shown as streamlines colored by the magnitude of the absolute velocity from blue to red. **a)** and **c)** show the experiment with forced flow at Re = 1 and 1000 µA. **b)** and **d)** show the experiment with forced flow at Re = 8 and 1000 µA.

serted spacer adds additional shear, further restricting the possible height of the EC vortices. As suggested in the previous section, quantification of the influence of EC in the decreasing boundary layer close to the desalinating membrane is only possible with smaller particles at a larger magnification.

5.4 Conclusions

This chapter describes a newly designed electrochemical module that allows recording of the 3D electroconvective velocity field with forced flow and inserted spacer structures. The module's validation against the conventional module design used in this thesis shows good agreement in the vortex field structure and the velocity profiles. However, the vortex rotation is inverted, which needs further investigation. This change could originate

from heterogeneity in the membrane surface due to the casting without affecting the vortex strength.

Despite this difference, we could quantify the superposition of the electroconvective and forced flow profiles with and without an inserted spacer. Overall, the superposition leads to decreased velocities. The forced flow profile seems to disrupt the vortex structure of electroconvection at increasing Reynolds numbers. At Re > 0.1, the influence of electroconvection on the flow profiles vanishes. Analysis of the remaining effect close to the desalinating membrane demands higher magnification and smaller tracer particles. Currently used, commercially available particles strongly interact with the membrane's surface charge, preventing them from reaching close to the surface. This challenge can be overcome by newly synthesized particles with adjustable surface charge, e.g. fluorescent-labeled microgels.

In the future, the proposed method enables us to investigate the changes in flow profile introduced by a patterned membrane which was already analyzed in the case of a steady electrolyte in Chapter 4. The same ink-jet technique is suitable to pattern the Nafion-cast glass. Additionally, the combination of surface patterning and tailor-made spacers offers the possibility of a fully optimized flow field. Small changes in the cell's design could also expand its use to study flow or concentration phenomena in channels adjacent to a gas-diffusion electrode (GDE) or a single compartment of a flow-capacitive deionization (FCDI) cell. In both cases, the bottom Nafion-cast glass slide would be replaced by either a GDE or a conventional electrode.

6

Summary and outlook

Parts of this chapter have been published as:
Felix Stockmeier, Michael Schatz, Malte Habermann, John Linkhorst, Ali Mani, and Matthias Wessling, "Direct 3D observation and unraveling of electroconvection phenomena during concentration polarization at ion-exchange membranes", *Journal of Membrane Science*, 2021
DOI: 10.1016/j.memsci.2021.119846

Parts of this chapter are submitted as:
Felix Stockmeier, Daniel Felder, Steffen Eser, Malte Habermann, Petar Perić, Stephan Musholt, Katharina Albert, John Linkhorst, and Matthias Wessling, "Localized Electroconvection at Ion-Exchange Membranes with Heterogeneous Surface Charge", *Under Review in Nature Materials*, 2021
Preprint available at Research Square as DOI: 10.21203/rs.3.rs-1093972/v1

Parts of this chapter are in preparation for publication:
Felix Stockmeier, Lucas Stüwe, Elizaveta Evdochenko, Niklas Köller, Sebastian Brosch, Christian Kneppeck, Stephan Musholt, Katharina Albert, John Linkhorst, and Matthias Wessling, "Interaction Between Spacer-Altered Bulk Hydrodynamics and Electroconvection", *Journal to be decided*

6.1 Thesis summary

This thesis was devoted to the detailed exploration and manipulation of the 3D velocity field that arises in the overlimiting current (OLC) regime in electrically-driven membrane processes. The OLC region describes the renewed increase in current density with increasing potential after a diffusion-limited plateau region. The diffusion limitation is overcome to a large degree by the additional ion supply close to the membrane due to convective mixing. A hydrodynamic phenomenon, the so-called electroconvection, mixes the diffusion boundary layer and transports ion-rich bulk electrolyte to the membrane. This work is centered around the effects of electroconvection close to a cation-exchange membrane (CEM) since recent studies indicated that the share of water splitting to the OLC through CEMs is negligible, see Chapter 1, which allows for an unobstructed view. Experimental quantification of these chaotic flow patterns has so far only been carried out in 2D. Numerical direct simulations suggest 3D features, yet the experimental proof is lacking.

To close this gap, this thesis presented a comprehensive experimental method for the time-resolved recording and quantification of the 3D electroconvective velocity field near a CEM using micro particle tracking velocimetry (µPTV) described in Chapter 2. With this setup, we quantified the velocity field of electroconvection from build-up towards steady-state at multiples of the overlimiting current density, see Chapter 3. In contrast to simulations, the experiments covered length and time scales typical for industrial applications. We visualized coherent vortex structures and revealed the changes in the velocity field and its statistics with increasing current density. Additionally, the proposed method enabled the evaluation of the rotational direction of the vortex structures.

Furthermore, the diffusion limitation in the plateau region can be overcome by membrane surface modifications that effectively trigger a hydrodynamic instability called electroconvection. One proposed modification method that has shown promising process improvements is the precise surface patterning of membranes with microgel suspensions introducing a

regular surface charge inhomogeneity. However, the influence of the modification on the formation of electroconvection is still unknown.

Therefore, the setup was used to investigate the impact of membrane surface modifications on the electroconvective vortex field's build-up and its steady-state, see Chapter 4. The modification method increases the limiting current density and shortens the plateau. 2D direct numerical simulations supported the experimental approach. The results revealed the vortex field structure, its rotational direction, and the structural stability in steady-state for membranes modified with two types of microgels varying in zeta potential compared to a bare membrane.

Lastly, the interaction of EC with the hydrodynamics in a spacer-filled electrolyte channel was quantified for the evaluation of the OLC as a process regime in industrial processes, see Chapter 5. We first validated a new module design suitable for µPTV recordings of the pumped electrolyte. The results showed the suppressing effect of forced flow on the electroconvective vortices, which got more significant with increasing Reynolds number and the insertion of a spacer.

6.1.1 3D velocity field and statistics of electroconvection

Chapter 3 reported the transition of EC, which is characterized by changes in the rotational direction, mean square velocity, and temporal energy spectrum with only minor influence on the spatial spectrum. These findings indicated a more significant impact of EC's structural change on the mean square velocities and temporal spectra than on the spatial spectra. This knowledge is a prerequisite for engineering ion-selective surfaces that will extend the operation range of electrically driven processes beyond the diffusion-limited Nernst regime.

All in all, the developed technique enabled the first time-resolved quantification of EC's 3D velocity field even at significant overlimiting currents in industry-relevant dimensions and time spans. The velocity data further clarified the vortex structure, its rotational direction, and the velocity statistics.

The connection between the apparent transition of EC's vortex structure and resulting velocity statistics during build-up and increasing current density still needs further investigation. The additional use of 3D DNSs, which offer increased resolution close to the membrane, could provide definite answers. Other influences on the vortex field and its statistics like competitive ion transport [Rogh2020] or temperature gradients [Benn2018c; Benn2018d] are still vastly unexplored.

6.1.2 Membrane modification for enhanced electroconvection

Electrically-driven membrane processes suffer from increasing resistances during operation resulting in a process limitation at high current densities. This limitation can be overcome by membrane surface modifications that effectively trigger electroconvection. One proposed modification method that has shown promising process improvements is the precise surface patterning of membranes with microgel suspensions introducing a regular surface charge inhomogeneity [Rogh2019]. However, the influence of the modification on the formation and hydrodynamics of electroconvection is still unclear.

We investigated the impact of such surface modifications on the electroconvective vortex field's build-up using a combination of simulative and experimental techniques, namely 2D direct numerical simulations and 3D particle tracking velocimetry. This thesis reported the vortex field structure, rotational direction, and the structural stability of EC in steady-state.

We showed that the microgel with a significant difference in zeta potential to the membrane material structures the vortex field and dictates its rotational direction. Although no long-term structure was maintained, the vortex field still differed from the case of a bare membrane. Additionally, this modification offered complete control of the electroconvective vortex field during its build-up. These results emphasized the potential of specifically engineered membrane surfaces for overcoming the limitation of electrically

driven membrane processes.

Our experiments at increasing current densities revealed a challenge this modification introduces. Here, an intensive scaling of the membranes could be observed. We ascribe the appearance of scaling to the bi-polar character of the patches. Similar to bipolar membranes, which are anion- and cation-exchange membranes fused together, the positively charged patches lead to a large electric field gradient between themselves and the negatively charged membrane. This environment promotes water dissociation, which is enhanced with increasing potential. As explained in Chapter 4, an increased amount of $\mathrm{OH^-}$ results in the formation of CuO or $\mathrm{Cu(OH)_2}$, which form a crystalline scaling on the membrane.

All in all, despite the appearance of scaling the benefits of this modification method show potential for industrial application. Roghmans et al. [Rogh2019] reported the beneficial effect of the patterns for experiments at around 1 to 2 $\cdot$ i_{lim} without observing changes in pH or scaling. Consistent with their observation, the experiments reported in this thesis did not show enhanced scaling for current densities below about 6 $\cdot$ i_{lim}. The increased current density and a resulting reduction in membrane area up to this current density would still benefit industrial application.

6.1.3 Electroconvection in application-oriented devices

In the past, only minor attention was paid to the use of the overlimiting current region as a process regime at an industrial scale. The leading concerns revolved around water splitting being solely the driver in this region. This view changed only recently, accompanied by a rapid increase in interest. Especially understanding the interaction of EC with water splitting and the hydrodynamics introduced by spacers is crucial for application-oriented devices.

Therefore, we designed a novel electrochemical module that allowed to record the 3D electroconvective velocity field with forced flow and inserted spacer structures. We validated the module against the convectional module design used in Chapter 3 and Chapter 4 of this thesis. The vortex field

structure and velocity profiles showed good agreement. However, the vortex rotational directions were directed in opposite directions which needs further investigation.

Despite this difference, we could quantify the superposition of the electroconvective and forced flow profiles at a low Reynolds number with and without an inserted spacer for the first time. Overall, the superposition led to decreased velocities. The forced flow profile seemed to disrupt the vortex structure of electroconvection. With increasing Reynolds number, the flow profile of electroconvection got further suppressed. Analysis of the remaining effect close to the desalinating membrane demands higher magnification and smaller tracer particles. Currently used, commercially available particles strongly interact with the membrane's surface charge, preventing them from reaching close to the surface. This challenge can be overcome by newly synthesized particles with an adjustable surface charge.

The newly generated insights would facilitate the design of spacers that allow the use of overlimiting current densities and the benefits of EC in industrial processes at typical Reynolds numbers.

6.2 Outlook

This thesis took a significant step towards the physical understanding and manipulation of electroconvection in application-oriented devices. Although, there are still some questions and challenges remaining concerning its use in industrial processes. Improved experimental and numerical methods could provide answers to some of these questions.

6.2.1 Overcoming constraints of experiments

In our experiments, the tracer's zeta potential limits the measurement of velocities close to the membrane. Therefore, tracer particles with close to neutral zeta potential, a diameter of about 1 µm to 3 µm, and a density close to that of water would enable the resolution of the velocity statistics close

to the membrane-fluid interface where the vortex-generating body force is located [Mani2020]. Knowledge of the 3D velocity field in this region would offer a better understanding of the generation of EC and its interaction with complex superimposed hydrodynamics.

Microgels offer these specific chemical and physical properties. They are loose polymeric structures with a high water content. Additionally, their zeta potential can be tailored by functionalization with differently charged monomers [Agra2018]. This way, microgels can even be made with a pH or temperature-sensitive size and zeta potential. Recent advances in their synthesis methods even overcome the size gap between 1 µm and 5 µm which is the relevant size for application as tracer particles in our system [Ksia2020]. Especially the exploration of the small-scale influence of the membrane surface modification discussed in Chapter 4 would benefit from the use of such novel tracer particles.

Another limitation poses the electrochemical cell's design. A diverse series of trial experiments with varying cell designs and configurations suggest key features that need to be fulfilled to measure 3D EC using µPTV. The most important design features include:

- Optical accessibility
- At least two electrodes and one membrane
- An aspect ratio larger than 2π
- A channel depth smaller than 1 mm for full vortex resolution with our µPTV setup

In Chapter 3 and 4, the used cell design comprises a copper cathode with a circular hole to ensure optical access. This electrode was one-sidedly sealed by gluing a microscope glass slide on top. This approach was previously compared to an ITO-coated glass electrode. Both showed similar performance. However, the ITO quickly corroded during experiments. Therefore, the other option was preferred.

For further studies, we recommend advancing the approach described in Chapter 5 which is based on Kang et al. [Kang2020] but uses Nafion-coated glass instead of Nafion N117 Membranes. The use of Nafion-coated glass results in well-defined, transparent, and rigid ion bridges. These ion bridges enable the delocalization of the electrodes and their reactions from the electrolyte channels. Therefore, the cell design is greatly simplified. However, the implementation of an electrolyte channel between two cation-exchange membranes still lacks comparability to application-oriented set-ups. An electrolyte channel between an anion- and cation-exchange membranes is needed to get closer to industrial electrodialysis conditions. Such a design could be accomplished by exchanging one of the Nafion-coated glass slides with an anion-exchange membrane. This anion-exchange membrane also needs to be fixed onto a glass slide. One possibility could be the use of a novel hydrogel-based homogeneous anion-exchange membrane [Chua2020].

This cell design could also be tuned for the optical analysis of processes in the slurry-electrode of flow-capacitive deionization (FCDI) channels or in the electrolyte close to gas-diffusion electrodes (GDEs). In the first case, one Nafion-coated glass slide could be exchanged for a planar metal electrode that interacts with the slurry. In the second case, the glass slide could be exchanged for a GDE which would also require implementing a gas channel beneath.

6.2.2 Overcoming constrains of simulations

The simulation of electroconvective flow, especially in 3D, poses a considerable challenge due to its computational demand [Mani2020]. Therefore, simplifying assumptions are needed to achieve acceptable run times. These limitations also influenced our numerical approach reported in Chapter 4.

Patch simulations

The simulations reported in Chapter 4 were carried out to supplement the experimental evaluation of velocities with data of concentration and electric field gradients. The results, while in good qualitative accordance, did not reflect the significant quantitative impact seen in the experiments of Roghmans et al. [Rogh2019]. These differences could result from the large discrepancy in the Debye length between experiment and simulation as also elaborated in Chapter 3 and by Mani and Wang [Mani2020]. Additionally, the patches are only implemented as heterogeneity in zeta potential. However, experiments and simulations indicate that the influence is more complex. A combination of the proposed volume charge method with conductivity heterogeneity used in Davidson et al. [Davi2016] leading to an even stronger deflection of the electric field lines and changes in hydrophobicity reducing energy loss due to friction as in Nebavskaya et al. [Neba2017] could lead to the experimentally observed effects [Rogh2019].

Another approach pursued during the thesis was using patches with inhomogeneous charge in terms of a programmed boundary condition. We used different continuous functions like a sinusoidal distribution with varying frequencies to mimic non-uniform patches. However, the results show only insignificant differences.

The study of Druzgalski and Mani [Druz2016] also motivated the step to 3D DNS modeling of different patch geometries seen in Figure 6.1 **a)**. The governing equations and boundary conditions equal the ones of the 2D DNSs described in Chapter 4 with the addition of a third spatial dimension. However, the significantly increased computational demand only allowed for coarse spatial and temporal resolution and simulation of short periods in a small geometry. Still, similarities with the 2D DNSs and experiments can be seen. The build-up of the EC vortex structure in a domain with a stripe type patch, see Figure 6.1 **b)**, indicates orientation at the patch borders. Also, a difference in the positioning of the longitudinal vortex rolls between the positive and negative charge case can be seen. Chapter 4 revealed

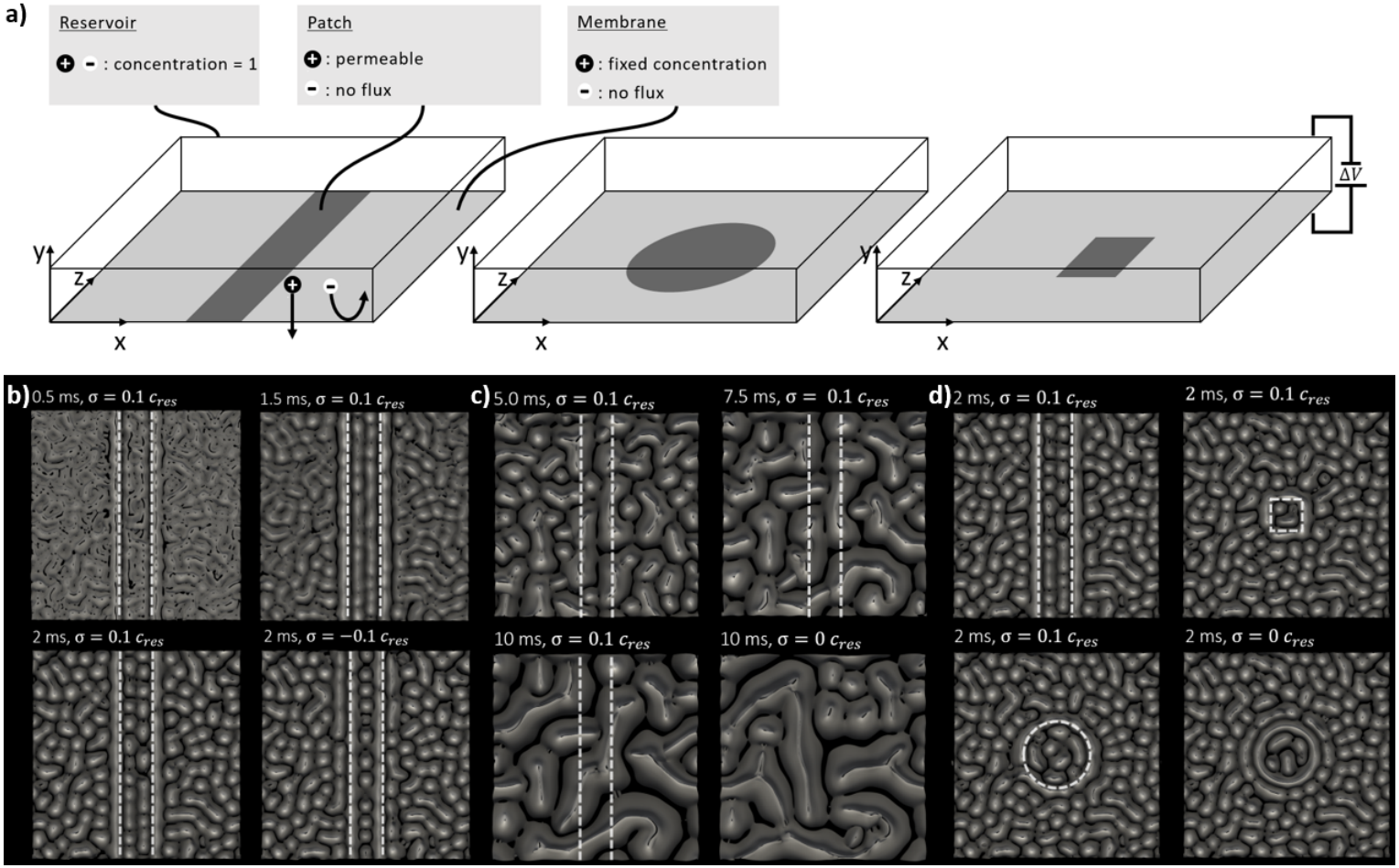

Figure 6.1: 3D DNS domain and results for differently shaped patches at a potential difference of 30 V_t a) Domain and boundary conditions of the 3D direct numerical simulations. The domain has a square base shape between a mixed reservoir, an ideal cation-exchange membrane, and four periodic boundaries. The three illustrations show the stripe, circle, and square type patches. **b)** Development of the vortex field in case of a square patch with positive charge between 0.5 ms and 2 ms, and comparison to the negative charge case at 2 ms. **c)** Further development of the vortex field between 5 ms and 10 ms, and comparison to the neutral charge case at 10 ms. **d)** Comparison of the vortex field between all patch types with a positive charge and the neutral charge case at 2 ms. In **a)**, **b)**, and **c)**, coherent vortex structures are plotted as isosurfaces with grayscale coloring for visual guidance. The white dotted lines indicate patch borders.

that, while 2D DNSs predict long-term stability of the vortex field at patches, the stabilizing effect was not confirmed in the experiments. The same result is obtained in 3D DNSs. Figure 6.1 **c)** shows the Development of the vortex field at the stripe type patch between 5 ms to 10 ms. The strict orientation seen in Figure 6.1 **b)** is already disturbed at 5 ms and completely lost at 10 ms. In the last shown time step, the vortex field also slightly differs from the case without a patch. Figure 6.1 **d)** shows a comparison of the vortex field structures of all simulated cases with a positive charge and the neutral charge case at 2 ms. All patches lead to a structuring of the vortex field at their borders. However, the neutral charge case also results in a structure similar to the circular patch case. This unexpected shape of the vortex field could indicate inaccurate time and space resolution, resulting in feedback over the periodic boundary conditions. Therefore, the results are valid to only a limited degree.

In the future, 3D DNSs of a patterned membrane with acceptable spatial and temporal resolution could shed light on the stability difference between 2D and 3D. However, the boundary of the great computational demand of 3D DNSs for detailed EC parameter studies needs to be overcome. The implementation of a model with statistically averaged equations could essentially reduce computational effort.

Statistical averaged equation

Druzgalski et al. [Druz2013; Druz2016] described a set of statistically averaged Navier-Stokes, Nernst-Planck, and Poisson equations with three unclosed terms. They calculated these terms based on their DNS data. However, the resulting values always only correspond to the specific calculated case. To formulate a fully closed set of equations, additional equations that predict the unclosed terms are inherently needed. Such equations could be derived from and validated with the velocity statistics presented in this work. A promising technique is the so-called inverse macroscopic forcing method (IMFM), which acts as a numerical rheometer measuring the eddy diffusivity operator [Mani2021]. A combination of IMFM with our experi-

mental velocity data will allow the fast determination of the zeroth moment of the eddy diffusivity kernel used as a sufficient closure for the dominant, fluctuating advection term [Druz2013; Druz2016].

As the unclosed terms depend on a fluctuating velocity component, the extension of the experimental analysis to the fluctuating cation and anion concentrations would complete the statistical picture of electroconvection (EC). Current studies only qualitatively investigate the temporal and spatial evolution of concentrations during EC with low temporal resolution. Advances in developing methods capable of analyzing concentration gradients with high temporal and 3D spatial resolution would close this gap.

6.2.3 Implications for industrial use of overlimiting currents

The use of overlimiting currents (OLCs) in industrial-scale applications is avoided mainly because of two challenges: First, the increased energy demand in the OLC region [Lee2002] and, second, the occurrence of intense water splitting, especially at anion-exchange membranes [Niko2014]. However, multiple studies are highlighting the benefits of the OLC. For example, Beaulieu et al. [Beau2020] reported an increase in water splitting but also in ion recovery and a decrease of scaling in a lab-scale electrodialysis process.

In this thesis, we provided the first insight into the hydrodynamics of the 3D electroconvective vortex field. The statistical analysis of our results in Chapter 3 could lead to the development of a fully closed set of statistically averaged equations. Such equations could be used to run simulations including EC on a membrane module scale allowing for macroscopic optimization for OLCs.

The insights on the hydrodynamic influence of membrane surface modifications in Chapter 4 should be expanded and optimized on a larger scale. Roghmans et al. [Rogh2019] already proved their effectiveness for reducing the plateau length and increasing the limiting current density of an electro-

dialysis process. Both effects reduce the energy demand of OLCs. Further, improvement of membrane surface modification methods could lead to a complete vanishing of the plateau region.

Processes utilizing such membranes would be profitable in the OLC region if the investment cost reduction of a smaller needed membrane area exceeds the increased energy cost. Additionally, the vanishing of the plateau region would also counteract the challenge of water splitting. Processes could be optimized to run at low enough potentials to avoid extended water splitting while still being in the OLC region. The reachable current densities will directly correlate with further advances in the preparation of ion-exchange membrane materials that do not catalyze water splitting.

In Chapter 5, we give first insights on the interaction of the flow field in spacer-filled channels with electroconvection. Although we identify a range of Reynolds numbers where electroconvection is measurable, the additional relation between EC and water splitting still needs further clarification. Additionally, specific spacer designs either decrease or increase the size of the stagnant boundary layer. Both cases are reported to enhance EC in small-scale devices [Kim2017; Kim2021]. Balster, Stamatialis, and Wessling [Bals2010] also reported that ion-conductive spacers further increase the current density by allowing EC to develope at the spacer itself. Furthermore, the combination of patterned membranes, which were analyzed in Chapter 4, with forced flow and tailored spacer structures could enable mixing of the complete flow channel.

As a last step, the scale-up of these concepts to larger modules, higher flow velocities and larger overlimiting currents will validate their usability in industry-scale processes.

6.2.4 Further applications of electroconvection

Adequate mixing of fluids in microfluidic applications proves to be a continuous challenge due to the low Reynolds numbers achieved in microfluidic channels [Lee2018]. Micromixers based on electrokinetic energy input offer high energy efficiencies, controllability, and robustness [Huo2020]. In

these types of mixers, a key is the localized inducing of electroconvective (EC) vortices e.g. at electrodes [Zhan2018] or nanochannels [Chiu2013; Liu2020].

The cell described in Chapter 5 offers an easy to assemble design where EC can be locally triggered at the channel walls. In combination with the insights of Chapter 4, control of the shape of EC could be achieved by tuning the material surface properties with surface modifications like microgel patterning. With this technique, even switchability of the EC vortex positions is possible if external triggers like pH or temperature adjust the pattern's properties.

Recent studies also describe vastly unexplored conditions for the evolution of EC, for example, during electrolysis [Pand2021] and even through a macroporous membrane [Lee2021]. These novel insights open up new potential uses of EC.

All in all, electroconvection offers improvement for established processes, but also a wide range of new applications in manifold fields of research. This thesis contributes important knowledge on the 3D EC vortex field, its velocity statics, and the interaction with membrane surface modifications, forced-flow, and spacer hydrodynamics. The developed quantification methods will be useful to also analyze more complex settings and applications. Our efforts bring us one step closer not only to reduce the costs of desalination but also to solve the global water scarcity problem.

Bibliography

[Abdu2014] S. Abdu, M.-C. Martí-Calatayud, J. E. Wong, M. García-Gabaldón, and M. Wessling. “Layer-by-layer modification of cation exchange membranes controls ion selectivity and water splitting”. *ACS applied materials & interfaces* 6.3 (2014) 1843–1854. DOI: 10.1021/am4048317 (cit. on pp. 17, 75).

[Abu-2016] R. Abu-Rjal, I. Rubinstein, and B. Zaltzman. “Driving factors of electro-convective instability in concentration polarization”. *Physical Review Fluids* 1.2 (2016) 135. DOI: 10.1103/PhysRevFluids.1.023601 (cit. on p. 14).

[Agra2018] G. Agrawal and R. Agrawal. “Stimuli-Responsive Microgels and Microgel-Based Systems: Advances in the Exploitation of Microgel Colloidal Properties and Their Interfacial Activity”. *Polymers* 10.4 (2018) DOI: 10.3390/polym10040418 (cit. on p. 129).

[Ali2018] A. Ali, R. A. Tufa, F. Macedonio, E. Curcio, and E. Drioli. “Membrane technology in renewable-energy-driven desalination”. *Renewable and Sustainable Energy Reviews* 81.9 (2018) 1–21. DOI: 10.1016/j.rser.2017.07.047 (cit. on p. 3).

[Alot2014] P. Alotto, M. Guarnieri, and F. Moro. “Redox flow batteries for the storage of renewable energy: A review”. *Renewable and Sustainable Energy Reviews* 29 (2014) 325–335. DOI: 10.1016/j.rser.2013.08.001 (cit. on p. 6).

[Bals2007a] J. Balster, M. H. Yildirim, D. F. Stamatialis, R. Ibanez, R. G. H. Lammertink, V. Jordan, and M. Wessling. “Morphology and microtopology of cation-exchange polymers and the origin of the overlimiting current”. *The journal of physical chemistry. B* 111.9 (2007) 2152–2165. DOI: 10.1021/jp068474t (cit. on pp. 17, 18, 70, 75).

[Bals2007b] J. Balster, M. H. Yildirim, D. F. Stamatialis, R. Ibanez, R. G. H. Lammertink, V. Jordan, and M. Wessling. “Morphology and microtopology of cation-exchange polymers and the origin of the overlimiting current”. *Journal of Physical Chemistry B* 111.9 (2007) 2152–2165. DOI: 10.1021/jp068474t (cit. on p. 47).

[Bals2010] J. Balster, D. F. Stamatialis, and M. Wessling. “Membrane with integrated spacer”. *Journal of Membrane Science* 360.1-2 (2010) 185–189. DOI: 10.1016/j.memsci.2010.05.011 (cit. on pp. 17, 22, 135).

[Barb2014] A. C. Barbati and B. J. Kirby. “Electrokinetic measurements of thin Nafion films”. *Langmuir : the ACS journal of surfaces and colloids* 30.8 (2014) 1985–1993. DOI: 10.1021/la403735g (cit. on p. 82).

[Bard2000] A. J. Bard and L. R. Faulkner. *Electrochemical Methods: Fundamentals and Applications*. 2nd Edition. [s.l.]: John Wiley & Sons Inc, 2000 (cit. on p. 37).

[Baza2009] M. Z. Bazant, M. S. Kilic, B. D. Storey, and A. Ajdari. “Towards an understanding of induced-charge electrokinetics at large applied voltages in concentrated solutions”. *Advances in colloid and inter-*

face science 152.1-2 (2009) 48–88. DOI: 10.1016/j.cis.2009.10.001 (cit. on pp. 9, 11).

[Bazi2020] L. Bazinet and T. R. Geoffroy. “Electrodialytic Processes: Market Overview, Membrane Phenomena, Recent Developments and Sustainable Strategies”. *Membranes* 10.9 (2020) DOI: 10.3390/membranes10090221 (cit. on p. 4).

[Beau2020] M. Beaulieu, V. Perreault, S. Mikhaylin, and L. Bazinet. “How Overlimiting Current Condition Influences Lactic Acid Recovery and Demineralization by Electrodialysis with Nanofiltration Membrane: Comparison with Conventional Electrodialysis”. *Membranes* 10.6 (2020) DOI: 10.3390/membranes10060113 (cit. on p. 134).

[Belf1972] G. Belfort and G. A. Guter. “An experimental study of electrodialysis hydrodynamics”. *Desalination* 10.3 (1972) 221–262. DOI: 10.1016/S0011-9164(00)82001-9 (cit. on p. 22).

[Bell2019] T. Belloň, P. Polezhaev, L. Vobecká, M. Svoboda, and Z. Slouka. “Experimental observation of phenomena developing on ion-exchange systems during current-voltage curve measurement”. *Journal of Membrane Science* 572 (2019) 607–618. DOI: 10.1016/j.memsci.2018.11.037 (cit. on p. 49).

[Bell2022] T. Belloň and Z. Slouka. “Overlimiting convection at a heterogeneous cation-exchange membrane studied by particle image velocimetry”. *Journal of Membrane Science* 643.3 (2022) 120048. DOI: 10.1016/j.memsci.2021.120048 (cit. on p. 75).

[Belo2006] E. Belova, G. Lopatkova, N. D. Pismenskaya, V. Nikonenko, and C. Larchet. “Role of water splitting in development of electroconvection in ion-exchange membrane systems”. *Desalination* 199.1-3 (2006) 59–61. DOI: 10.1016/j.desal.2006.03.142 (cit. on pp. 74, 105).

[Benn2016] A. M. Benneker, J. A. Wood, P. A. Tsai, and R. G. H. Lammertink. “Observation and experimental investigation of confinement effects on ion transport and electrokinetic flows at the microscale”. *Scientific reports* 6 (2016) 37236. DOI: 10.1038/srep37236 (cit. on p. 18).

[Benn2018a] A. M. Benneker. *From small to big: Ion transport at interfaces*. 2018. DOI: 10.3990/1.9789036544924 (cit. on pp. 17, 75).

[Benn2018b] A. M. Benneker, B. Gumuscu, E. G. H. Derckx, R. G. H. Lammertink, J. C. T. Eijkel, and J. A. Wood. “Enhanced ion transport using geometrically structured charge selective interfaces”. *Lab on a chip* 18.11 (2018) 1652–1660. DOI: 10.1039/c7lc01220a (cit. on p. 70).

[Benn2018c] A. M. Benneker, J. Klomp, R. G. Lammertink, and J. A. Wood. “Influence of temperature gradients on mono- and divalent ion transport in electrodialysis at limiting currents”. *Desalination* 443 (2018) 62–69. DOI: 10.1016/j.desal.2018.05.005 (cit. on p. 126).

[Benn2018d] A. M. Benneker, T. Rijnaarts, R. G. Lammertink, and J. A. Wood. “Effect of temperature gradients in (reverse) electrodialysis in the

Ohmic regime". *Journal of Membrane Science* 548 (2018) 421–428. DOI: 10.1016/j.memsci.2017.11.029 (cit. on pp. 16, 126).

[Bidd2004] E. Biddiss, D. Erickson, and D. Li. "Heterogeneous surface charge enhanced micromixing for electrokinetic flows". *Analytical chemistry* 76.11 (2004) 3208–3213. DOI: 10.1021/ac035451r (cit. on p. 17).

[Burm2011] A. Burmistrova, M. Richter, M. Eisele, C. Üzüm, and R. von Klitzing. "The Effect of Co-Monomer Content on the Swelling/Shrinking and Mechanical Behaviour of Individually Adsorbed PNIPAM Microgel Particles". *Polymers* 3.4 (2011) 1575–1590. DOI: 10.3390/polym3041575 (cit. on p. 82).

[Buty2020] D. Butylskii, I. Moroz, K. Tsygurina, and S. Mareev. "Effect of Surface Inhomogeneity of Ion-Exchange Membranes on the Mass Transfer Efficiency in Pulsed Electric Field Modes". *Membranes* 10.3 (2020) DOI: 10.3390/membranes10030040 (cit. on p. 17).

[Camp2018] A. Campione, L. Gurreri, M. Ciofalo, G. Micale, A. Tamburini, and A. Cipollina. "Electrodialysis for water desalination: A critical assessment of recent developments on process fundamentals, models and applications". *Desalination* 434 (2018) 121–160. DOI: 10.1016/j.desal.2017.12.044 (cit. on p. 17).

[Chan2010] J.-H. Chang, A. V. Ellis, C.-H. Tung, and W.-C. Huang. "Copper cation transport and scaling of ionic exchange membranes using electrodialysis under electroconvection conditions". *Journal of*

Membrane Science 361.1-2 (2010) 56–62. DOI: 10.1016/j.memsci.2010.06.012 (cit. on pp. 52, 102).

[Chiu2013] P.-H. Chiu, C.-C. Chang, and R.-J. Yang. “Electrokinetic micromixing of charged and non-charged samples near nano–microchannel junction”. *Microfluidics and Nanofluidics* 14.5 (2013) 839–844. DOI: 10.1007/s10404-012-1116-2 (cit. on p. 136).

[Choi2001] J.-H. Choi, S.-H. Kim, and S.-H. Moon. “Heterogeneity of Ion-Exchange Membranes: The Effects of Membrane Heterogeneity on Transport Properties”. *Journal of Colloid and Interface Science* 241.1 (2001) 120–126. DOI: 10.1006/jcis.2001.7710 (cit. on pp. 17, 75).

[Chua2020] J.-N. Chuang, P.-Y. Diao, W.-S. Huang, L.-F. Huang, S. Senapati, H.-C. Chang, and Y.-M. Sun. “Novel Homogeneous Anion Exchange Membranes for Reproducible and Sensitive Nucleic Acid Detection via Current-Voltage Characteristic Measurement”. *ACS applied materials & interfaces* 12.49 (2020) 54459–54472. DOI: 10.1021/acsami.0c17180 (cit. on p. 130).

[Cowa1959] D. A. Cowan and J. H. Brown. “Effect of Turbulence on Limiting Current in Electrodialysis Cells”. *Industrial & Engineering Chemistry* 51.12 (1959) 1445–1448. DOI: 10.1021/ie50600a026 (cit. on pp. 22, 105).

[Davi2016] S. M. Davidson, M. Wessling, and A. Mani. “On the Dynamical Regimes of Pattern-Accelerated Electroconvection”. *Scientific re-*

ports 6 (2016) 22505. DOI: 10.1038/srep22505 (cit. on pp. 17–19, 32, 55–57, 70, 75, 76, 78, 80, 90, 131).

[Deme2014] E. A. Demekhin, N. V. Nikitin, and V. S. Shelistov. "Three-dimensional coherent structures of electrokinetic instability". *Physical review. E, Statistical, nonlinear, and soft matter physics* 90.1 (2014) 013031. DOI: 10.1103/PhysRevE.90.013031 (cit. on pp. 16, 46, 49, 54, 57, 69, 87).

[Deng2013] D. Deng, E. V. Dydek, J.-H. Han, S. Schlumpberger, A. Mani, B. Zaltzman, and M. Z. Bazant. "Overlimiting current and shock electrodialysis in porous media". *Langmuir : the ACS journal of surfaces and colloids* 29.52 (2013) 16167–16177. DOI: 10.1021/la4040547 (cit. on p. 32).

[Dina2019] A. Dinar, A. Tieu, and H. Huynh. "Water scarcity impacts on global food production". *Global Food Security* 23.3 (2019) 212–226. DOI: 10.1016/j.gfs.2019.07.007 (cit. on p. 2).

[Djeh2019] L. A. Djehdian, C. M. Chini, L. Marston, M. Konar, and A. S. Stillwell. "Exposure of urban food–energy–water (FEW) systems to water scarcity". *Sustainable Cities and Society* 50.1 (2019) 101621. DOI: 10.1016/j.scs.2019.101621 (cit. on p. 2).

[Door2021] G. Doornbusch, M. van der Wal, M. Tedesco, J. Post, K. Nijmeijer, and Z. Borneman. "Multistage electrodialysis for desalination of natural seawater". *Desalination* 505 (2021) 114973. DOI: 10.1016/j.desal.2021.114973 (cit. on p. 3).

[Druz2013] C. L. Druzgalski, M. B. Andersen, and A. Mani. “Direct numerical simulation of electroconvective instability and hydrodynamic chaos near an ion-selective surface”. *Physics of Fluids* 25.11 (2013) 110804. DOI: 10.1063/1.4818995 (cit. on pp. 15, 39, 40, 42, 46, 49, 77, 79, 80, 133, 134).

[Druz2016] C. Druzgalski and A. Mani. “Statistical analysis of electroconvection near an ion-selective membrane in the highly chaotic regime”. *Physical Review Fluids* 1.7 (2016) DOI: 10.1103/PhysRevFluids.1.073601 (cit. on pp. 13, 16, 38, 41, 46, 49, 52, 53, 59–62, 65, 69, 70, 131, 133, 134).

[Dukh1991] S. S. Dukhin. “Electrokinetic phenomena of the second kind and their applications”. *Advances in colloid and interface science* 35 (1991) 173–196. DOI: 10.1016/0001-8686(91)80022-C (cit. on p. 13).

[Esse1986] O. M. Essenwanger. *Elements of statistical analysis*. Vol. / ed. by O. M. Essenwanger ; 1,B. World survey of climatology General climatology. Amsterdam: Elsevier, 1986 (cit. on p. 40).

[Fane2009] A. G. Fane. “Techniques to Enhance Performance of Membrane Processes”. In*Handbook of membrane separations*. 2009. 193–232. (Cit. on p. 55).

[Fimb2007] G. A. Fimbres-Weihs and D. E. Wiley. “Numerical study of mass transfer in three-dimensional spacer-filled narrow channels with

steady flow". *Journal of Membrane Science* 306.1-2 (2007) 228–243. DOI: 10.1016/j.memsci.2007.08.043 (cit. on pp. 21, 106).

[Fimb2010] G. A. Fimbres-Weihs and D. E. Wiley. "Review of 3D CFD modeling of flow and mass transfer in narrow spacer-filled channels in membrane modules". *Chemical Engineering and Processing: Process Intensification* 49.7 (2010) 759–781. DOI: 10.1016/j.cep.2010.01.007 (cit. on p. 21).

[Gend2014] Y. Gendel, A. K. E. Rommerskirchen, O. David, and M. Wessling. "Batch mode and continuous desalination of water using flowing carbon deionization (FCDI) technology". *Electrochemistry Communications* 46 (2014) 152–156. DOI: 10.1016/j.elecom.2014.06.004 (cit. on pp. 5, 46).

[Gil2018] V. Gil, M. Andreeva, L. Jansezian, J. Han, N. D. Pismenskaya, V. Nikonenko, C. Larchet, and L. Dammak. "Impact of heterogeneous cation-exchange membrane surface modification on chronopotentiometric and current–voltage characteristics in NaCl, CaCl2 and MgCl2 solutions". (2018) (cit. on pp. 17, 75).

[Gu2019] Z. Gu, B. Xu, P. Huo, S. M. Rubinstein, M. Z. Bazant, and D. Deng. "Deionization shock driven by electroconvection in a circular channel". *Physical Review Fluids* 4.11 (2019) DOI: 10.1103/PhysRevFluids.4.113701 (cit. on p. 32).

[Guan2020] Y. Guan, J. Riley, and I. Novosselov. “Three-dimensional electroconvective vortices in cross flow”. *Physical Review E* 101.3 (2020) 159. DOI: 10.1103/PhysRevE.101.033103 (cit. on pp. 20, 46, 105).

[Guan2021] Y. Guan, T. Yang, and J. Wu. “Mixing and transport enhancement in microchannels by electrokinetic flows with charged surface heterogeneity”. *Physics of Fluids* 33.4 (2021) 042006. DOI: 10.1063/5.0047181 (cit. on pp. 17, 75).

[Gude2017] V. G. Gude. “Desalination and water reuse to address global water scarcity”. *Reviews in Environmental Science and Bio/Technology* 16.4 (2017) 591–609. DOI: 10.1007/s11157-017-9449-7 (cit. on pp. 2, 3).

[Herp2008] S. Herpin, C. Y. Wong, M. Stanislas, and J. Soria. “Stereoscopic PIV measurements of a turbulent boundary layer with a large spatial dynamic range”. *Experiments in Fluids* 45.4 (2008) 745–763. DOI: 10.1007/s00348-008-0533-1 (cit. on pp. 62, 63, 67).

[Hill1956] T. L. Hill et al. “General discussion”. *Discuss. Faraday Soc.* 21.0 (1956) 117–140. DOI: 10.1039/DF9562100117 (cit. on p. 33).

[Hoek2014] A. Y. Hoekstra and T. O. Wiedmann. “Humanity’s unsustainable environmental footprint”. *Science (New York, N.Y.)* 344.6188 (2014) 1114–1117. DOI: 10.1126/science.1248365 (cit. on p. 2).

[Huo2020] X. Huo and X. Chen. “A review on modeling, simulation and experiment of electrokinetic micromixers”. *Journal of Dispersion Sci-*

ence and Technology (2020) 1–13. DOI: 10.1080/01932691.2020.1773847 (cit. on p. 135).

[Jeon1995] J. Jeong and F. Hussain. “On the identification of a vortex”. *Journal of Fluid Mechanics* 285.-1 (1995) 69. DOI: 10.1017/S0022112095000462 (cit. on pp. 38, 110).

[Jeon2018] Y. J. Jeon, J. Schneiders, M. Müller, D. Michaelis, and B. Wieneke. *4D flow field reconstruction from particle tracks by VIC+ with additional constraints and multigrid approximation*. 2018. DOI: 10.3929/ETHZ-B-000279199 (cit. on p. 38).

[Jone2019] E. Jones, M. Qadir, M. T. H. van Vliet, V. Smakhtin, and S.-M. Kang. “The state of desalination and brine production: A global outlook”. *The Science of the total environment* 657 (2019) 1343–1356. DOI: 10.1016/j.scitotenv.2018.12.076 (cit. on p. 3).

[Kang2020] S. Kang and R. Kwak. “Pattern Formation of Three-Dimensional Electroconvection on a Charge Selective Surface”. *Physical Review Letters* 124.15 (2020) 52. DOI: 10.1103/PhysRevLett.124.154502 (cit. on pp. 15, 49, 54, 69, 80, 87, 107, 130).

[Kara2015] E. Karatay, C. L. Druzgalski, and A. Mani. “Simulation of chaotic electrokinetic transport: performance of commercial software versus custom-built direct numerical simulation codes”. *Journal of Colloid and Interface Science* 446 (2015) 67–76. DOI: 10.1016/j.jcis.2014.12.081 (cit. on p. 80).

[Kara2016] E. Karatay, M. B. Andersen, M. Wessling, and A. Mani. “Coupling between Buoyancy Forces and Electroconvective Instability near Ion-Selective Surfaces”. *Physical review letters* 116.19 (2016) 194501. DOI: 10.1103/PhysRevLett.116.194501 (cit. on pp. 16, 32).

[Khai2011] A. S. Khair. “Concentration polarization and second-kind electrokinetic instability at an ion-selective surface admitting normal flow”. *Physics of Fluids* 23.7 (2011) 072003. DOI: 10.1063/1.3605693 (cit. on pp. 20, 106).

[Kim2007] S. J. Kim, Y.-C. Wang, J. H. Lee, H. Jang, and J. Han. “Concentration polarization and nonlinear electrokinetic flow near a nanofluidic channel”. *Physical review letters* 99.4 (2007) 044501. DOI: 10.1103/PhysRevLett.99.044501 (cit. on p. 13).

[Kim2011] Y. Kim, W. S. Walker, and D. F. Lawler. “Electrodialysis with spacers: Effects of variation and correlation of boundary layer thickness”. *Desalination* 274.1-3 (2011) 54–63. DOI: 10.1016/j.desal.2011.01.076 (cit. on p. 21).

[Kim2016] B. Kim, R. Kwak, H. J. Kwon, S. van Pham, M. Kim, B. Al-Anzi, G. Lim, and J. Han. “Purification of High Salinity Brine by Multi-Stage Ion Concentration Polarization Desalination”. *Scientific reports* 6 (2016) 31850. DOI: 10.1038/srep31850 (cit. on pp. 15, 49).

[Kim2017] B. Kim, S. Choi, V. S. Pham, R. Kwak, and J. Han. “Energy efficiency enhancement of electromembrane desalination systems by

local flow redistribution optimized for the asymmetry of cation/anion diffusivity". *Journal of Membrane Science* 524 (2017) 280–287. (Cit. on pp. 22, 106, 135).

[Kim2021] J. Kim, S. Kim, and R. Kwak. "Controlling ion transport with pattern structures on ion exchange membranes in electrodialysis". *Desalination* 499 (2021) 114801. DOI: 10.1016/j.desal.2020.114801 (cit. on pp. 18, 22, 75, 76, 106, 135).

[Korz2016] E. Korzhova, N. D. Pismenskaya, D. Lopatin, O. Baranov, L. Dammak, and V. Nikonenko. "Effect of surface hydrophobization on chronopotentiometric behavior of an AMX anion-exchange membrane at overlimiting currents". *Journal of Membrane Science* 500 (2016) 161–170. DOI: 10.1016/j.memsci.2015.11.018 (cit. on pp. 17, 47).

[Krol1999] J. Krol, M. Wessling, and H. Strathmann. "Chronopotentiometry and overlimiting ion transport through monopolar ion exchange membranes". *Journal of Membrane Science* 162.1-2 (1999) 155–164. DOI: 10.1016/S0376-7388(99)00134-9 (cit. on p. 36).

[Ksia2020] A. N. Ksiazkiewicz, L. Bering, F. Jung, N. A. Wolter, J. Viell, A. Mitsos, and A. Pich. "Closing the 1–5 µm size gap: Temperature-programmed, fed-batch synthesis of µm-sized microgels". *Chemical Engineering Journal* 379 (2020) 122293. DOI: 10.1016/j.cej.2019.122293 (cit. on p. 129).

[Kwak2013a] R. Kwak, G. Guan, W. K. Peng, and J. Han. “Microscale electrodialysis: Concentration profiling and vortex visualization”. *Desalination* 308 (2013) 138–146. DOI: 10.1016/j.desal.2012.07.017 (cit. on pp. 15, 20, 49, 105).

[Kwak2013b] R. Kwak, S. van Pham, K. M. Lim, and J. Han. “Shear flow of an electrically charged fluid by ion concentration polarization: scaling laws for electroconvective vortices”. *Physical review letters* 110.11 (2013) 114501. DOI: 10.1103/PhysRevLett.110.114501 (cit. on pp. 15, 20, 49, 105).

[Lavr2017] S. Lavrnić, M. Zapater-Pereyra, and M. L. Mancini. “Water Scarcity and Wastewater Reuse Standards in Southern Europe: Focus on Agriculture”. *Water, Air, & Soil Pollution* 228.7 (2017) 883. DOI: 10.1007/s11270-017-3425-2 (cit. on p. 3).

[Lee2002] H.-J. Lee, F. Sarfert, H. Strathmann, and S.-H. Moon. “Designing of an electrodialysis desalination plant”. *Desalination* 142.3 (2002) 267–286. DOI: 10.1016/S0011-9164(02)00208-4 (cit. on p. 134).

[Lee2018] C.-Y. Lee and L.-M. Fu. “Recent advances and applications of micromixers”. *Sensors and Actuators B: Chemical* 259 (2018) 677–702. DOI: 10.1016/j.snb.2017.12.034 (cit. on p. 135).

[Lee2021] D. Lee, D. Choi, H. Park, H. Lee, and S. J. Kim. “Electroconvective circulating flows by Asymmetric Coulombic force distribution in multiscale porous membrane”. *Journal of Membrane Science* 80

(2021) 119286. DOI: 10.1016/j.memsci.2021.119286 (cit. on p. 136).

[Li2019] G. Li, L. A. Archer, and D. L. Koch. “Electroconvection in a Viscoelastic Electrolyte”. *Physical review letters* 122.12 (2019) 124501. DOI: 10.1103/PhysRevLett.122.124501 (cit. on p. 17).

[Lide2003] D. R. Lide, ed. *CRC handbook of chemistry and physics, 2003-2004: A ready-reference book of chemical and physical data*. 84th ed. Boca Raton, Fla.: CRC Press, 2003 (cit. on p. 37).

[Linz2021] G. Linz, S. B. Rauer, Y. Kuhn, S. Wennemaring, L. Siedler, S. Singh, and M. Wessling. “3D–Printed Bioreactor with Integrated Impedance Spectroscopy for Cell Barrier Monitoring”. *Advanced Materials Technologies* 6.6 (2021) 2100009. DOI: 10.1002/admt.202100009 (cit. on p. 32).

[Liu2020] W. Liu, Y. Zhou, and P. Shi. “Scaling laws of electroconvective flow with finite vortex height near permselective membranes”. *Physical review. E* 102.3-1 (2020) 033102. DOI: 10.1103/PhysRevE.102.033102 (cit. on p. 136).

[Male1992] F. Maletzki, H.-W. Rösler, and E. Staude. “Ion transfer across electrodialysis membranes in the overlimiting current range: stationary voltage current characteristics and current noise power spectra under different conditions of free convection”. *Journal of Membrane Science* 71.1-2 (1992) 105–116. DOI: 10.1016/0376-7388(92)85010-G (cit. on p. 14).

[Mani2020] A. Mani and K. M. Wang. “Electroconvection Near Electrochemical Interfaces: Experiments, Modeling, and Computation”. *Annual Review of Fluid Mechanics* 52.1 (2020) 509–529. DOI: 10.1146/annurev-fluid-010719-060358 (cit. on pp. 4, 11, 14–16, 39, 46, 49, 62, 74, 75, 83, 104, 105, 129–131).

[Mani2021] A. Mani and D. Park. “Macroscopic forcing method: a tool for turbulence modeling and analysis of closures”. *Physical Review Fluids* 6.5 (2021) 5. DOI: 10.1103/PhysRevFluids.6.054607 (cit. on p. 133).

[Mare2018] S. A. Mareev, D. Butylskii, N. D. Pismenskaya, C. Larchet, L. Dammak, and V. Nikonenko. “Geometric heterogeneity of homogeneous ion-exchange Neosepta membranes”. *Journal of Membrane Science* 563 (2018) 768–776. DOI: 10.1016/j.memsci.2018.06.018 (cit. on pp. 17, 47, 75).

[Mars2020] L. T. Marston, G. Lamsal, Z. H. Ancona, P. Caldwell, B. D Richter, B. L. Ruddell, R. R. Rushforth, and K. Frankel Davis. “Reducing water scarcity by improving water productivity in the United States”. *Environmental Research Letters* 15.9 (2020) 094033. DOI: 10.1088/1748-9326/ab9d39 (cit. on p. 3).

[Meko2016] M. M. Mekonnen and A. Y. Hoekstra. “Four billion people facing severe water scarcity”. *Science advances* 2.2 (2016) e1500323. DOI: 10.1126/sciadv.1500323 (cit. on p. 2).

[Meli2007] T. Melin and R. Rautenbach. *Membranverfahren: Grundlagen der Modul- und Anlagenauslegung*. 3., aktualisierte und erweiterte Auflage. Berlin, Heidelberg: Springer-Verlag Berlin Heidelberg, 2007. DOI: 10.1007/978-3-540-34328-8 (cit. on pp. 4–6).

[Mikh2016] S. Mikhaylin, V. Nikonenko, N. D. Pismenskaya, G. Pourcelly, S. Choi, H. J. Kwon, J. Han, and L. Bazinet. “How physico-chemical and surface properties of cation-exchange membrane affect membrane scaling and electroconvective vortices: Influence on performance of electrodialysis with pulsed electric field”. *Desalination* 393 (2016) 102–114. DOI: 10.1016/j.desal.2015.09.011 (cit. on p. 17).

[Mish1998] N. A. Mishchuk. “Electro-osmosis of the second kind near the heterogeneous ion-exchange membrane”. *Colloids and Surfaces A: Physicochemical and Engineering Aspects* 140.1-3 (1998) 75–89. DOI: 10.1016/S0927-7757(98)00216-7 (cit. on pp. 17, 75).

[Nass2020] H. Nassrullah, S. F. Anis, R. Hashaikeh, and N. Hilal. “Energy for desalination: A state-of-the-art review”. *Desalination* 491.11 (2020) 114569. DOI: 10.1016/j.desal.2020.114569 (cit. on p. 3).

[Neba2017] K. A. Nebavskaya, V. V. Sarapulova, K. G. Sabbatovskiy, V. D. Sobolev, N. D. Pismenskaya, P. Sistat, M. Cretin, and V. Nikonenko. “Impact of ion exchange membrane surface charge and hydrophobicity on electroconvection at underlimiting and overlimiting

currents". *Journal of Membrane Science* 523 (2017) 36–44. DOI: 10.1016/j.memsci.2016.09.038 (cit. on pp. 18, 47, 75, 131).

[Neba2018] K. A. Nebavskaya, D. Y. Butylskii, I. A. Moroz, A. V. Nebavsky, N. D. Pismenskaya, and V. V. Nikonenko. "Enhancement of Mass Transfer Through a Homogeneous Anion-Exchange Membrane in Limiting and Overlimiting Current Regimes by Screening Part of Its Surface with Nonconductive Strips". *Petroleum Chemistry* 58.9 (2018) 780–789. DOI: 10.1134/S0965544118090086 (cit. on pp. 17, 18).

[Niko2014] V. V. Nikonenko, A. V. Kovalenko, M. K. Urtenov, N. D. Pismenskaya, J. Han, P. Sistat, and G. Pourcelly. "Desalination at overlimiting currents: State-of-the-art and perspectives". *Desalination* 342 (2014) 85–106. DOI: 10.1016/j.desal.2014.01.008 (cit. on pp. 13, 14, 46, 105, 134).

[Niko2017] V. V. Nikonenko, S. A. Mareev, N. D. Pismenskaya, A. M. Uzdenova, A. V. Kovalenko, M. K. Urtenov, and G. Pourcelly. "Effect of electroconvection and its use in intensifying the mass transfer in electrodialysis (Review)". *Russian Journal of Electrochemistry* 53.10 (2017) 1122–1144. DOI: 10.1134/S1023193517090099 (cit. on pp. 14, 105).

[Niko2019] V. Nikonenko, A. Nebavsky, S. Mareev, A. Kovalenko, M. Urtenov, and G. Pourcelly. "Modelling of Ion Transport in Electromembrane Systems: Impacts of Membrane Bulk and Surface Heterogeneity".

Applied Sciences 9.1 (2019) 25. DOI: 10.3390/app9010025 (cit. on p. 17).

[Pand2021] N. Pande, J. A. Wood, G. Mul, D. Lohse, B. T. Mei, and D. Krug. *Electroconvective instability in water electrolysis: an evaluation of electroconvective patterns and their onset features*. 2021. arXiv: 2101.08542 [physics.flu-dyn] (cit. on p. 136).

[Park2017] M. Park, J. Ryu, W. Wang, and J. Cho. "Material design and engineering of next-generation flow-battery technologies". *Nature Reviews Materials* 2.1 (2017) 11533. DOI: 10.1038/natrevmats.2016.80 (cit. on pp. 6, 46).

[Pawl2019] S. Pawlowski, J. G. Crespo, and S. Velizarov. "Profiled Ion Exchange Membranes: A Comprehensible Review". *International journal of molecular sciences* 20.1 (2019) DOI: 10.3390/ijms20010165 (cit. on p. 17).

[Perc2020] K. Percin, B. van der Zee, and M. Wessling. "On the Resistances of a Slurry Electrode Vanadium Redox Flow Battery". *ChemElectroChem* 7.9 (2020) 2165–2172. DOI: 10.1002/celc.202000242 (cit. on pp. 6, 46).

[Pete2016] L. Petersen, M. Heynen, and F. Pellicciotti. "Freshwater Resources: Past, Present, Future". 3 (2016) 1–12. DOI: 10.1002/9781118786352.wbieg0712.pub2 (cit. on p. 2).

[Pham2012] V. S. Pham, Z. Li, K. M. Lim, J. K. White, and J. Han. "Direct numerical simulation of electroconvective instability and hysteretic current-

voltage response of a permselective membrane". *Physical review. E, Statistical, nonlinear, and soft matter physics* 86.4 Pt 2 (2012) 046310. DOI: 10.1103/PhysRevE.86.046310 (cit. on pp. 17, 75).

[Pham2016] S. V. Pham, H. Kwon, B. Kim, J. K. White, G. Lim, and J. Han. "Helical vortex formation in three-dimensional electrochemical systems with ion-selective membranes". *Physical review. E* 93.3 (2016) 033114. DOI: 10.1103/PhysRevE.93.033114 (cit. on pp. 20, 46, 105).

[Pime2018] F. Pimenta and M. A. Alves. *Numerical simulation of electrically-driven flows using OpenFOAM*. 2018. arXiv: 1802.02843 [physics.flu-dyn] (cit. on p. 77).

[Pism2019] N. D. Pismenskaya, S. A. Mareev, E. V. Pokhidnya, C. Larchet, L. Dammak, and V. V. Nikonenko. "Effect of Surface Modification of Heterogeneous Anion-Exchange Membranes on the Intensity of Electroconvection at Their Surfaces". *Russian Journal of Electrochemistry* 55.12 (2019) 1203–1220. DOI: 10.1134/S1023193519120139 (cit. on pp. 18, 75).

[Pora2013] S. Porada, R. Zhao, A. van der Wal, V. Presser, and P. M. Biesheuvel. "Review on the science and technology of water desalination by capacitive deionization". *Progress in Materials Science* 58.8 (2013) 1388–1442. DOI: 10.1016/j.pmatsci.2013.03.005 (cit. on p. 5).

[Post2007] J. W. Post, J. Veerman, H. V. Hamelers, G. J. Euverink, S. J. Metz, K. Nymeijer, and C. J. Buisman. “Salinity-gradient power: Evaluation of pressure-retarded osmosis and reverse electrodialysis”. *Journal of Membrane Science* 288.1-2 (2007) 218–230. DOI: 10.1016/j.memsci.2006.11.018 (cit. on p. 6).

[Prob1994] R. F. Probstein. *Physicochemical Hydrodynamics: An introduction*. 2. ed., [Elektronische Ressource]. Hoboken, NJ, USA: John Wiley & Sons, Inc, 1994. DOI: 10.1002/0471725137 (cit. on pp. 6–10, 12, 21, 32, 36, 42).

[Qu2018] S. Qu, S. Liang, M. Konar, Z. Zhu, A. S. F. Chiu, X. Jia, and M. Xu. “Virtual Water Scarcity Risk to the Global Trade System”. *Environmental science & technology* 52.2 (2018) 673–683. DOI: 10.1021/acs.est.7b04309 (cit. on p. 2).

[Rogh2016] F. Roghmans, M. C. Martí-Calatayud, S. Abdu, R. Femmer, R. Tiwari, A. Walther, and M. Wessling. “Electrochemical impedance spectroscopy fingerprints the ion selectivity of microgel functionalized ion-exchange membranes”. *Electrochemistry Communications* 72 (2016) 113–117. DOI: 10.1016/j.elecom.2016.09.009 (cit. on p. 82).

[Rogh2019] F. Roghmans et al. “2D Patterned Ion–Exchange Membranes Induce Electroconvection”. *Advanced Materials Interfaces* 6.1 (2019) 1801309. DOI: 10.1002/admi.201801309 (cit. on pp. 18, 19, 24, 26, 37, 47, 75–78, 80, 81, 83, 96, 97, 126, 127, 131, 134).

[Rogh2020] F. Roghmans, E. Evdochenko, M. C. Martí-Calatayud, M. Garthe, R. Tiwari, A. Walther, and M. Wessling. “On the permselectivity of cation-exchange membranes bearing an ion selective coating”. *Journal of Membrane Science* 600.150 (2020) 117854. DOI: 10.1016/j.memsci.2020.117854 (cit. on pp. 17, 126).

[Romm2015] A. Rommerskirchen, Y. Gendel, and M. Wessling. “Single module flow-electrode capacitive deionization for continuous water desalination”. *Electrochemistry Communications* 60 (2015) 34–37. DOI: 10.1016/j.elecom.2015.07.018 (cit. on pp. 5, 46).

[Rubi1979] I. Rubinstein and L. Shtilman. “Voltage against current curves of cation exchange membranes”. *Journal of the Chemical Society, Faraday Transactions 2* 75 (1979) 231. DOI: 10.1039/F29797500231 (cit. on p. 15).

[Rubi1988] I. Rubinstein, E. Staude, and O. Kedem. “Role of the membrane surface in concentration polarization at ion-exchange membrane”. *Desalination* 69.2 (1988) 101–114. DOI: 10.1016/0011-9164(88)80013-4 (cit. on pp. 13, 15, 17).

[Rubi1991] I. Rubinstein and F. Maletzki. “Electroconvection at an electrically inhomogeneous permselective membrane surface”. *Journal of the Chemical Society, Faraday Transactions* 87.13 (1991) 2079. DOI: 10.1039/FT9918702079 (cit. on pp. 13, 18).

[Rubi2000] I. Rubinstein and B. Zaltzman. “Electro-osmotically induced convection at a permselective membrane”. *Physical Review E* 62.2

(2000) 2238–2251. DOI: 10.1103/PhysRevE.62.2238 (cit. on pp. 4, 13, 15, 47).

[Rubi2008] S. M. Rubinstein, G. Manukyan, A. Staicu, I. Rubinstein, B. Zaltzman, R. G. H. Lammertink, F. Mugele, and M. Wessling. “Direct observation of a nonequilibrium electro-osmotic instability”. *Physical review letters* 101.23 (2008) 236101. DOI: 10.1103/PhysRevLett.101.236101 (cit. on pp. 13, 15, 48, 49).

[Rubi2015] I. Rubinstein and B. Zaltzman. “Equilibrium electroconvective instability”. *Physical review letters* 114.11 (2015) 114502. DOI: 10.1103/PhysRevLett.114.114502 (cit. on p. 14).

[Sand1899] H. J. S. Sand. “On the Concentration at the Electrodes in a Solution, with special reference to the Liberation of Hydrogen by Electrolysis of a Mixture of Copper Sulphate and Sulphuric Acid”. *Proceedings of the Physical Society of London* 17.1 (1899) 496–534. DOI: 10.1088/1478-7814/17/1/332 (cit. on pp. 36, 37).

[Sant1998] J. G. Santiago, S. T. Wereley, C. D. Meinhart, D. J. Beebe, and R. J. Adrian. “A particle image velocimetry system for microfluidics”. *Experiments in Fluids* 25.4 (1998) 316–319. DOI: 10.1007/s003480050235 (cit. on p. 34).

[Scha2013] D. Schanz, A. Schröder, S. Gesemann, D. Michaelis, and B. Wieneke. “‘Shake The Box’: A highly efficient and accurate Tomographic Particle Tracking Velocimetry (TOMO-PTV) method using

prediction of particle positions". *PIV13; 10th International Symposium on Particle Image Velocimetry* (2013) (cit. on p. 38).

[Schn2016] J. F. G. Schneiders and F. Scarano. "Dense velocity reconstruction from tomographic PTV with material derivatives". *Experiments in Fluids* 57.9 (2016) 1. DOI: 10.1007/s00348-016-2225-6 (cit. on p. 38).

[Schr2015] A. Schröder, D. Schanz, D. Michaelis, C. Cierpka, S. Scharnowski, and C. J. Kähler. "Advances of PIV and 4D-PTV "Shake-The-Box" for Turbulent Flow Analysis –the Flow over Periodic Hills". *Flow, Turbulence and Combustion* 95.2-3 (2015) 193–209. DOI: 10.1007/s10494-015-9616-2 (cit. on p. 38).

[Sist1997] P. Sistat and G. Pourcelly. "Chronopotentiometric response of an ion-exchange membrane in the underlimiting current-range. Transport phenomena within the diffusion layers". *Journal of Membrane Science* 123.1 (1997) 121–131. DOI: 10.1016/S0376-7388(96)00210-4 (cit. on p. 37).

[Slou2014] Z. Slouka, S. Senapati, and H.-C. Chang. "Microfluidic systems with ion-selective membranes". *Annual review of analytical chemistry (Palo Alto, Calif.)* 7 (2014) 317–335. DOI: 10.1146/annurev-anchem-071213-020155 (cit. on p. 6).

[Stoc2021a] F. Stockmeier, D. Felder, S. Eser, M. Habermann, P. Peric, S. Musholt, K. Albert, J. Linkhorst, and M. Wessling. "Localized Electroconvection at Ion-Exchange Membranes with Heterogeneous

Surface Charge". *Under review in Nature Materials, Preprint available on Research Square* (2021) DOI: 10.21203/rs.3.rs-1093972/v1 (cit. on p. 26).

[Stoc2021b] F. Stockmeier, M. Schatz, M. Habermann, J. Linkhorst, A. Mani, and M. Wessling. "Direct 3D observation and unraveling of electroconvection phenomena during concentration polarization at ion-exchange membranes". *Journal of Membrane Science* 640.119846 (2021) DOI: 10.1016/j.memsci.2021.119846 (cit. on pp. 26, 58, 71, 74, 77, 87, 88).

[Stoc2022] F. Stockmeier, M. Schatz, M. Habermann, J. Linkhorst, A. Mani, and M. Wessling. "Measurement of Electrokinetically induced hydrodynamics at Ion-selective interfaces using 3D Micro particle tracking velocimetry (μPTV)". *MethodsX* 9.101814 (2022) DOI: 10.1016/j.mex.2022.101814 (cit. on p. 26).

[Stod2014] J. Stodollick, R. Femmer, M. Gloede, T. Melin, and M. Wessling. "Electrodialysis of itaconic acid: A short-cut model quantifying the electrical resistance in the overlimiting current density region". *Journal of Membrane Science* 453 (2014) 275–281. DOI: 10.1016/j.memsci.2013.11.008 (cit. on pp. 16, 49).

[Stra2010] H. Strathmann. "Electrodialysis, a mature technology with a multitude of new applications". *Desalination* 264.3 (2010) 268–288. DOI: 10.1016/j.desal.2010.04.069 (cit. on pp. 5, 46, 105).

[Szen1986] M. N. Szentirmay, L. F. Campbell, and C. R. Martin. “Silane coupling agents for attaching Nafion to glass and silica”. *Analytical Chemistry* 58.3 (1986) 661–662. DOI: 10.1021/ac00294a042 (cit. on p. 109).

[Tadi2016] J. G. D. Tadimeti, V. Kurian, A. Chandra, and S. Chattopadhyay. “Corrugated membrane surfaces for effective ion transport in electrodialysis”. *Journal of Membrane Science* 499 (2016) 418–428. DOI: 10.1016/j.memsci.2015.11.001 (cit. on pp. 22, 106).

[Tana1991] Y. Tanaka. “Concentration polarization in ion exchange membrane electrodialysis”. *Journal of Membrane Science* 57.2-3 (1991) 217–235. DOI: 10.1016/S0376-7388(00)80680-8 (cit. on pp. 20, 106).

[Tana2010] Y. Tanaka. “Water dissociation reaction generated in an ion exchange membrane”. *Journal of Membrane Science* 350.1-2 (2010) 347–360. DOI: 10.1016/j.memsci.2010.01.010 (cit. on p. 14).

[Tana2012] Y. Tanaka. “Mass transport in a boundary layer and in an ion exchange membrane: Mechanism of concentration polarization and water dissociation”. *Russian Journal of Electrochemistry* 48.7 (2012) 665–681. DOI: 10.1134/S1023193512060122 (cit. on pp. 20, 106).

[Tang2020] K. Tang and K. Zhou. “Water Desalination by Flow-Electrode Capacitive Deionization in Overlimiting Current Regimes”. *Environmental science & technology* 54.9 (2020) 5853–5863. DOI: 10.1021/acs.est.9b07591 (cit. on pp. 5, 46).

[Tsai2004] P. Tsai, Z. A. Daya, and S. W. Morris. “Aspect-ratio dependence of charge transport in turbulent electroconvection”. *Physical review letters* 92.8 (2004) 084503. DOI: 10.1103/PhysRevLett.92.084503 (cit. on p. 32).

[Tzan2020] V. A. Tzanakakis, N. V. Paranychianakis, and A. N. Angelakis. “Water Supply and Water Scarcity”. *Water* 12.9 (2020) 2347. DOI: 10.3390/w12092347 (cit. on pp. 2, 3).

[UNES2020] UNESCO and UN-Water. *Water and climate change*. Vol. 2020. Paris: Unesco, 2020 (cit. on p. 2).

[Unit2019] United Nations Children’s Fund (UNICEF) and World Health Organization. *Progress on household drinking water, sanitation and hygiene 2000-2017: Special focus on inequalities*. 2019 (cit. on p. 2).

[Urte2013] M. K. Urtenov, A. M. Uzdenova, A. V. Kovalenko, V. Nikonenko, N. D. Pismenskaya, V. I. Vasil’eva, P. Sistat, and G. Pourcelly. “Basic mathematical model of overlimiting transfer enhanced by electroconvection in flow-through electrodialysis membrane cells”. *Journal of Membrane Science* 447 (2013) 190–202. DOI: 10.1016/j.memsci.2013.07.033 (cit. on pp. 20, 106).

[Vale2015] J. C. de Valenca, R. M. Wagterveld, R. G. H. Lammertink, and P. A. Tsai. “Dynamics of microvortices induced by ion concentration polarization”. *Physical review. E, Statistical, nonlinear, and soft matter physics* 92.3 (2015) 031003. DOI: 10.1103/PhysRevE.92.031003 (cit. on pp. 16, 32, 34, 35, 46, 48, 55, 57, 80).

[Vale2017a] J. C. de Valenca. *Overlimiting current properties at ion exchange membranes*. 2017. DOI: 10.3990/1.9789036543149 (cit. on pp. 33, 37, 46, 48).

[Vale2017b] J. C. de Valença, A. Kurniawan, R. M. Wagterveld, J. A. Wood, and R. G. H. Lammertink. “Influence of Rayleigh-Bénard convection on electrokinetic instability in overlimiting current conditions”. *Physical Review Fluids* 2.3 (2017) DOI: 10.1103/PhysRevFluids.2.033701 (cit. on p. 32).

[Vale2018a] J. C. de Valenca, M. Jõgi, R. M. Wagterveld, E. Karatay, J. A. Wood, and R. G. H. Lammertink. “Confined Electroconvective Vortices at Structured Ion Exchange Membranes”. *Langmuir : the ACS journal of surfaces and colloids* 34.7 (2018) 2455–2463. DOI: 10.1021/acs.langmuir.7b04135 (cit. on pp. 18, 19, 75, 76, 90).

[Vale2018b] J. C. de Valenca, M. Jõgi, R. M. Wagterveld, E. Karatay, J. A. Wood, and R. G. H. Lammertink. “Confined Electroconvective Vortices at Structured Ion Exchange Membranes”. *Langmuir : the ACS journal of surfaces and colloids* 34.7 (2018) 2455–2463. DOI: 10.1021/acs.langmuir.7b04135 (cit. on p. 70).

[Volo2005] E. Volodina, N. D. Pismenskaya, V. Nikonenko, C. Larchet, and G. Pourcelly. “Ion transfer across ion-exchange membranes with homogeneous and heterogeneous surfaces”. *Journal of Colloid and Interface Science* 285.1 (2005) 247–258. DOI: 10.1016/j.jcis.2004.11.017 (cit. on pp. 17, 75).

[Warr2021] A. Warren, A. Sharma, D. Zhang, G. Li, and L. A. Archer. “Structure and Dynamics of Electric-Field-Driven Convective Flows at the Interface between Liquid Electrolytes and Ion-Selective Membranes”. *Langmuir* 37.19 (2021) 5895–5901. DOI: 10.1021/acs.langmuir.1c00374 (cit. on pp. 35, 46, 48).

[Went2020] I. G. Wenten, K. Khoiruddin, M. A. Alkhadra, H. Tian, and M. Z. Bazant. “Novel ionic separation mechanisms in electrically driven membrane processes”. *Advances in colloid and interface science* 284 (2020) 102269. DOI: 10.1016/j.cis.2020.102269 (cit. on p. 17).

[Werb2016] J. R. Werber, C. O. Osuji, and M. Elimelech. “Materials for next-generation desalination and water purification membranes”. *Nature Reviews Materials* 1.5 (2016) 3. DOI: 10.1038/natrevmats.2016.18 (cit. on pp. 5, 46).

[Wess2014] M. Wessling, L. G. Morcillo, and S. Abdu. “Nanometer-thick lateral polyelectrolyte micropatterns induce macrosopic electro-osmotic chaotic fluid instabilities”. *Scientific reports* 4 (2014) 4294. DOI: 10.1038/srep04294 (cit. on pp. 17, 75).

[Wess2015] M. Wessling, L. G. Morcillo, and S. Abdu. “Nanometer-thick lateral polyelectrolyte micropatterns induce macrosopic electro-osmotic chaotic fluid instabilities”. *Sci. Rep.* 4.1 (May 2015) 4294. DOI: 10.1038/srep04294 (cit. on p. 47).

[Will2010] P. Willems, N. G. Deen, A. Kemperman, R. Lammertink, M. Wessling, M. van Sint Annaland, J. Kuipers, and W. van der Meer. “Use of Particle Imaging Velocimetry to measure liquid velocity profiles in liquid and liquid/gas flows through spacer filled channels”. *Journal of Membrane Science* 362.1-2 (2010) 143–153. DOI: 10.1016/j.memsci.2010.06.029 (cit. on p. 24).

[Worl2017] World Health Organization and United Nations Children’s Fund (UNICEF). *Safely managed drinking water - thematic report on drinking water 2017*. 2017 (cit. on p. 2).

[Yari2009] E. Yariv. “Asymptotic current-voltage relations for currents exceeding the diffusion limit”. *Physical review. E, Statistical, nonlinear, and soft matter physics* 80.5 Pt 1 (2009) 051201. DOI: 10.1103/PhysRevE.80.051201 (cit. on p. 42).

[Yoss2008] G. Yossifon and H.-C. Chang. “Selection of nonequilibrium overlimiting currents: universal depletion layer formation dynamics and vortex instability”. *Physical review letters* 101.25 (2008) 254501. DOI: 10.1103/PhysRevLett.101.254501 (cit. on pp. 13, 15, 49).

[Yoss2009] G. Yossifon, P. Mushenheim, Y.-C. Chang, and H.-C. Chang. “Nonlinear current-voltage characteristics of nanochannels”. *Physical review. E, Statistical, nonlinear, and soft matter physics* 79.4 Pt 2 (2009) 046305. DOI: 10.1103/PhysRevE.79.046305 (cit. on pp. 15, 49).

[Zabo1988] V. I. Zabolotskii, N. V. Shel'deshov, and N. P. Gnusin. "Dissociation of Water Molecules in Systems with Ion-exchange Membranes". *Russian Chemical Reviews* 57.8 (1988) 801–808. DOI: 10.1070/RC1988v057n08ABEH003389 (cit. on pp. 14, 105).

[Zabo1993] V. I. Zabolotsky and V. Nikonenko. "Effect of structural membrane inhomogeneity on transport properties". *Journal of Membrane Science* 79.2-3 (1993) 181–198. DOI: 10.1016/0376-7388(93)85115-D (cit. on pp. 17, 75).

[Zabo1998] V. I. Zabolotsky, V. V. Nikonenko, N. D. Pismenskaya, E. V. Laktionov, M. Urtenov, H. Strathmann, M. Wessling, and G. H. Koops. "Coupled transport phenomena in overlimiting current electrodialysis". *Separation and Purification Technology* 14.1-3 (1998) 255–267. DOI: 10.1016/S1383-5866(98)00080-X (cit. on p. 14).

[Zabo2005] V. I. Zabolotskii, S. A. Loza, and M. V. Sharafan. "Physicochemical Properties of Profiled Heterogeneous Ion-Exchange Membranes". *Russian Journal of Electrochemistry* 41.10 (2005) 1053–1060. DOI: 10.1007/s11175-005-0180-2 (cit. on p. 17).

[Zabo2017] V. I. Zabolotsky, L. Novak, A. V. Kovalenko, V. V. Nikonenko, M. H. Urtenov, K. A. Lebedev, and A. Y. But. "Electroconvection in systems with heterogeneous ion-exchange membranes". *Petroleum Chemistry* 57.9 (2017) 779–789. DOI: 10.1134/S0965544117090109 (cit. on pp. 17, 75).

[Zalt2007] B. Zaltzman and I. Rubinstein. “Electro-osmotic slip and electroconvective instability”. *Journal of Fluid Mechanics* 579 (2007) 173. DOI: 10.1017/S0022112007004880 (cit. on pp. 14, 15).

[Zhan2018] K. Zhang, Y. Ren, L. Hou, X. Feng, X. Chen, and H. Jiang. “An efficient micromixer actuated by induced-charge electroosmosis using asymmetrical floating electrodes”. *Microfluidics and Nanofluidics* 22.11 (2018) 53. DOI: 10.1007/s10404-018-2153-2 (cit. on p. 136).

[Zour2015] Z. Zourmand, F. Faridirad, N. Kasiri, and T. Mohammadi. “Mass transfer modeling of desalination through an electrodialysis cell”. *Desalination* 359.1 (2015) 41–51. DOI: 10.1016/j.desal.2014.12.008 (cit. on p. 16).